

Fundamental Study of Bubble Coalescence in Solutions and on Surfaces

by

Bo Liu

A thesis submitted in partial fulfillment of the requirements for the degree of

Doctor of Philosophy

in

Chemical Engineering

Department of Chemical and Materials Engineering

University of Alberta

© Bo Liu, 2019

Abstract

The coalescence of air bubbles is an elementary process influencing the performance of various industrial processes such as oil extraction, water purification, and mineral flotation. The possible coalescence between two colliding bubbles is significantly influenced by the liquid drainage rate from the thin film trapped between the bubbles.

The focus of this thesis is to investigate the film dynamics between fast colliding air bubbles in aqueous solutions. A unique method is developed based on a custom-designed Dynamic Force Apparatus (DFA). Two bubbles, one generated at the orifice of a capillary tube, the other immobilized on a transparent hydrophobic glass (surface microbubble), are brought together for the collision at controlled speeds. During the bubble collision, the interaction force and the interference fringes are obtained simultaneously. Experimental parameters can be flexibly adjusted, including the surface microbubble size, solution concentration, and collision speed.

Under aged/contaminated conditions, the air-water interface is immobile. The interaction force and the initial formation of the dimple profile during the collision, agree well with the prediction from the Stokes-Reynolds-Young-Laplace model with the tangentially immobile boundary condition at the air-liquid interface. However, an ‘express exit’ was observed during bubble collision, leading to the unexpected rapid drainage of the trapped liquid. This phenomenon partially explains the shorter coalescence times from experiments as compared with model predictions. The film rupture thickness was consis-

tently observed at 25 ± 15 nm.

In contrast, when clean water was used, the film thinning rate was almost equal to the collision speed, resulting in bubble coalescence within milliseconds. The experimental data are explained by a theoretical model assuming mobile boundary condition at the air-water interface. Changing the interfacial tension by 10^{-4} N/m, by adding a small amount of surfactant, would be sufficient to immobilize the air-water interface. The surface mobility is determined by the competition of fluid shear stress on the film surface and the Marangoni stress that arises from the uneven distribution of surface active components at the air-water interface. The above finding proved the existence of fully mobile air-water interfaces in bubble coalescence, and also explained why this boundary condition is difficult to be achieved experimentally in previous research.

The following exploration was conducted in surfactant solutions at the concentration of up to 2 mM. A simple experimental technique was developed, in which the freshly generated bubbles can collide after staying in bulk for a very short period (~ 10 ms or ~ 50 ms). From the bounce or coalescence results, we found that the mobile air-water interface is achievable even in surfactant solutions similar to those used in industrial processes. The freshly generated bubbles can be mobile and may switch to immobile after staying in bulk for tens of milliseconds. The surface mobility is jointly determined by the aging time and bulk surfactant concentration, corresponding to the dynamic adsorption of the surfactant onto the air-water interface. This work bridges the fundamental understanding of surface mobility to real applications.

Preface

This thesis is composed of several papers that have been either published or submitted. Below is the statement of contributions to these co-authored papers that are presented in Chapters 3, 4 and 5.

1. Bo Liu, Rogerio Manica, Xurui Zhang, Adrien Bussonnière, Zhenghe Xu, Guangyuan Xie, Qingxia Liu. Dynamic Interaction between a Millimeter-Sized Bubble and Surface Microbubbles in Water, *Langmuir*, 2018, 34(39): 11667-11675. Bo Liu performed all the experiments and data analysis, and wrote the entire paper. Rogerio Manica helped with the modeling section. Qingxia Liu supervised the work. Xurui Zhang and Adrien Bussonnière were involved in the experimental design. All the authors contributed to the discussion and commented on the manuscript.

2. Bo Liu, Rogerio Manica, Qingxia Liu, Evert Klaseboer, Zhenghe Xu, Guangyuan Xie. Coalescence of Bubbles with Mobile Interfaces in Water. *Physical Review Letters*, 2019, 122(19): 194501. Bo Liu performed all the experiments and data analysis, and wrote the entire paper. Rogerio Manica helped with the modeling section. Evert Klaseboer provided valuable suggestions and helped with the manuscript proofreading. Qingxia Liu supervised the work. All the authors contributed to the discussion and commented on the manuscript.

3. Bo Liu, Rogerio Manica, Qingxia Liu, Evert Klaseboer, Zhenghe Xu. Coalescence or Bounce? How Surfactant Adsorption in Milliseconds Affects Bubble Collision. Submitted to *The Journal of Physical Chemistry Letters*. Bo Liu performed all the experiments and data analysis, and wrote the paper. Rogerio Manica helped with the theory. Evert Klaseboer helped with the manuscript proofreading. Qingxia Liu supervised the work. All the authors

contributed to the discussion and commented on the manuscript.

To my wife
I am so blessed to have you in my life.

Acknowledgements

First and foremost, I would like to thank my supervisor, Professor Qingxia Liu, for his instruction, support, and motivation throughout each stage of my graduate study.

I would like to express my sincere appreciation to my mentor and coffee partner, Dr Rogerio Manica, for all the coffee break discussions on science and life. I am also in debt to him for the guidance, encouragement and patience.

I thank Professor Zhenghe Xu for generously allowing me to use all the instruments in his lab.

I also express my thanks to Dr Adrien Bussonnière and Professor Amy Tsai for their instructions and help.

The comments and discussions from Dr Evert Klaseboer are greatly appreciated.

I thank Dr Zhenzhen Lu and Dr Xurui Zhang for their training and discussions.

I acknowledge Mr Carl Carbett, Ms Laurie Kachmaryk, Mr James Skwarok, Ms Patricia Siferd, Ms Jie Ru, Mr Les Dean, Mr Robert Smith for their administrative and technical assistance.

I am really happy to meet all the colleagues and friends in our research group. Their company in the past years becomes an important section of my life.

My deepest gratitude goes to my parents, my sister Xiaoya, and my wife Yadi for all the love and support.

Contents

1	Introduction	1
1.1	Background and motivations	1
1.2	Objectives and scope of the thesis	2
1.3	Structure of the thesis	3
2	Literature Review	5
2.1	Introduction	5
2.2	Theoretical models	6
2.2.1	Young-Laplace equation	7
2.2.2	Disjoining pressure	8
2.2.3	Lubrication approximation for thin film drainage	9
2.2.4	Initial condition and boundary conditions	13
2.3	Experimental methods	14
2.3.1	Bubble swarm method	14
2.3.2	Thin film interferometry method	15
2.3.3	Bubble pair method	17
2.4	Controversies	21
2.4.1	Air-water surface charge and colloidal stability	22
2.4.2	Variation of coalescence time at similar experimental conditions	23
2.4.3	Rapid bubble coalescence within milliseconds	23
3	Dynamic Interaction Between a Millimeter Sized Bubble and Surface Microbubbles in Water	25
3.1	Introduction	28
3.2	Experimental section	30
3.2.1	Materials and methods	30
3.2.2	Experimental system	31
3.3	Description of the theoretical model	33
3.4	Results and discussions	35
3.5	Summary	44
4	Coalescence of Bubbles with Mobile Interfaces in Water	46
4.1	Introduction	48
4.2	Experimental system	49
4.3	Results and discussions	51
4.4	Conclusion	58
5	Coalescence or Bounce? How Surfactant Adsorption in Milliseconds Affects Bubble Collision	59
5.1	Introduction	61
5.2	Experimental method	62
5.3	Results and discussions	64

5.4	Conclusion	70
6	Conclusions and Future work	71
6.1	Conclusions	71
6.2	Future Research	73
	References	74
	Appendix A Experimental and data analysis	84
A.1	Bottom bubble generation	84
A.2	Alignment of the bubbles in water	84
A.3	Film thickness determination	85
A.4	Reconstruction of the thin film profile (symmetric and asymmetric)	86
A.5	Estimation of the uncertainty in the critical rupture thickness	86
A.6	Matlab code for film center thickness	88
A.6.1	Read the video	88
A.6.2	Extract light intensity	88
A.6.3	Film thickness extraction	89
	Appendix B Supporting information for chapter 3	95
B.1	Unusual force curves	95
B.2	The role of EDL interaction	96
	Appendix C Supporting information for chapter 4	99
C.1	Model description	99
C.2	Definition of time ($t=0$) and theoretical results	103
	Appendix D Supporting information for chapter 5	107
D.1	Bubble aging time	107
D.2	Pinch-off collision: bubble bounce and coalescence	108
D.3	Force balance	109
D.3.1	Initial condition	110
D.3.2	Boundary conditions	110
	Appendix E Lubrication equations	113

List of Figures

2.1	Schematics for thin film drainage and rupture during the bubble collision	6
2.2	(a) Schematic illustration for bubble collision, and the definition of coordinate; and schematic illustrations for three boundary conditions: (b) Immobile-immobile; (c) Immobile-mobile; (c) Mobile-mobile.	10
2.3	(a) Schematic for the McGill bubble viewer(adapted from Girgin et al.(2006),with permission. Elsevier); [50] (b) Schematic for the laser scattering method [51](adapted from Craig et al.(1993), with permission. American Chemical Society).	15
2.4	(a) Schematic for the ‘Scheludko’ cell [21](adapted from Karakashev et al.(2015), with permission. Elsevier); (b) A snapshot for the observed fringes. [60](adapted from Karakashev et al.(2010), with permission. Elsevier).	16
2.5	(a) Schematic illustration of the bubble pairs generated by adjunct capillaries(adapted from Oolman and Blanch(1986), with permission. Taylor&Francis); [64] (b) Schematic illustration for the rising bubble colliding with the fluid interface(adapted from Castillo et al.(2011), with permission. Elsevier). [18]	17
2.6	(a) Schematic illustration of the integrated thin film drainage apparatus(adapted from Wang et al.(2013), with permission. American Chemical Society); [72] (b) Schematic illustration of the AFM bubble collision technique(adapted from Browne et al.(2011), with permission. American Chemical Society). [73]	18
2.7	(a) Schematic illustration for the rising bubble experimental system by Doubliez(adapted from Doubliez (1991), with permission. Elsevier); [74] (b) Snapshots of the colliding bubbles and the interference fringes(adapted from Morokuma (2018), with permission. Elsevier). [75]	19
2.8	(a) Bubble pair interferometry method based on the dynamic force apparatus [79], the insets show the interaction force and the interference fringes(adapted from Liu et al, (2018), with permission. America Chemistry Society); (b) The interferometry method to investigate bubble-bubble collision reported by Gao and Pan (adapted from Gao & Pan(2018), with permission. American Chemical Society). [80]	20

2.9	(a) The coalescence map by Horn et al (adapted from Horn et al.(2011), with permission. Elsevier). [6] (b) The experimental data shows the variation of coalescence times with collision speeds (adapted from Castillo et al.(2011), with permission. Elsevier). [18]	22
3.1	Schematic illustration of the experimental system, a millimeter bubble is generated at the end of a glass capillary. The capillary is moved downward towards a surface microbubble immobilized on a transparent hydrophobic surface. The interaction force is monitored by a bimorph cantilever during the bubble collision. The thin liquid film entrapped between the two bubbles is monitored by interference fringes through an inverted microscope connected to a high speed camera. The inset illustrates the surface deformation; the coordinate system and the film thickness $h(r, t)$ are defined.	32
3.2	Typical (A) displacement curve and (B) force profile during a measurement run between a millimeter bubble ($R_B = 1.2$ mm) and a micrometer bubble ($R = 550$ μ m) immobilized on the surface of hydrophobic silica at the approach velocity of 1 mm/s. The raw data are smoothed using a Matlab function. The interaction force is divided into four stages as time progresses, with a repulsive force before coalescence followed by an attractive capillary force after the rupture of the thin liquid film. The dash lines refer to the initial collision point.	36
3.3	Snapshots of the interference fringes between a top bubble ($r = 1.2$ mm) and the surface microbubble ($r = 550$ μ m) recorded at 3000 frames per second. Detailed information about the gradual expansion of the symmetric film, the unexpected lose of symmetry, and the black film before rupture are shown in sequence. The times for the snapshots here correspond to the same times in Figure 3.2B.	37
3.4	Experimental measured force (circles) vs SRYL prediction (solid lines) for two different bubble sizes. The force rises quickly during the approaching stage and remains constant during the holding stage until coalescence happens. In this plot, the theoretical curve was computed using the experimental time and stopped when the bubbles coalesced in the experiment.	39
3.5	Coalescence time vs surface bubble radius in various aqueous salt solutions. The solid line is the theoretical prediction using SRYL model. The approach velocity is 1 mm/s, the radius of the top bubble is 1.2 mm.	40
3.6	Critical rupture thickness vs bubble size in various aqueous salt solutions. The inset A shows the pixel points taken from the critical rupture. The average of 9 pixels(6×6 μ m ²) are plotted to show the evolution of light intensity over time in inset B. The blue circles are the critical rupture thickness calculated based on the light intensity. Two data points from the surface bubbles around 1 mm in radii are also included. A method for the estimation of the upper and lower bounds for the critical rupture thickness is described in the Apendix A. The red dashed line is the dividing line where the disjoining pressure (VDW interaction) equals the Laplace pressure.	42

3.7	Rim thickness vs time according to the SRYL model prediction. Square dots indicate the experimental coalescence times for these cases. The inset shows comparison between theory (solid lines) and experiment (symbols) for the thickest and thinnest parts of the film. The dash line is a guide for the eye.	43
3.8	The shape of small and large bubbles predicted from the model just before coalescence.	44
4.1	(a) Schematic of the experimental setup. A bubble of radius $R_b=1.2$ mm was held at the glass capillary orifice, whereas another bubble of radius R_s was immobilized on a hydrophobic silica surface. The capillary was driven downward by a speaker diaphragm at the velocity V to achieve collision between the bubbles. A high-speed camera connected to an inverted microscope was used to record the interference fringes. (b) Side view illustration of the bubbles, where lines are used to monitor top bubble size and position. (c) A snapshot of the interference fringes obtained between two colliding bubbles ($R_s=0.79$ mm, $V=28$ mm/s, $5 \mu\text{M}$ SDS).	50
4.2	(a) Snapshots of the interference fringes in a time sequence obtained between two colliding bubbles ($R_s=0.73$ mm, $V=1$ mm/s). (b) Evolution of the light intensity at the film center marked by the red square (2×2 pixels, $\sim 4\times 4 \mu\text{m}^2$), from which we obtained (c) time evolution of the film thickness (circles) compared with approaching undeformed bubbles (straight line). (d) Thin film drainage with immobile air water interfaces ($R_s=0.55$ mm, $V=1$ mm/s). Before collision, the bubbles were left in bulk for over 60 minutes so that the interfaces were contaminated and immobilized.	52
4.3	(a) Experimental film drainage at different approach velocities in the range 0.5 to 2.8 mm/s. The slope of thickness-time evolution indicates the film thinning velocity. (b) Comparison between experiments and theory [44, 45] that assumes lubrication and fully mobile boundary condition. In (a) and (b) each curve 'i' has been shifted by a time t_i for clarity. (c) In the theoretical prediction, the maximum shear stress along the interfaces evolves with center film thickness ($R_s=0.65$ mm, $V=10$ mm/s).	53
4.4	(a) Fringes showing dimple formation in $7.5 \mu\text{M}$ SDS solution, $R_s=0.83$ mm, $V=2.8$ mm/s ($\tau_{fmax} \approx 3.2$ Pa). (b) Small film width in pure water, $R_s=0.85$ mm, $V=2.8$ mm/s. (c) Rapid evolution of interference fringes in $10 \mu\text{M}$ SDS, $R_s=0.79$ mm, $V=50$ mm/s ($\tau_{fmax} \approx 6.6$ Pa), resulting in (d) film profiles for times from top to bottom: 0.175, 0.250, 0.300, 0.350, 0.500 and 1.325 ms. (e) The probability of rapid coalescence (<5 ms) as a function of maximum shear stress ($\tau_{fmax} \sim V^{0.25}$, symbols), where '0' represent no coalescence and '1' represents rapid coalescence. Lines correspond to a cumulative Gaussian distribution fit.	56

5.1	(a) Schematic of the rising bubble experimental setup. (b) Snapshots of a rising bubble and its collision with the flat air-water interface in a 0.03 mM SDS solution. Images were pre-treated by ImageJ. (c) The extracted bubble trajectory, from which the rise collision and pinch-off collision were designed (see insets) with different aging time (~ 50 ms and ~ 10 ms, respectively). Time $t=0$ is defined as the time the bubble would have ‘touched’ the flat interface if there was no deformation; the flat surface is defined as the position $z=0$. The position of the bubble was extracted from the images by Matlab.	63
5.2	(a) Snapshots of the bubble bounce in the 0.05 mM SDS solution; bubble radii are ~ 0.52 mm, collision velocity is 18.3 cm/s. (b) Snapshots for bubble coalescence in milli-Q water; bubble radii are ~ 0.40 mm, collision velocity is 19.2 cm/s. The time $t=0$ is defined as the first image that the two bubbles ‘touched’ from side view observation, which means that the actual distance is below $15 \mu\text{m}$ (1 pixel).	65
5.3	Probability of coalescence as a function of surfactant concentration for pinch-off and rise collisions.	67
5.4	Comparison between theory and experiment for the bubble position under different conditions. The insets show the coordinate definitions and the schematic representations of the boundary conditions. (a) Two bubbles coalescence with mobile surfaces in Milli-Q water ($R_1=R_2=0.38$ mm, collision velocity is 17.8 cm/s). (b) Bubble-flat surface collision in 0.03 mM SDS solution ($R=0.48$ mm, collision velocity is 21.2 cm/s, immobile-mobile boundary condition). (c) Bubble-flat surface collision in 1 mM SDS solution ($R=0.45$ mm, collision velocity is 11.4 cm/s, immobile-immobile boundary condition). (d) Comparison of film forces for the cases a, b and c.	68
A.1	(a) A bubble was generated from the capillary tube. (b) The bubble was driven to the surface to form a capillary bridge (c) Air was sucked out using the syringe. (d) After the air bridge broke, a bubble remained at the solid surface.	92
A.2	Alignment of the bubbles assisted by the inverted microscope (A) Focus at the quartz glass top surface, the surface bubble is observed; (B) Focus at the bottom of the top bubble, the center area is marked using the red box; (C) Focus at the top of the surface microbubble, the center area is marked using a grey box. The overlap of the red and the grey boxes indicate a proper alignment of two bubbles; (D) The focus is moved upward a little for interference fringe observation.	93
A.3	(a) The film thickness reconstructed from the light intensity obtained in different channels and the fitting by a 4th order polynomial. (b) The deviations of the experimental data from the fit.	94
A.4	Thin film profile between a top bubble ($R=1.2$ mm) and a surface bubble ($R=550 \mu\text{m}$) in water (A) Comparison between theoretical predictions and experimental film profiles before the loss of symmetry; (B) 3D thin film profile reconstructed from the last snapshot of Figure 3.3.	94

B.1	(A) The interaction force between a top millimeter bubble and surface microbubbles with the radius of $68 \mu\text{m}$ (early coalesce) and $330 \mu\text{m}$ (late coalesce); (B) The predicted film thickness at the rim between the top bubble and the surface microbubble ($R= 68 \mu\text{m}$), the model prediction stops at the rupture time obtained from the experiment. The inset shows the size dependence trend of the interaction force and coalescence time.	96
B.2	Pressure profile between two identical air-water interfaces (A) surface potential is -20 mV ; (B) surface potential is -40 mV . The disjoining pressure was calculated based on the DLVO theory under constant surface charge (CC, top line) and constant surface potential (CP, bottom line) boundary conditions. The Laplace pressure (straight line) is calculated with the radius of $500 \mu\text{m}$. The solution is assumed to be 1:1 monovalent salt at the concentration of 1 mM/L .	97
C.1	Schematic illustration for the film flow with immobile and mobile boundary conditions: (a) The interfaces are assumed to be clean so that the Marangoni stress is not considered. The interfacial velocity U is determined by the continuity of tangential shear stress across the interface. For this system the first term on the right hand side of equation C.1 dominates. (b) The tangential shear stress on the interface due to film flow is balanced by the Marangoni stress at the interface ($\partial\sigma/\partial r$) due to the uneven distribution of surface active materials at the interfaces, rendered the surface immobile ($U = 0$). In this case the first term on the right hand side of equation C.1 drops out. Theoretically, these two boundary conditions give rise to drainage rates that are different by orders of magnitude.	101
C.2	Comparison between model prediction (lines) and experimental results (blue circles). The definition of time $t = 0$ as the moment that the two undeformed bubbles would have touched each other is represented by the red solid line at constant approach velocity ($V = -dh/dt$). (a) Under the influence of attractive Van der Waals, the theoretical result (green dashed line) predicts film rupture without the formation of a dimple at a time slightly shorter than the experimental film rupture. Inset shows schematic representing the definition of $t = 0$. (b) The effect of bubble size was considered theoretically by performing calculations at the lower end ($R_s = 0.4 \text{ mm}$, solid cyan line) and higher end ($R_s = 0.85 \text{ mm}$, dashed green line) of our experimental bubble sizes. In this plot, the influence of Van der Waals was omitted. The formation of a dimple was only predicted at very small thicknesses, after the experimental film rupture had occurred.	104

C.3	(a) Experimental data from Figure 4.3a are plotted together following the definition of time $t=0$. (b) Time and thickness are scaled using theoretical time and length scales typical of this system. The red straight line corresponds to the film thinning at the applied speeds. As expected, the data curves overlap, indicating that this model is appropriate for our system. Inset shows the same plot using log scale, where it becomes evident that the rupture thickness and rupture time are similar for all cases. The theoretical prediction shows slightly shorter coalescence time. In this plot we took $R_s = 0.65$ mm, which is a typical value of our experimental data.	106
D.1	(a) Snapshots for bubble bounce where a slowly rising bubble was pushed aside by a rapid growing one; (b) Snapshots for the bubble coalescence process. The growing bubble merge into the rising one within 0.4 ms.	108
D.2	(a) Schematic of the rising bubble hitting another bubble resting on the flat surface, with the symbols defined; (b) Schematic of the rising bubble hitting the flat surface, with the symbols defined. The other three schematics describe the boundary conditions at the air-water interface: (c) Immobile-immobile; (d) Immobile-mobile; (e) Mobile-mobile.	111
E.1	(a) Schematic illustration for bubble collision; (b) the definition of the coordinate system; (c) schematic illustration of the radial velocity U_r	114

Chapter 1

Introduction

1.1 Background and motivations

The coalescence of air bubbles in aqueous solutions is an elemental process in various industrial and environmental applications, such as mineral flotation, oil extraction, and water purification. Bubble coalescence should be avoided or enhanced based on the process requirement. Examples can be found with mineral flotation, where the attachment between air bubbles and hydrophobic particles is required. According to previous studies, the bubble-particle attachment is enhanced with the reduced bubble size, i.e., less bubble coalescence. However, the microbubble alone cannot efficiently lift the particles up to be recovered. Recently, a dual bubble flotation technology was developed in our research group, in which the bubble-particle attachment is expected to include two stages. In the first stage, microbubbles are generated on the surface of the mineral particle through hydrodynamic or acoustic cavitation. In the second stage, large bubbles are introduced into the flotation system to attach onto the micro-bubble frosted particles. With the microbubbles frosted at the surface, the large bubble-particle attachment should be accelerated because of the coalescence between the large bubble and the surface microbubble. Therefore, the fundamental knowledge on bubble coalescence is essential for further technology improvement.

The colliding bubbles trap a thin liquid film in between. The coalescence dynamic involves the thinning and rupturing of the thin film, which is a complex interplay of hydrodynamic drainage, surface deformation, and surface

forces. There are numerous techniques developed to investigate the bubble coalescence process. However, the direct observation on the film drainage is mostly conducted with slow speed collisions. For fast colliding bubbles, the film dynamic is obtained from indirect experimental results such as the coalescence time. Because of the lack of direct film information, there are many questions that remain unanswered.

1.2 Objectives and scope of the thesis

The main objective of this work is to investigate the coalescence of fast colliding bubbles by direct film observation and theoretical modeling. A new experimental method was developed based on a homemade Dynamic Force Apparatus, in which the interaction force and the thin film drainage can be simultaneously measured during bubble collision.

In the first part, the interaction between a large bubble and surface micro-bubbles was investigated. The interaction force agrees very well with the prediction of the Stokes-Reynolds-Young-Laplace model assuming immobile boundary condition at the air-water interface. However, the asymmetric film drainage was observed to accelerate the liquid flow through an ‘express exit’.

In the second part with pure water and fast colliding speed, bubble coalescence in sub-milliseconds was observed, during which the film thinning rates were roughly equal to the applied collision speeds. The result agrees with the model prediction using the fully mobile boundary condition at the air-water interface. The addition of surfactant that changed the interfacial tension by 10^{-4} N/m is sufficient to immobilize the air-water interface.

In the last part of the thesis, the impact of surfactant adsorption in milliseconds on bubble coalescence was investigated using a simple bubble rising technique. The freshly generated air bubbles are allowed to collide after staying in bulk for a very short time (~ 10 ms and ~ 50 ms). Surfactant adsorption within this time scale is sufficient to change the air-water surface mobility, and determines whether two colliding bubbles should coalesce or bounce.

1.3 Structure of the thesis

This thesis includes 6 Chapters; chapters 3-5 contain the papers that have been either published or submitted. The detailed content in each chapter is introduced below:

Chapter 1 provides a brief introduction about the background and motivations, the objectives and scope, and the structure of the thesis.

Chapter 2 is a literature review of the theoretical models, the available experimental methods about bubble coalescence, and several questions remaining unexplained.

Chapter 3 presents the study of the interaction between a millimeter-sized bubble and surface microbubbles in water. The direct film drainage observation reveals the non-symmetric drainage behavior which cannot be deduced from force measurements or side view observations. This chapter has been published:

Bo Liu, Rogerio Manica, Xurui Zhang, Adrien Bussonnière, Zhenghe Xu, Guangyuan Xie, Qingxia Liu. Dynamic Interaction between a Millimeter-Sized Bubble and Surface Microbubbles in Water, *Langmuir*, 2018, 34(39): 11667-11675.

Chapter 4 describes the coalescence of air bubbles with mobile air-water interfaces. Rapid film evolution within milliseconds was clearly captured. The effect of mobile air-water interface on bubble coalescence is clearly illustrated and the interfacial mobility transition from mobile to immobile was discussed. This chapter has been published:

Bo Liu, Rogerio Manica, Qingxia Liu, Evert Klaseboer, Zhenghe Xu, Guangyuan Xie. Coalescence of Bubbles with Mobile Interfaces in Water. *Physical Review Letters*, 2019, 122(19): 194501.

Chapter 5 illustrates the impact of surfactant dynamic adsorption on bubble coalescence. The bubble collision outcome depends on the bulk surfactant concentration and the bubble residence time in bulk. This chapter has been submitted:

Bo Liu, Rogerio Manica, Qingxia Liu, Evert Klaseboer, Zhenghe Xu. Coa-

lescence or Bounce? How Surfactant Adsorption in Milliseconds Affects Bubble Collision. Submitted to *The Journal of Physical Chemistry Letters*.

Chapter 6 contains the conclusions of this research and plans for future research. The appendix contains the supporting files for chapters 3-5.

Chapter 2

Literature Review

2.1 Introduction

Air bubbles are used in various industries as selective carriers for target minerals [1, 2], oil drops [3], or surface active chemicals [4]. The collision between air bubbles is a fundamental process that significantly impacts industrial performance. Therefore, bubble dynamics have been extensively investigated for decades. It was shown that colliding bubbles could bounce or merge into a bigger bubble [5, 6]. The collision outcome is influenced by various factors such as bubble size [7, 8], velocity [6, 9], salts [6, 10–13], and surfactants [8, 14]. All those factors impact the thinning and rupturing of the thin liquid film trapped between the bubbles [6–8, 12, 15].

The bubble coalescence is inhibited by the formation of a thin liquid film in between [6, 7]. The schematic illustrations in Figure 2.1 describe the film thinning and rupturing processes. The interaction between two bubbles is negligible when they are far apart. As the bubbles get closer (separation $\sim 10\ \mu\text{m}$ and smaller [7, 15]), the liquid flow between the bubbles exerts a repulsive hydrodynamic pressure on both surfaces that deform the air-water interfaces to form the thin liquid film. The coalescence of the bubbles is hindered until the film thickness reaches $\sim 50\ \text{nm}$ [8]. This simple film thinning process involves the complex interplay of hydrodynamic drainage, surface deformation and surface forces [7, 15, 16]. Some information on the film level is still lacking, which leaves several puzzles to be resolved, including the wide variation of coalescence times under the same experimental conditions [17, 18], the exis-

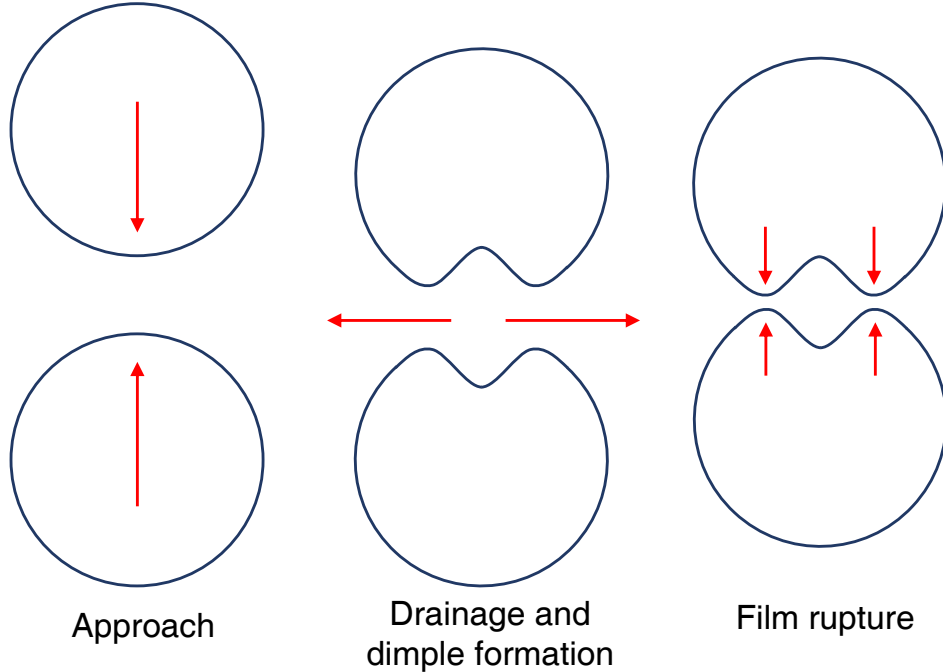


Figure 2.1: Schematics for thin film drainage and rupture during the bubble collision

tence of mobile air-water interface [6, 12, 17, 18], and the absence of colloidal stability during bubble collision at fast approaching velocity [6, 19].

After intensive research for decades, liquid drainage from the foam film or slow speed colliding bubbles (<0.2 mm/s) has been well explained, and detailed information is referred to several recent reviews [6, 19–22]. Here, we will focus on the understanding of the fast colliding bubbles. The theoretical models describing the film drainage, the experimental methods investigating the bubble collision, and several unsolved questions will be discussed.

2.2 Theoretical models

A theoretical model is required to describe the film flow between the two colliding bubbles. An early theoretical model was developed by Stefan [23], in which the film is assumed to be flat. The film drainage is driven by the pressure difference between the film region and the bulk. This model was applied for several foam film experiments with low drainage speeds. In those scenarios, the hydrodynamic pressure and/or the disjoining pressure counterbalance

the Laplace pressure to flatten the liquid film. With fast speed collisions, the hydrodynamic pressure can be higher than the Laplace pressure and may reverse the surface curvature to form a dimpled film [24], leaving a discrepancy between the theoretical assumption and experimental observation [25–27]. In subsequent work, a lubrication model that considers the local pressure distribution and surface deformation was introduced to capture the film dynamic with nanometer resolution [7, 28]. In the following section, the lubrication models using different boundary conditions at the air-water interface, the Young-Laplace equation describing the surface deformation, the initial condition, and the boundary conditions will be introduced. For simplification, axisymmetric film drainage is assumed in the following discussion. Figure 2.2a shows a schematic illustration of the colliding bubbles and the cylindrical coordinate system.

2.2.1 Young-Laplace equation

The deformation of the air-water interfaces is described by the augmented Young-Laplace equation, which assumes an equilibrium surface profile in response to the pressure [24]. Despite the rapid thinning and deformation in milliseconds, this assumption is still satisfied because the capillary wave velocity is in the order of 1 m/s [24], much faster than the characteristic collision velocities of the bubbles (0.1 m/s). For two colliding bubbles with radii R_1 and R_2 respectively, the augmented Young-Laplace equation is written as

$$\frac{\sigma}{2r} \frac{\partial}{\partial r} \left(r \frac{\partial h}{\partial r} \right) = \frac{2\sigma}{R} - p - \Pi \quad (2.1)$$

In this equation, the left-hand side term describes the change of curvature of the air-water interface, with σ as the water surface tension. On the right-hand side, the first term describes the Laplace pressure, where $R = R_1 R_2 / (R_1 + R_2)$ is the harmonic mean radius of the bubbles. The second term p is the hydrodynamic pressure due to the film flow. The third term Π is the disjoining pressure that arises from surface forces and mostly includes the van der Waals interaction and the electrical double layer interaction (also known as “DLVO theory”). Three terms on the right-hand side contribute to the local profile

in a competing manner. The spherical shape of the air bubble is a result of the Laplace pressure. Upon collision, the hydrodynamic pressure begins to grow and flatten the air-water interface; the dimple can be formed if the hydrodynamic pressure is larger than the Laplace pressure. The disjoining pressure can either flatten the film or rupture it, depending on the direction of the dominating surface force, which can be repulsive or attractive. Therefore, the surface deformation is coupled with the liquid drainage from the thin film.

2.2.2 Disjoining pressure

In the Young-Laplace equation, the disjoining pressure (Π) plays an important role on liquid drainage and surface deformation, as proved by several experimental studies [16, 29, 30]. The disjoining pressure arises from the surface forces between two air-water interfaces. According to the classical Derjaguin-Landau-Verwey-Overbeek (DLVO) theory[31], there are two surface force components contributing to the disjoining pressure (see eqn.2.2): the electrical double layer (EDL, Π_{EDL}) interaction and the van der Waals (VDW, Π_{vdw}) interaction.

$$\Pi = \Pi_{vdw} + \Pi_{EDL} \quad (2.2)$$

The electrical double layer interaction between two air bubbles should be repulsive, because the air-water interfaces are negatively charged [32]. In contrast, the VDW interaction ($\Pi_{vdw} = -A/6\pi h^3$) between two bubbles is attractive, with the Hamaker constant $A \sim 3 \times 10^{-20} J$. Furthermore, there are also discussions about the hydrophobic interaction between two air bubbles, which are reasonable because air is 'hydrophobic' [33, 34]. By including the hydrophobic interaction (Π_H), the DLVO theory is changed to the extended-DLVO theory (eqn.2.3).

$$\Pi = \Pi_{vdw} + \Pi_{EDL} + \Pi_H \quad (2.3)$$

In clean water or diluted salt solutions, the repulsive EDL interaction works at a distance below ~ 200 nm, much longer than the VDW interaction. According

to the prediction of the DLVO theory, the repulsive EDL interaction should be able to stabilize the thin liquid film, as observed between an air bubble/oil drop and negatively charged solid substrates[35, 36]. For the bubble-bubble interaction, however, this colloidal stability was rarely reported, leaving a discrepancy between the theory and the experimental observation. Detailed discussion about the discrepancy will be provided in the next section. The VDW interaction becomes important at the film thickness below ~ 50 nm, and it is suggested to be the driving force for thin film rupture[16]. The hydrophobic interaction was reported to work at a similar distance with the VDW interaction, and may also possibly account for the rupture of thin liquid film [33, 34]. However, the impact of VDW interaction and hydrophobic interaction on thin liquid film drainage, and particularly on thin film rupture, is still unclear, providing opportunities for further investigations.

2.2.3 Lubrication approximation for thin film drainage

To describe the liquid drainage from the thin liquid film, the lubrication approximation is used to simplify the full Navier-Stokes equation. Validation of the lubrication approximation can be easily justified from the Reynolds number of the film flow [37, 38]: $Re_f = \rho h_F V_F / \mu$, where $\rho \sim 10^3$ kg/m³ is the water density, $h_F \sim 1$ μ m is the film thickness, $V_F \sim 0.1$ m/s is the characteristic velocity of the air-water interface, $\mu \sim 10^{-3}$ Pa.s is the water viscosity. Despite the fact that the global Reynolds number for the air bubble can easily exceed 100 [37], the local film Reynolds number remains low ($Re_f \leq 1$). With the lubrication approximation, the momentum equation is given in equation 2.4, where $u(r, z, t)$ is the velocity component in the radial direction, p is the pressure that varies in the r -direction.

$$\frac{\partial p}{\partial r} = \mu \frac{\partial^2 u}{\partial z^2} \quad (2.4)$$

In this scenario, the continuity equation is given as:

$$\frac{1}{r} \frac{\partial (ru)}{\partial r} + \frac{\partial u_z}{\partial z} = 0 \quad (2.5)$$

where u_z is the vertical component of the liquid velocity. By integrating the continuity equation from the bottom surface ($z=0$) to the top surface

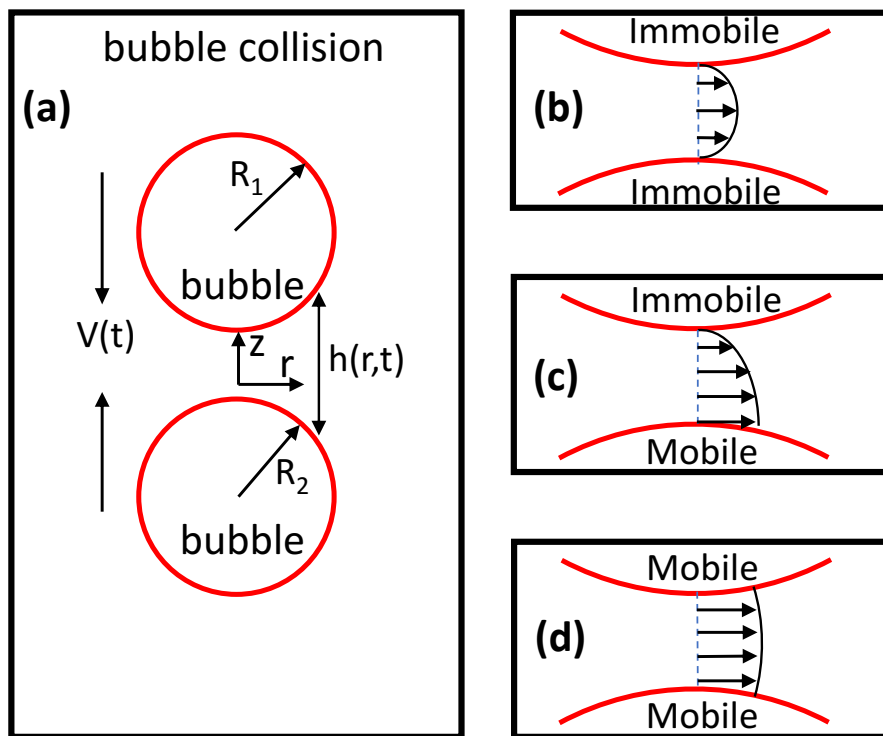


Figure 2.2: (a) Schematic illustration for bubble collision, and the definition of coordinate; and schematic illustrations for three boundary conditions: (b) Immobile-immobile; (c) Immobile-mobile; (d) Mobile-mobile.

($z = h(r, t)$) together with boundary conditions at the air-water interface, the equation can be solved to provide the film thinning rate in response to the pressure. Therefore, the boundary condition at the air-water interface is essential to get the lubrication equation.

Intrinsically, the air-water interface should be fully mobile in response to the fluid shear. However, the surface mobility is significantly influenced by the surfactants or contaminations in the bulk and on the surface [39]. The surfactant behaviors in the liquid film include the surfactant adsorption from the bulk onto the air-water interface, and the surfactant convection & diffusion along the air-water interface [40]. Thus, the air-water interface was reported to be partially mobile, which was further characterized into surface rheology features [40–42], including the surface viscosity and surface elasticity. The features are widely reported in foam film experiment in concentrated surfactant solutions with the film life lasted for several minutes [34, 40, 41].

For fast colliding bubbles, the partially mobile boundary condition has seldom been discussed. In most cases, the boundary condition at the air-water interface is simplified into two extreme conditions: whether it is fully mobile or immobile. This simplification has been proven to be reasonable in several research articles [15, 37], and supported by the simulation of Chesters and Bazhlekov [14]. Therefore, three boundary conditions at the air-water interface are considered when deriving the lubrication equations for our systems:

Immobile-immobile boundary condition

Schematic for this boundary condition is shown in Figure 2.2b. On both surfaces, the surface velocity $U = 0$. Experimentally, this boundary condition can be achieved when a sufficient amount of contamination has adsorbed on the air-water interface to inhibit interfacial mobility. This boundary condition has been reported in various publications [15–17, 24] and the equation describing the film flow is given by

$$\frac{\partial h}{\partial t} = \frac{1}{12\mu r} \frac{\partial}{\partial r} \left(rh^3 \frac{\partial p}{\partial r} \right) \quad (2.6)$$

With this boundary condition, the film drainage is slow and it may take seconds for the liquid film to thin and reach the critical rupture thickness.

Immobile-mobile boundary condition

Schematic for this boundary condition is shown in Figure 2.2c. The air-water interface is immobile on one side of the film, but mobile on the other. This boundary condition has been reported in a rising bubble experiment with one contaminated flat fluid surface (immobile) and one fresh bubble surface (mobile) [15]. With the mobile interface in which $\partial U/\partial z = 0$, the following equation can be obtained [43]:

$$\frac{\partial h}{\partial t} = \frac{1}{3\mu r} \frac{\partial}{\partial r} \left(rh^3 \frac{\partial p}{\partial r} \right) \quad (2.7)$$

The film drainage with this boundary condition is 4 times faster than the immobile-immobile case and may lead to a slightly faster bubble coalescence in the same order of magnitude. A detailed description of this model and its validation have been reported [15].

Mobile-mobile boundary condition

Schematic for this boundary condition is shown in Figure 2.2d. In this case, both surfaces are clean and mobile. The equation describing the film drainage has been derived by Davis [44], featured by the velocity U at the interface, which is determined by the continuity of stress at the interface $\tau_f = \mu \frac{\partial U}{\partial z} = \mu_{air} \frac{\partial U}{\partial z}$, μ_{air} is the air viscosity. The drainage rate for this case is given by

$$\frac{\partial h}{\partial t} = -\frac{1}{r} \frac{\partial}{\partial r} (rUh) + \frac{1}{12\mu r} \frac{\partial}{\partial r} \left(rh^3 \frac{\partial p}{\partial r} \right) \quad (2.8)$$

where U is given by [44–46]

$$U(r) = -\frac{1}{\mu_{air}} \int_0^\infty \Phi(r, \omega) \tau_f(\omega) d\omega \quad (2.9)$$

$$\Phi(r, \omega) = \frac{k}{2\pi} \sqrt{\frac{\omega}{2r}} \int_0^\pi \frac{\cos\alpha}{\sqrt{1 - k^2 \cos\alpha}} d\alpha$$

$$k^2 = \frac{2r\omega}{r^2 + \omega^2}$$

This boundary condition has been proposed decades ago [44] and was believed to be responsible for some experimental results [6, 12, 18], but never validated on the film level, leaving a question on its existence.

2.2.4 Initial condition and boundary conditions

The above equations are solved numerically, therefore, suitable initial condition and boundary conditions should be applied. The initial film thickness is given by:

$$h(r, 0) = h(0, 0) + \frac{r^2}{R} \quad (2.10)$$

where $h(0, 0)$ represents the initial separation between the center (apex) of the bubbles.

The film is assumed to be axisymmetric, therefore, the numerical calculation is conducted within a limited region $0 < r < r_m$; where $r=0$ represents the film center, while r_m is carefully selected outside the interaction region to reduce the numerical cost while keeping the model accuracy at the nanometer scale. A detailed description of the selection of r_m can be found in the review paper by Chan et al. [7]. Therefore, the boundary conditions should be considered at $r=0$ and $r=r_m$. With the symmetric liquid film, at $r=0$:

$$\frac{\partial h}{\partial r} = 0 = \frac{\partial p}{\partial r} \quad (2.11)$$

At $r = r_m$, the pressure decay is given as: $r \frac{\partial p}{\partial r} + 4p = 0$. Because of the interaction force, the surface outside r_m also deforms. The deformation is accounted through proper boundary conditions at r_m [24]. There can be various forms for the boundary condition depending on the experimental system. One example for the collision of two bubbles immobilized on solid surfaces with a pinned contact line is given below.

$$\frac{\partial h(r_m, t)}{\partial t} = V - \frac{\alpha}{2\pi\sigma} \frac{dF(t)}{dt} \quad (2.12)$$

where V is the approach velocity and

$$\alpha = 2 \log \left(\frac{r_m}{2\sqrt{R_1 R_2}} \right) + 2 + \frac{1}{2} \left(\frac{1 + \cos \theta_1}{1 - \cos \theta_1} \right) + \frac{1}{2} \left(\frac{1 + \cos \theta_2}{1 - \cos \theta_2} \right) \quad (2.13)$$

where θ_1 and θ_2 are the angles that the bubbles make with the surfaces on both sides. The force $F(t)$ is the sum of hydrodynamic and disjoining forces:

$$F(t) = F_h + F_{\Pi} = 2\pi \int_0^{\infty} [p(r', t) + \Pi(h(r', t))] r' dr' \quad (2.14)$$

In practice, the pressure is integrated from the center until r_m , as the pressure becomes negligibly small outside the interaction region.

2.3 Experimental methods

Various experimental methods have been developed to investigate the bubble collision. According to the classification proposed in the review from Horn et al. [6], these methods can be divided into three general categories: the bubble swarm method, the thin film interferometry method and the bubble pair method. The advantages and limitations of these methods are revised in this section.

2.3.1 Bubble swarm method

The bubble swarm method studies the behavior of a swarm of bubbles in bulk. The bubble collision and coalescence in the swarm are extracted from statistical results about the bubble population or size; both are obtained by direct observation or indirect estimation.

The direct observation of bubbles is achieved with techniques such as the bubble viewer developed by the McGill group [47–50]. A schematic for this instrument is presented in Figure 2.3a [50]. The air bubbles need to be transferred outside the bulk for the observation by a camera. From the images, the bubble size distribution can be extracted. The measured size distribution may slightly differ from the bulk value because of the disturbance during the bubble transfer from the bulk to the observation region.

Indirect techniques are adopted to explore in-situ bubble behavior. For instance, the scatter of a laser signal that passes through a bubble column was used for bubble coalescence analysis (see Figure 2.3b) [51]. By analyzing the intensity of the pass-through laser signal, the in-situ change of bubble size

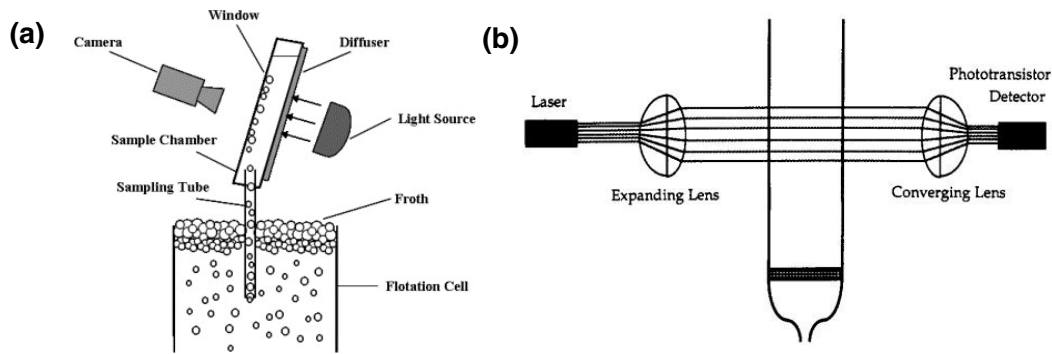


Figure 2.3: (a) Schematic for the McGill bubble viewer(adapted from Girgin et al.(2006),with permission. Elsevier); [50] (b) Schematic for the laser scattering method [51](adapted from Craig et al.(1993), with permission. American Chemical Society).

can be identified. Another example can be found with the analysis of the volumetric percentage of gas (gas hold-up) in bulk [52, 53]. The measured gas hold-up under different experimental conditions can be used to evaluate the variation of in-situ bubble size, although the analysis is more qualitative rather than quantitative. The variation of bubble size reflects the coalescence or breakup of the bubbles in the industrial experimental condition.

Statistical results were shown to be highly reproducible and the bubble coalescence was influenced by various parameters including the aeration rate [54], surfactant type and concentration [47], salt type and concentration [51], agitation [50, 54, 55], etc., However, the relationship between the statistical results and the film thinning and rupture can hardly be quantified. The average bubble collision time, as estimated by Kirkpatrick and Lockett [56], is within 0.12 second. Within this time scale, theoretically, the formation, drainage, and rupture of the thin liquid film are essential to achieve the bubble coalescence. However, the lack of direct observation and the complex coupling of operation parameters, rendered the experimental results difficult to be quantitatively analyzed.

2.3.2 Thin film interferometry method

Direct observation of the thin liquid film can be achieved by the micro interferometry method, in which light with known wavelength or spectra is shone on

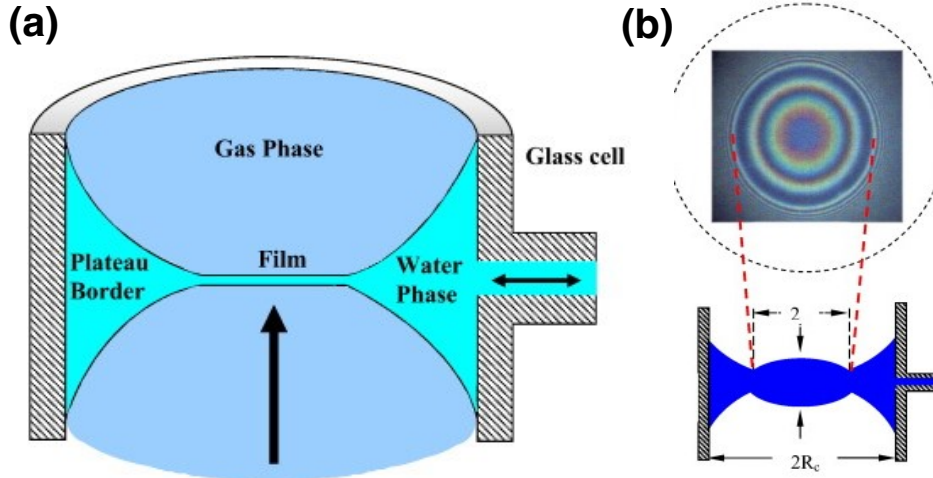


Figure 2.4: (a) Schematic for the ‘Scheludko’ cell [21](adapted from Karakashev et al.(2015), with permission. Elsevier); (b) A snapshot for the observed fringes. [60](adapted from Karakashev et al.(2010), with permission. Elsevier).

the thin liquid film. The light reflected from both film surfaces interferes with each other to change the recorded light intensity, from which we can extract the film profile with nanometer accuracy [21, 23, 57, 58]. Sequential recording of the interferometry images enables the extraction of the spatiotemporal evolution of the thin liquid film from the thickness around a few microns until its rupture. The pioneer observation was conducted by Derjaguin and Kussakov on the thin film trapped between an expanding air bubble and a solid surface [59]. Later on, the micro-interferometry method was extended to the thin film between two fluid interfaces and quickly gained popularity to investigate several fundamental features for foam film drainage. [21, 57, 58]

Figure 2.4a shows a schematic illustration of the Scheludko cell [21, 61]. The liquid film is formed in a well-controlled manner by sucking the liquid out from a special designed porous plate. The interferometry images in Figure 2.4b were recorded by a camera connected to an inverted microscope. By controlling the liquid suction rate, the approach speed of the surfaces can be adjusted. [23, 62] Studies with this instrument help to mimic the thinning dynamic of the foam film at quasi-static drainage process. The surfaces with the concave feature are also used to mimic the colliding air bubbles, whose collision speed is limited within 0.2 mm/s [12, 63], much slower than the bubble collision

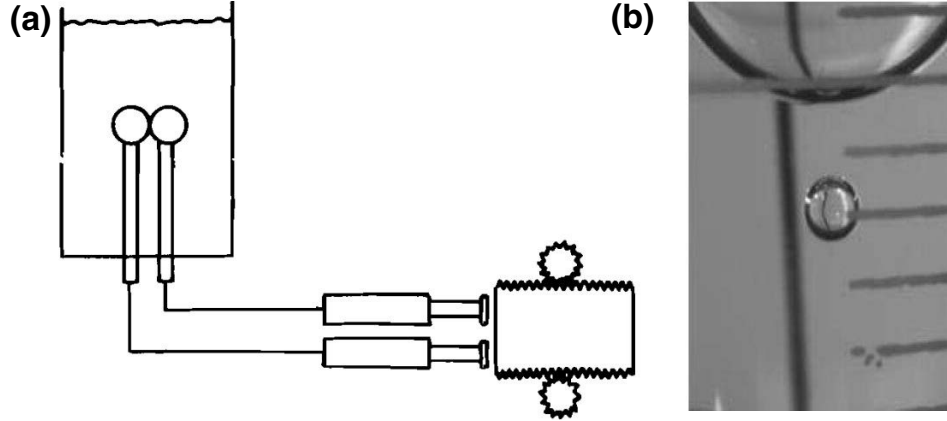


Figure 2.5: (a) Schematic illustration of the bubble pairs generated by adjacent capillaries(adapted from Oolman and Blanch(1986), with permission. Taylor&Francis); [64] (b) Schematic illustration for the rising bubble colliding with the fluid interface(adapted from Castillo et al.(2011), with permission. Elsevier). [18]

speeds in bulk (~ 10 cm/s).

2.3.3 Bubble pair method

The investigation on the collision between two individual bubbles, i.e., the bubble pair method, provides another option to understand the bubble coalescence. An example of this method is shown in Figure 2.5a [64]. With this method, the bubble collision environment and parameters are in good control, while bubble collision with much faster speeds can be achieved when compared to the thin film method. The bubble collision can be achieved in different ways, for instance, by generating bubbles simultaneously from two adjunct capillaries [64, 65], by bringing two bubbles together at controlled velocities [66], or by releasing one bubble to freely hit the other bubble [67, 68] or the flat surface (see Figure 2.5b) [15, 18, 69, 70]. The experimental parameters being investigated include the collision velocity, bubble size, the bubble residence time in bulk, surfactant type and concentration, etc. Typically, the experimental results are analyzed by comparing the coalescence time and the probability of coalescence [6, 18, 65].

Limited information can be obtained from the outcome of bubble collision alone. Therefore, researchers have aimed to extract more information from the

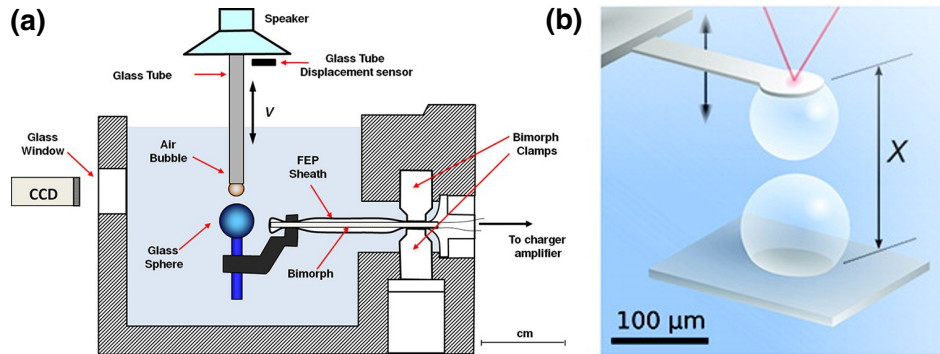


Figure 2.6: (a) Schematic illustration of the integrated thin film drainage apparatus(adapted from Wang et al.(2013), with permission. American Chemical Society); [72] (b) Schematic illustration of the AFM bubble collision technique(adapted from Browne et al.(2011), with permission. American Chemical Society). [73]

dynamic collision process. In the past decade, several successful experiments have been reported using improved experimental techniques together with theoretical modeling. For example, the detailed collision process within milliseconds between a rising bubble and the flat surface can be easily recorded by a high-speed camera [15, 43, 69, 71]. The bubble features captured during the collision, including the bubble rise, deformation, and subsequent bounces were compared to the predictions using a theoretical model [15]. The agreement between the experimental observations and theory predictions helps to understand the film dynamics between the bubble and the flat fluid surface. Another method to obtain dynamic collision information is to measure the interaction force between two colliding bubbles. Figures 2.6 a and b show the force measurement based on an integrated thin film drainage apparatus [72] and an atomic force apparatus (AFM) [16, 73], respectively. The measured force data evolved during the dynamic collision process and agreed well with the theoretical prediction [16, 73], which can be used to deduce the film drainage behavior until rupture.

Results obtained by the bubble pair method significantly advance our understanding of bubble coalescence. The impact of bubble size, collision velocity, surfactant type and concentration, and bubble residence time in the bulk can be clearly distinguished. However, the quantitative understanding of the

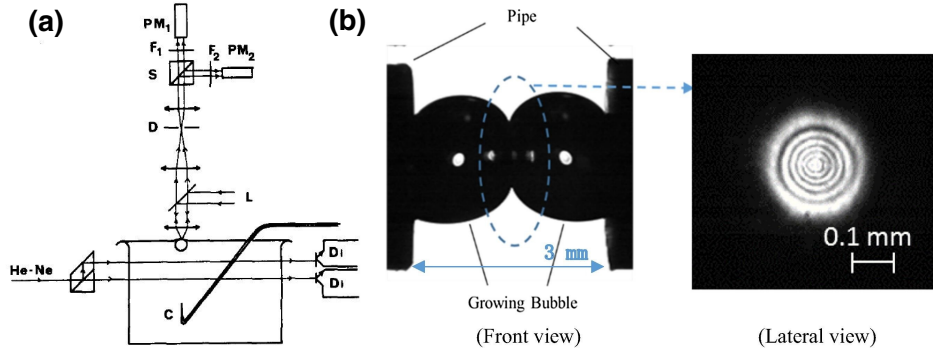


Figure 2.7: (a) Schematic illustration for the rising bubble experimental system by Doubliez (adapted from Doubliez (1991), with permission. Elsevier); [74] (b) Snapshots of the colliding bubbles and the interference fringes (adapted from Morokuma (2018), with permission. Elsevier). [75]

film drainage during the dynamic collision process is still far from satisfactory, with several features that cannot be explained. For instance, the bubble coalescence time at the same experimental condition differs by two orders of magnitude from a few seconds to hundreds of seconds. Secondly, there were several reports about the coalescence of bubble within milliseconds. Moreover, the colloidal stability between the colliding bubbles can only be experimentally achieved in limited cases [6]. There are several hypotheses regarding the abnormal experimental results, but none of them can be fully validated because of the lack of direct information on the film drainage and rupture.

An experimental method with direct film observation is essential to fully unveil the liquid drainage between two fast colliding bubbles. This can be achieved by applying the interferometry method in bubble pair experiments. The pioneering work by Cain [76] conducted thirty years ago successfully obtained thin film interferometry images between two closely growing bubbles. A similar instrument was designed by Morokuma [75] recently, where the interferometry images were recorded between two adjunct growing bubbles at the estimated collision velocity of up to ~ 10 cm/s. Another work reported by Doubliez [74] captured the interference images when a rising bubble hit a flat air-water interface at the collision speed of up to 19 cm/s, from which the film drainage between the bouncing bubble and the flat fluid surface was

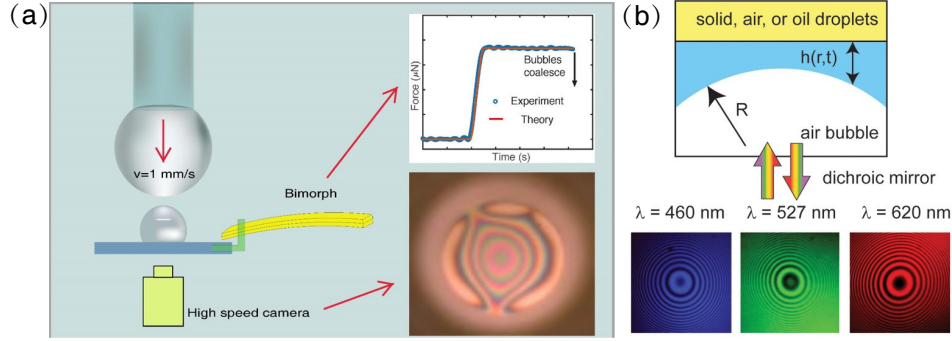


Figure 2.8: (a) Bubble pair interferometry method based on the dynamic force apparatus [79], the insets show the interaction force and the interference fringes (adapted from Liu et al, (2018), with permission. American Chemistry Society); (b) The interferometry method to investigate bubble-bubble collision reported by Gao and Pan (adapted from Gao & Pan(2018), with permission. American Chemical Society). [80]

obtained. A similar technique was adopted by Bhamla [77] to observe the film drainage between rising bubbles and the flat fluid interface in surfactant solutions. There are also some insightful techniques being developed to observe the interference fringes between colliding drops [46, 78].

Although these bubble pair methods with interferometry help to gain insight into the film drainage, a fundamental understanding is still lacking. The thinning of the liquid film is significantly impacted by the dimpled film profile, which was not reported by the early work by Cain [76] and Doubiez [74]. They focused on one point of the film, rather than the overall film profile, leaving several questions unsolved. For instance, the film rupture thickness in their work was reported to range from 200 nm to 500 nm, much larger than the recently accepted value of around 50 nm. The recent work using laser interferometry successfully captured the interference fringes between two growing bubbles [75]. However, there were issues with data interpretation. Overall, there are still several knowledge gaps on bubble coalescence.

In this work, we developed a new method based on the home designed dynamic force apparatus [35, 38] that combines the bubble pair method introduced by Wang [72] and the interferometry technique. As shown in the schematic of Figure 2.8a, an air bubble is immobilized on a transparent glass

surface, while the other bubble is generated at the orifice of a capillary tube. The collision between the bubbles is achieved by driving the capillary tube downward by a motor or a diaphragm speaker at the velocity range from 0.01 mm/s to 50 mm/s. A light is shone on the thin liquid film through the transparent glass and the interferometry images are recorded by a high-speed camera connected to an inverted microscope. Using this design, the various parameters influencing the bubble coalescence can be tested in a well-controlled manner. The parameters include the bubble size, collision velocity, surfactant type and concentration. A similar design using the same concept was presented recently by Pan's group independently (see Figure 2.8b) [80]. From the direct observation of the film drainage between fast colliding bubbles, we expect to understand the remaining puzzles with bubble coalescence.

2.4 Controversies

Although the bubble coalescence process has been extensively studied for decades, there are still many questions that remain unsolved. Figure 2.9a shows a coalescence map from Horn et al. [6] describing the change of coalescence behaviors with the collision speed. The major features include: (1) the colloidal stability is observed at the slow collision speed, but diminished with the increase of the collision speed; (2) A slow viscous drainage zone is defined for the collision velocity below ~ 0.15 mm/s; (3) The rapid inertial drainage zone with rapid bubble coalescence is reported with higher collision velocities.

An illustration of regions described by the map is presented in Figure 2.9b [18], where the three regions can be clearly identified. The experiment was conducted in a specially designed rising bubble technique in which the collision speed can be adjusted [18]. At the slow speed collisions, the bubble lifetime can reach 100 seconds or longer, indicating the colloidal stability of the trapped liquid film. Once the collision velocity exceeds 0.04 mm/s, the coalescence time reduces to 0.1 to 100 seconds, shorter than the colloidal stability region. In the slow viscous drainage region, the coalescence time presented in Figure 2.9b can be qualitatively explained. However, the variation of coalescence time

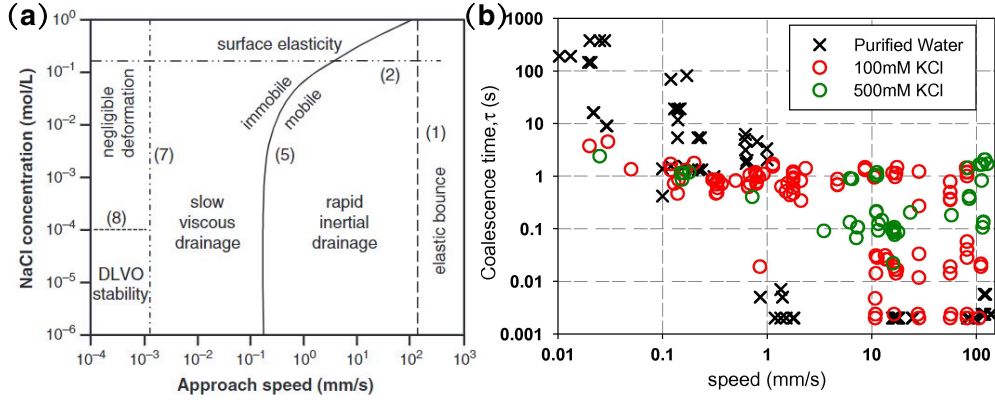


Figure 2.9: (a) The coalescence map by Horn et al (adapted from Horn et al.(2011), with permission. Elsevier). [6] (b) The experimental data shows the variation of coalescence times with collision speeds (adapted from Castillo et al.(2011), with permission. Elsevier). [18]

at the same experimental condition at ~ 0.1 mm/s collision velocity cannot be explained. As the collision velocity exceeds 1 mm/s, the coalescence time drops to 10 milliseconds or less, which is explained by the inertial drainage assuming the mobile boundary condition at the air-water interface. Hypothesis to explain these behaviors has been suggested, but detailed understanding on the film level is still lacking.

2.4.1 Air-water surface charge and colloidal stability

In pure water, air bubbles are negatively charged, with the reported surface potential varying from -30 to -100 mV [12, 81, 82]. The approach of two negatively charged air-water interfaces, as expected from the DLVO theory, should be stopped by the repulsive electrical double layer interaction. Therefore, the two surfaces cannot approach further to rupture unless the repulsive electrical double layer interaction is screened by salt.

Evidence for the above argument can be found with slow speed collisions. Both the colloidal stability and its collapse with the addition of salt in the solution are reported. [12, 18, 83] Impact of the air-water surface charge also manifests on some other thin film studies between an air bubble and a hydrophilic surfaces [35, 38]. However, the coalescence of air bubbles are consistently observed with fast speed collision [6]. The absence of colloidal stability

cannot be well explained with the DLVO theory. Possible explanations may be the air-water surface is less negatively charged [84], or the charge can be redistributed along the air-water interface [85] during film drainage. However, a detailed understanding is still not clear.

2.4.2 Variation of coalescence time at similar experimental conditions

Another noteworthy phenomenon is the variation of coalescence times. At similar experimental conditions including bubble size and collision velocity, the obtained coalescence time can vary by orders of magnitude. One hypothesis that explains this phenomenon is the uncertain boundary conditions at the air-water interface, which can be partially mobile or immobile [18]. As a comparison, a similar variation in coalescence time is observed in a different experimental system, where rising bubbles in perfluorocarbon liquid were collided with a perfluorocarbon-water interface. The boundary conditions at the interfaces are either fully mobile or immobile. However, the variation of coalescence time by two orders of magnitude, similar to the results shown in figure 2.9, is also observed. Another hypothesis to explain this phenomenon is that the film rupture thickness could vary from ~ 50 nm to ~ 150 nm [17].

2.4.3 Rapid bubble coalescence within milliseconds

With higher collision velocities, the coalescence time decreased dramatically to a few milliseconds. This phenomenon is explained by the mobile boundary condition at the air-water interfaces [6, 12, 18]. This hypothesis is highly convincing because the coalescence prediction using the mobile model exactly falls in the same time scale [86]. But the existence of the mobile boundary condition in bubble coalescence is still in debate because of the lack of direct observation on the film dynamics.

Intrinsically, the air-water interface should be mobile in response to the shear stress exerted by the fluid flow. This boundary condition would give rise to the rapid bubble coalescence. However, there are numerous experimental results suggesting that the air-water interface is immobile. Such examples

can be found with colliding bubbles [7, 15, 16], the collision between an air bubble and a solid surface [37, 38, 87], and water drop surface interaction [88]. Even an air bubble with mobile air-water interface during rising exhibited the immobile feature upon its collision with a solid surface [89]. The discrepancy between results leaves a knowledge gap that requires in-depth fundamental understanding.

Chapter 3

Dynamic Interaction Between a Millimeter Sized Bubble and Surface Microbubbles in Water

Abstract

The coalescence between microbubbles and millimeter sized bubbles is an elementary process in various industrial applications such as froth flotation and wastewater treatment. Fundamental understanding of the coalescence behavior between two colliding bubbles requires knowledge of water drainage from the thin liquid film between the deformable air-water surfaces, a simple phenomenon with high complexity in physics because of the interplay of surface forces, hydrodynamic drainage and surface rheology. In this work, we performed simultaneous measurements of the interaction force and spatial thin film thickness during the collision between a millimeter sized bubble (radius 1.2 mm) and surface microbubbles (radii between 30 and 700 μm) at the velocity of 1 mm/s using our recently developed dynamic force apparatus (DFA). The interaction force during the collision agrees well with the prediction from the Stokes-Reynolds-Young-Laplace model with the tangentially immobile boundary condition at the air-liquid interface. However, the measured coalescence times for different bubble sizes are shorter than the model predictions, possibly caused by a rapid drainage behavior along with the loss of symmetry of the thin liquid film. In dozens of experimental runs, the bubbles coalesce at a critical film thickness of 25 ± 15 nm, which agrees reasonably well with the predicted rupture thickness using attractive van der Waals interaction force. These results suggest that the non-symmetric drainage process, rather than the rupture thickness, contributes to the scattering of the experimental coalescence time between two fast colliding air bubbles. Furthermore, our results

suggest that smaller surface bubbles (30-100 μm) are more effective for the attachment onto a large bubble as the coalescence time decreases considerably when the microbubbles are smaller than 100 μm .

3.1 Introduction

The coalescence of air bubbles in water is influenced by the drainage of the thin water film between the deformable air-water interfaces. Thinning and rupturing of the thin liquid film are determined by many factors including bubble size, collision speed, and the presence of surfactants or contaminants[6, 8, 17, 21, 90]. These simple phenomena are physically complex because of the interplay of interface deformation, surface forces, surface rheology, and hydrodynamics[28, 91].

For decades, detailed experimental and theoretical investigations were conducted to understand the thin film drainage at the static or quasi-static conditions, where the roles of surface forces and surface rheology in film thinning are well characterized[20, 21, 57, 92]. However the understanding of the dynamic collision between two bubbles was limited because of the difficulty in obtaining quantitative experimental results[57]. Advances in experimental methods and theoretical modeling in the past decade enabled the further exploration of the dynamic collision of two microbubbles, where the role of hydrodynamic effect was highlighted[91]. Unfortunately, the coalescence between a millimeter sized bubble and a surface microbubble, a key feature in many industrial applications such as flotation and wastewater treatment, has rarely been investigated.

Bubble-bubble interactions in these industrial applications are characterized by a wide range of bubble sizes from micrometers to centimeters with the high collision velocity of millimeters or even centimeters per second. Manipulation of bubble size has been explored extensively to facilitate these industrial processes. For instance, the presence of small bubbles on the surface of mineral particles (i.e., surface microbubbles or surface nano-bubbles) is expected to facilitate the large bubble-particle attachment in mineral flotation[93–95]. However, the fundamental understanding of this dynamic process is limited because of the difficulty in obtaining direct and reliable experimental data at such high dynamic conditions with two deformable air-water interfaces. Static or quasi-static bubble coalescence data provide limited information to the dynamic collision, because the variation of bubble deformability with respect to

the bubble size, the dominating role of hydrodynamic pressure, and the possible variation in surface mobility because of the liquid flow are not considered in the static conditions[6, 12, 85, 96].

For a long period, the only measurable quantity for bubble collision at millimeters per second was the lifetime of the colliding bubbles[57]. Some insightful results about the roles of bubble size, collision velocity and surface rheology were reported in the past decade[6, 8, 97]. Recent advances in experimental[70, 98, 99] and theoretical modeling [17, 100] allowed the investigations of the bubble bouncing behavior of a rising bubble at the air-water surface. However, experimental results from different groups[17, 101] have shown wide variations in the bubble coalescence time by orders of magnitude, which provides an opportunity for further quantitative understanding.

One method to achieve the quantitative evaluation of the dynamic bubble collision process is to measure the interaction force between two colliding bubbles. In the past decade, significant progress has been made using the atomic force microscopy (AFM) bubble probe technique[16, 73], whereby the interaction force between two microbubbles below 100 μm in size, or between a microbubble and a macro-bubble surface[102], was measured at a collision velocity up to 50 $\mu\text{m}/\text{s}$. The nano-Newton scale force data measured at the highly idealized experimental condition, explained with a suitable theoretical model, provides insights into the film drainage with highly coupled contributions from surface forces and hydrodynamic effects. However, the variation in bubble size and collision velocity in many industrial conditions surely exceeds the scope of the instrument reported in the literature. The force measurement in micro-Newton scale using a bimorph cantilever seems to be promising for large bubbles following its recent application in studying bubble-solid interaction[35], it has been suggested that bubble-bubble interactions can be explored using this technique[72].

From the experimental perspective, water drainage from the thin liquid film between the deformable air-water surfaces is best explained quantitatively by capturing the spatiotemporal evolution of the film thickness from a few microns to the nanoscale. Techniques to measure the thin film thickness were

initiated by Derjaguin and Kussakov between mica and bubble surfaces[59] , and highlighted by the design of the ‘Scheludko cell’[61], where the interference fringes between two air-water interfaces were observed using reflection interference contrast microscopy (RICM). Experiments with the ‘Scheludko cell’ were referred to as the collision between millimeter sized bubbles or foam film, at a controlled collision speed varying from quasi-static to $200 \mu\text{m/s}$ [12, 63]. The thin film evolution behavior at a faster collision speed with various bubble sizes, although attempted by researchers [103], has not been clearly captured.

In this work, we performed simultaneous measurements of the interaction force and spatial thin film thickness during the collision between a millimeter sized bubble (radius 1.2 mm) and microbubbles (radii 30 - 700 μm) at a velocity of 1 mm/s using our recently developed dynamic force apparatus (DFA), which was named integrated thin film force apparatus (ITLFFA) in the previous publication[35]. Measurement of the interaction force in micro-Newtons using a bimorph cantilever allows faster collision and larger surface deformations than AFM measurements. The observation of the interference fringes between two fast colliding bubbles was successfully recorded by the combination of inverted microscopy and high-speed photography, which enables us to get the direct information about the spatiotemporal evolution of the thin film thickness. The focus of this work will be on the role of bubble size on liquid drainage from the thin film and bubbles coalescence. The developed experimental method with quantitative data together with theoretical analysis provides new insights into the dynamic collision and coalescence between a millimeter sized bubble and surface microbubbles.

3.2 Experimental section

3.2.1 Materials and methods

The water used for the experiment is Milli-Q purified water with a resistivity of 18.2 M Ω -cm at 25 °C and a viscosity of 0.89 mPa·s. Potassium chloride (KCl) of ACS grade, purchased from Fisher Scientific, was roasted in an oven

at 600 °C for 8h to remove the organic impurities prior to the preparation of the KCl solution. The 1 λ fused silica window purchased from Edmund Optics is used as the transparent substrate. The silica window was pre-washed by the piranha solution ($H_2SO_4 : H_2O_2 = 3 : 1$) for 1 hour, then hydrophobized using octadecyltrichlorosilane (OTS, 95+%) to obtain the contact angle $\sim 100^\circ$.

3.2.2 Experimental system

The schematic of the DFA is presented in Figure 3.1. A stainless-steel chamber filled with KCl solution is placed on the stage of an inverted Axiovert 100 Carl Zeiss microscope. A millimeter bubble generated at the capillary orifice is pushed downward by a motor actuator (THORLABS, Z825B) at the speed of 1 mm/s toward a microbubble immobilized on the silica window. The radius of the top bubble is monitored by a side view charge-coupled device (CCD) camera and adjusted by a gas tight syringe to maintain a stable radius of 1.20 ± 0.01 mm. The surface bubble immobilized on the substrate is generated using a custom-made ultra-sharp pipette. The radii of the surface bubbles vary from 30 μm to 700 μm . Head to head collision between two bubbles is achieved by carefully alignment monitored by the inverted microscope. For comparison, the initial gap between the top bubble and the surface bubble is monitored by the side view CCD camera, whereby the moving distance of the top bubble is set accordingly to achieve the relatively constant overlap of 250 μm between two bubbles. When the overlap is achieved, the system is held at that configuration until the end of the experiment.

During the experiment, a bimorph cantilever (force resolution 0.1 μN , 10000 force points per second) attached to the silica window is used as the force sensor. A high-speed camera (Photron SA4, 60 fps-500000 fps) is connected to the inverted microscope to record the interference fringes synchronized with force measurement. A halogen lamp (Hal100, Zeiss) is used to shine white light for the interference fringes. It takes several attempts to get proper camera focus during the experiment because of the deformability of both surfaces. On the other hand, very clear interference fringes would be obtained once a reasonably good focus is achieved because of the big difference in refractive

indexes of water and air. The film thickness is calculated from the interference fringes using the method introduced by Scheludko[61]. In addition to these experimental results, detailed information about the acceleration, deceleration and speed variation of the top bubble are monitored synchronously with experiments using a deflection sensor with $5 \mu m$ sensitivity. This experimental velocity is adopted in the theoretical modeling for a better comparison with experiment. Over 50 experimental runs are reported in this paper.

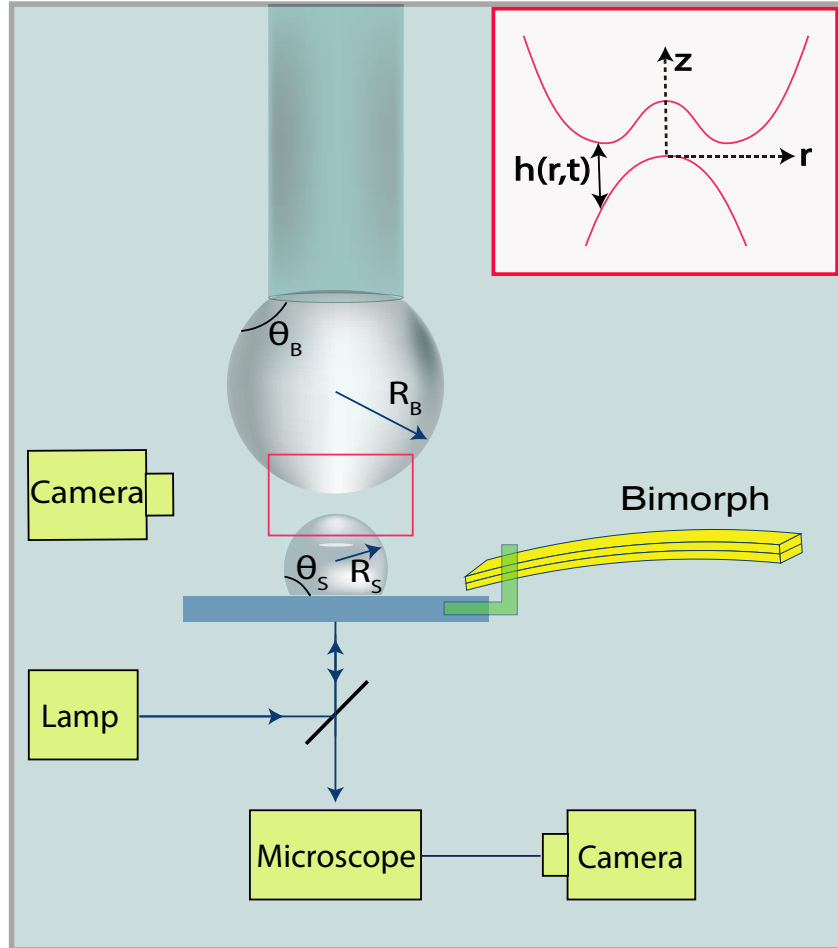


Figure 3.1: Schematic illustration of the experimental system, a millimeter bubble is generated at the end of a glass capillary. The capillary is moved downward towards a surface microbubble immobilized on a transparent hydrophobic surface. The interaction force is monitored by a bimorph cantilever during the bubble collision. The thin liquid film entrapped between the two bubbles is monitored by interference fringes through an inverted microscope connected to a high speed camera. The inset illustrates the surface deformation; the coordinate system and the film thickness $h(r, t)$ are defined.

3.3 Description of the theoretical model

Quantitative understanding of the dynamic process is achieved using the Stokes-Reynolds-Young-Laplace (SRYL) model where the liquid drainage is described with the Reynolds lubrication theory, while the surface deformation is described by the augmented Young-Laplace equation. Assumptions as well as equations in the model are given in the appendix. This model has been successfully applied to understand the collision force measured by AFM between two microbubbles [16, 73]. Perfect agreement of the nanoNewton scale forces between the AFM measurement and the SRYL model prediction helps to distinguish the relative importance of surface forces and hydrodynamic force in the dynamic bubble collision. Moreover, agreements between SRYL model prediction and experimental results have been confirmed on the thinning and deformation behavior of the thin liquid film trapped between an air bubble and solid surfaces[7, 35, 72, 85]. Interestingly, the agreement is not limited to the low-speed collision at the micrometer scale[28, 104] with a small bubble Reynolds number ($Re_B = \frac{2R\rho V}{\mu}$, here R is the bubble radius in millimeter scale, V is the bubble approaching velocity, ρ and μ are the density and viscosity of water respectively.) , but also valid for the high speed collision at centimeter scale with a global Reynolds number possibly exceed 100.[17, 35, 37, 105] The reason for the wide applicability of the model is that the Reynolds number of the thin liquid film ($Re_f = \frac{h_f V_c}{\mu}$, where h_f is the film thickness, V_c is the air-water surface velocity.) is much smaller than unity as a result of the small film thickness (h_f) in micrometer or nanometer scale[37]. Being validated by many experimental data, the model has been adopted to gain better understanding towards the bubble coalescence behavior without quantitative experimental results like interaction force and film thickness, such as in understanding in the bouncing and coalescence of a bubble rising toward an air-water surface.[17, 100].

Two assumptions of the model are: axisymmetric interaction, which is achieved by careful alignment of the bubbles (See Figure A.2), and the immobile boundary condition at the air-liquid interface. The surface is easily

immobilized by a tiny surface tension gradient on the surfaces, while the air-water surface would be easily contaminated[8, 12, 17]. In several recently published works, the assumption of immobile surface property is still valid at very high collision velocities[17, 35, 37]. Therefore we use an immobile condition for modeling since we keep a similar level of cleanliness in this experiment as those reported works. This assumption is also validated by our experimental results.

The components of the disjoining pressure should be carefully justified for the modeling work. The repulsive electric double layer (EDL) interaction and the attractive van der Waals(VDW) interaction described by the classical Derjaguin-Landau-Verwey-Overbeek (DLVO) theory[31] were widely used in modeling surface interactions. For the bubble-solid surface collision at high approaching velocities[35], precise agreements have been achieved between experimental observation and theoretical prediction for the dynamic film thinning behavior. Furthermore, the experimental equilibrium thin film thickness agrees with the prediction of the DLVO theory.

When dealing with the bubble-bubble system, the attractive VDW interaction should be included in the model since it is believed to be the driving force for thin film rupture[16]. But the effect of repulsive EDL interaction should be carefully evaluated. In milli-Q water or aqueous solution with low salt concentrations, the classical DLVO model including the EDL interaction would predict a stable thin liquid film. But in experiments, the film stability between two air bubbles was only observed in the static or quasi-static collisions with extremely low approaching speeds. [12, 16, 101]The consistent coalescence behavior between two bubbles colliding at high velocities [6, 17, 19, 85, 96] suggests the EDL interaction is unable to prevent the film from rupturing, although the mechanism has not been fully understood. The coalescence of bubbles are consistently observed in our experiments using aqueous solutions with different salt concentrations from milli-Q water to 500 mM. Therefore, the EDL interaction in the classical DLVO theory[31] was not included in the comparisons between the SRYL model and the experimental results.

3.4 Results and discussions

We provide an example of the motor displacement in a typical experimental run in Figure 3.2A. The negative sign of the displacement value indicates the downward movement of the motor and the top bubble. The top bubble was driven toward the surface bubble at point o', after colliding with the surface bubble at point a, the top bubble was driven further until the required overlap between the bubbles was achieved, hereafter the system was held at the same configuration until the end of the experiment. The velocity profile of the top bubble movement is shown in the inset of Figure 3.2A where the acceleration and deceleration of the motor during the operation are identified. We ensured the expected approach velocity of 1 mm/s at the early stage using a reasonable initial separation in experiment to avoid the impact of the motor acceleration, while the unavoidable impact of motor deceleration was considered in the theoretical modeling.

The simultaneous measurements of interaction force and interference fringes in this experimental run are shown in Figures 3.2B and Figure 3.3, respectively. In Figure 3.2B the interaction force is reported from the beginning of the movement of the top bubble, until the formation of a capillary bridge formed by the merged bubbles. In Figure 3.3, some selected snapshots from the recorded interference video are shown to highlight the thin liquid film behavior during the dynamic process. The time for each snapshot in Figure 3.3 corresponds to the same time in Figure 3.2B.

To facilitate the comparison between experiments, as shown in Figure 3.2 A and B, the time point a is selected as time 0 because it is the time of the start of the repulsive interaction force, also the time for the initial observation of the flattening of the film from the microscope. Generally, we divide the dynamic interaction into 4 stages based on the force and fringe characteristics: (I) Negligible net force measured at a large separation distance, also no fringes observed; (II) A rapid increase of the repulsive force from point a to b, the force is a result of the hydrodynamic pressure between two close surfaces with a separation distance below 2 or 3 μm . In the example given in Figures 3.2 and

3.3, the force increases from 0 ms to 340 ms with the simultaneous expansion of the thin film area between these two bubbles. The measured force is proportional to the area of the thin film, although the relative importance of surface forces and hydrodynamic repulsion evolves with time and film thickness[35]; The growth of the dimple profile, a symbol of the reversed bubble surface, is clearly shown in Figure 3.3. (III) From point b to point c, the interaction force remains constant as the bubble stopped approaching; in this period the thin liquid film maintained a constant diameter while the liquid kept on draining out. (IV) From point c to point d, a strong attractive force was measured, indicating the formation of a capillary bridge after the coalescence of two bubbles. Film rupture happens at point c and the time from point a to point c is defined as the coalescence time.

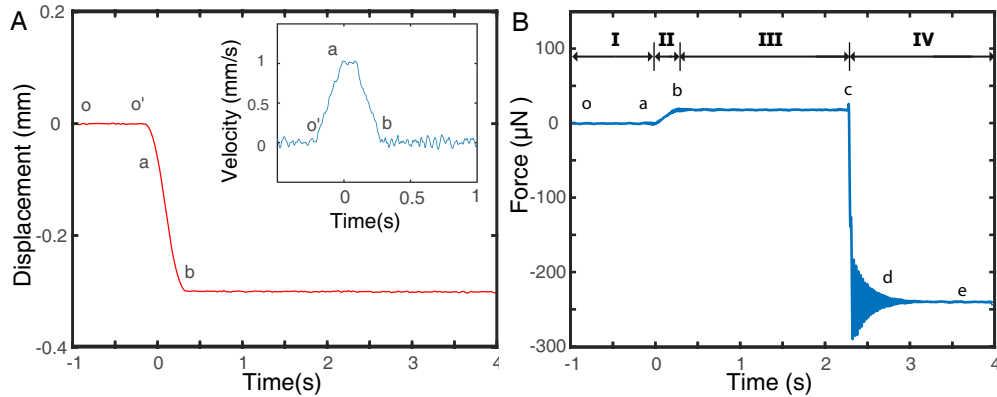


Figure 3.2: Typical (A) displacement curve and (B) force profile during a measurement run between a millimeter bubble ($R_B = 1.2$ mm) and a micrometer bubble ($R = 550$ μ m) immobilized on the surface of hydrophobic silica at the approach velocity of 1 mm/s. The raw data are smoothed using a Matlab function. The interaction force is divided into four stages as time progresses, with a repulsive force before coalescence followed by an attractive capillary force after the rupture of the thin liquid film. The dash lines refer to the initial collision point.

As shown in Figure 3.3, interference fringes with axisymmetric structure are observed during the approaching stage, with a clear information about the formation and expansion of the dimpled thin film area. Once the top bubble stops approaching, ideally, the liquid would drain out slowly and symmetrically until the thinnest part at the rim reaches the critical thickness for film rupture,

as was observed between two glycerol drops in very viscous silicon oil[46]. But the axisymmetric drainage until rupture, although tried carefully, was never observed in our experiment. In the experiment shown in Figure 3.3, the thin film suddenly lost its symmetry starting from 430 ms. A considerable amount of the trapped water flowed out in less than 20 ms from one small channel, as if an ‘express exit’ was formed. After that, the film rebuilt its symmetry with a small amount of liquid remained in the film. The loss of symmetry happened again with the formation of new ‘express exit’ before the black film was seen. Formation of the ‘express exit’, although much faster in this work, is similar to the results with oil or air obtained by the Scheludko cell[12, 106]. The ‘express exit’ phenomena might be a result of the unavoidable minor offset between two bubbles in the experiment, although special efforts have been taken for the alignment, or it can be a consequence of the local mobility at the air-water surface because of the shear stress at the interface[85]. Further investigations to better understand this phenomenon are necessary because it is closely related to industry processes such as mineral flotation and waste water treatment.

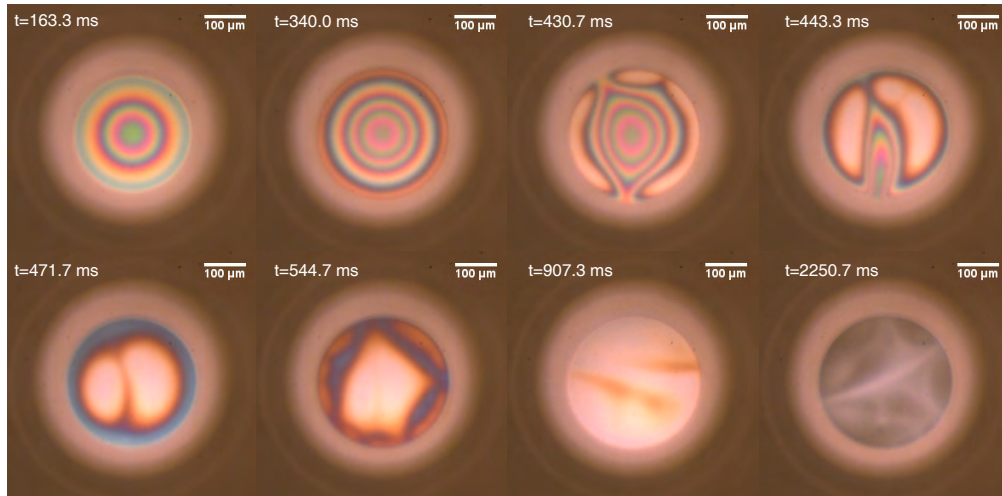


Figure 3.3: Snapshots of the interference fringes between a top bubble ($r = 1.2$ mm) and the surface microbubble ($r = 550 \mu m$) recorded at 3000 frames per second. Detailed information about the gradual expansion of the symmetric film, the unexpected lose of symmetry, and the black film before rupture are shown in sequence. The times for the snapshots here correspond to the same times in Figure 3.2B.

Two quantified experimental measurements, namely interaction force and interference fringes, can be obtained with this experimental method. The easily achievable and reliable measurement of the interaction force, with a suitable theoretical model, enables us to get an insight into the dynamic collision process with valuable information such as overlap area and bubble deformation. However, using the interaction force alone would not provide the full picture, since the non-symmetric drainage behavior is not provided in the force data. The interference fringes with overall and local information about the spatiotemporal evolution of the thin film thickness, although challenging to record experimentally, would provide detailed information about the drainage behavior. The combination of these two methods enables a better understanding about the dynamic interaction between two air bubbles in water.

For tiny microbubbles, the liquid drains out so fast that the observed force is still increasing when film rupture occurs (see Appendix A.2). The stable stage does not occur until a transition surface bubble radius around $100\ \mu\text{m}$. In experiments with a stable force measured at the third stage of the dynamic process, as shown in Figure 3.4, the interaction force seems to be relatively constant between $15\ \mu\text{N}$ and $30\ \mu\text{N}$, and the slope of the force curves are almost identical for most cases. This suggests that a reasonable operation procedure is maintained in the experiment for comparison of results. The wave fluctuation of the measured force shown in Figure 3.4 is noise from the bimorph as it is clearly observed for two bubbles far apart. Other than this, a perfect agreement on interaction force is observed between the SRYL model prediction and the experimental measurement. This indicates that the overall interaction area between the two bubbles, the critical factor determining the interaction force, is perfectly captured by the model. Furthermore, the key features in dimple formation, including the initial flattening of the surface and the expansion of the interaction area were also reasonably captured by the model prediction. The tangentially immobile boundary condition used in the model is thus validated by the agreement between the experimental results and model prediction.

The impact of bubble radius on coalescence time is described in Figure

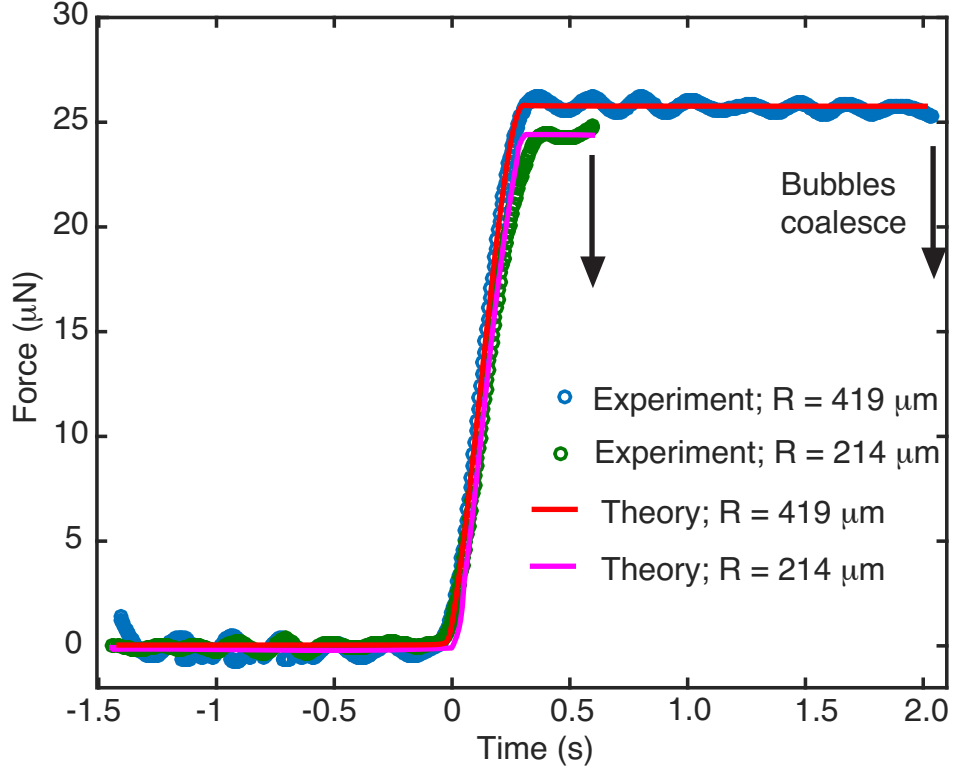


Figure 3.4: Experimental measured force (circles) vs SRYL prediction (solid lines) for two different bubble sizes. The force rises quickly during the approaching stage and remains constant during the holding stage until coalescence happens. In this plot, the theoretical curve was computed using the experimental time and stopped when the bubbles coalesced in the experiment.

3.5 Here, the experimental coalescence time is defined as the period between the initial collision and the bubble coalescence (point a to point c in Figure 3.2B). The determination of the theoretical coalescence time by the SRYL model with VDW only is described in detail in the appendix A. According to the experimental results, the coalescence time increases sharply with the surface bubble radius. To be more specific, it takes less than 400 ms for a surface bubble smaller than $100 \mu\text{m}$ to coalesce with the top bubble, while the same process takes more than 1000 ms for surface bubbles larger than $300 \mu\text{m}$. Obviously, the coalescence is quicker with a smaller surface bubble. The overall trends for experiments in different salt concentrations are similar, while the slightly shorter coalescence time is observed for experiment in milli-Q water. Nevertheless, the difference is not easily distinguished from the mea-

surement scattering that arises from the non-symmetric drainage behavior. It is noteworthy that the coalescence times reported here indicate reproducible and reliable results. Similar experiments have shown much wider variations of coalescence times[17, 19]. The theoretical model, that assumes symmetric drainage, tangentially immobile boundary condition and VDW as the dominant attractive force that causes film rupture, predicted a coalescence time longer than the experimental one. According to Figure 3.5, the theoretical prediction works as an upper bound for the experimental data.

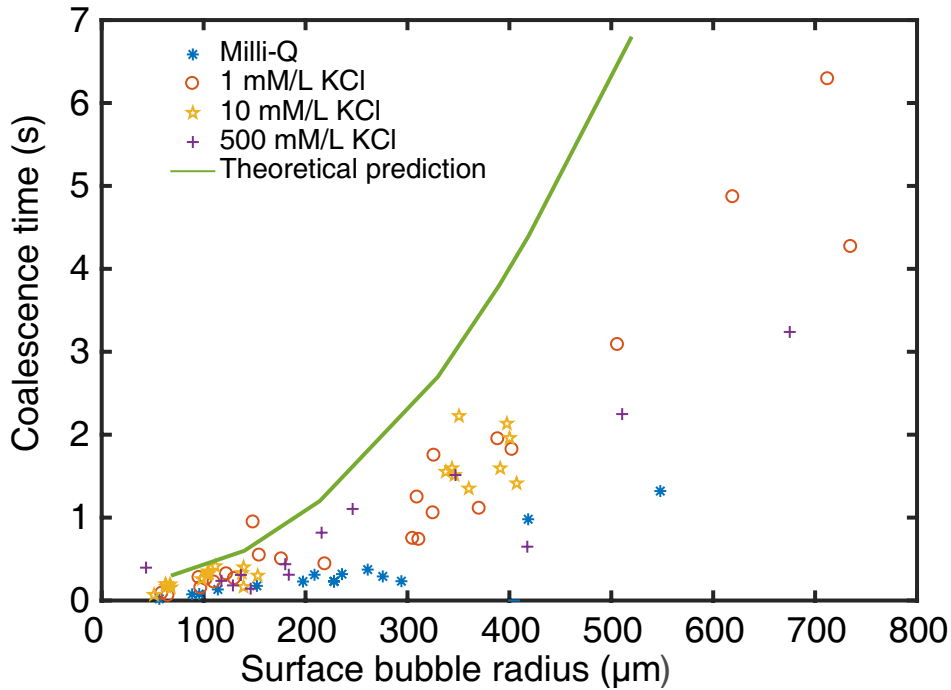


Figure 3.5: Coalescence time vs surface bubble radius in various aqueous salt solutions. The solid line is the theoretical prediction using SRYL model. The approach velocity is 1 mm/s, the radius of the top bubble is 1.2 mm.

The experimental rupture thickness as a function of bubble radius is shown in Figure 3.6. From the thinnest area of the thin film at the time of rupture we take the average of 9 pixels ($6 \times 6 \mu m^2$) to diminish the possible noise and plot the evolution of the light intensity over time. By taking the maximum and minimum intensities we can estimate the rupture thickness[58, 107]. Interestingly, the rupture thickness is consistent across different bubble sizes. Though the error in these values can be large, they can all be either larger or shorter,

rupture thicknesses in the order of 25 ± 15 nm were consistently observed. The measured rupture thickness is consistent with the reported works[107] using the ‘Scheludko cell’.

Previously, the large spread of coalescence time by orders of magnitude was attributed to the existence of surface active contaminations, the statistic nature of this phenomena or the variation of the critical film rupture thickness[17, 19, 97]. According to this experiment, it is suggested that the film ruptures at a critical film thickness of 25 ± 15 nm, indicating of a consistent rupture mechanism. The coalescence time is scattered because of the drainage process that the thin film loss its symmetry which allows the liquid to drain out quicker in an unexpected manner.

The underlying mechanism for the role of bubble size on bubble coalescence is discussed using model prediction and experimental results. As is known, the liquid film ruptures once the thinnest part reaches the critical thickness. In an ideal system, which is axisymmetric, the thinnest part in the dimpled thin liquid film should be at the rim. The model predictions of the rim thickness as a function of time at different surface bubble radii are given in Figure 3.7. For all the examples given, the thinning of the rim is basically divided into three stages: (1) a rapid thinning stage until a rim thickness below 100 nm; (2) a gradually thinning stage and (3) rapid film rupture by the VDW attractive force. Note that the thickness where the VDW becomes relevant and quickly pulls the interfaces is roughly 20-30 nm, a result that is consistent with the experimentally measured rupture thicknesses.

It is evident that the bubble size has a significant effect on coalescence time. For a small surface bubble of $68\ \mu\text{m}$, the first stage takes less than 100 ms until a rim thickness around $60\ \mu\text{m}$, followed by a short slow drainage stage until the film ruptures at the critical thickness. For a larger surface bubble at the radius of $419\ \mu\text{m}$, the first stage stops at a rim thickness around 100 nm after a rapid thinning for about 600 ms, then it takes more than 1000 ms for it to reach the critical rupture thickness. In conclusion, the advantage of small bubbles in short coalescence time might be explained by the fast drainage of liquid film.

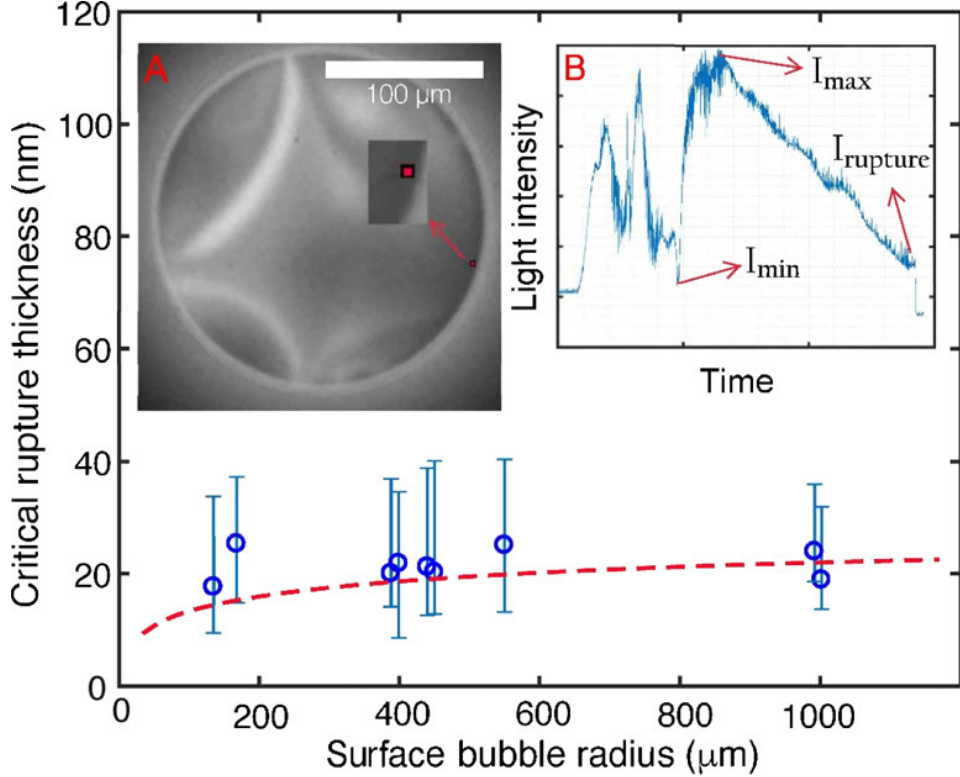


Figure 3.6: Critical rupture thickness vs bubble size in various aqueous salt solutions. The inset A shows the pixel points taken from the critical rupture. The average of 9 pixels ($6 \times 6 \mu\text{m}^2$) are plotted to show the evolution of light intensity over time in inset B. The blue circles are the critical rupture thickness calculated based on the light intensity. Two data points from the surface bubbles around 1 mm in radii are also included. A method for the estimation of the upper and lower bounds for the critical rupture thickness is described in the Appendix A. The red dashed line is the dividing line where the disjoining pressure (VDW interaction) equals the Laplace pressure.

When compared with the theoretical prediction, the experimental coalescence times are shorter (marked as squares symbols in Figure 3.7) because of the loss of symmetry. The insert in Figure 3.7 shows detailed information about the thinnest and thickest parts of the thin liquid film, in which the theoretical value are the rim and center thickness of the dimpled liquid film respectively, while the experimental values were found by analyzing the images. The experimental film thickness of the thinnest and thickest parts agree reasonably well with the model prediction at the early stage where the liquid film remains axisymmetric. Once the film loses its symmetric, the center film

height drops dramatically because a considerable amount of liquid drains out through the ‘express exit’. The thickness change of the thinnest part is less obvious, but an acceleration of the thinning process is also observed. The liquid film ruptures once the thinnest part reaches the critical rupture thickness.

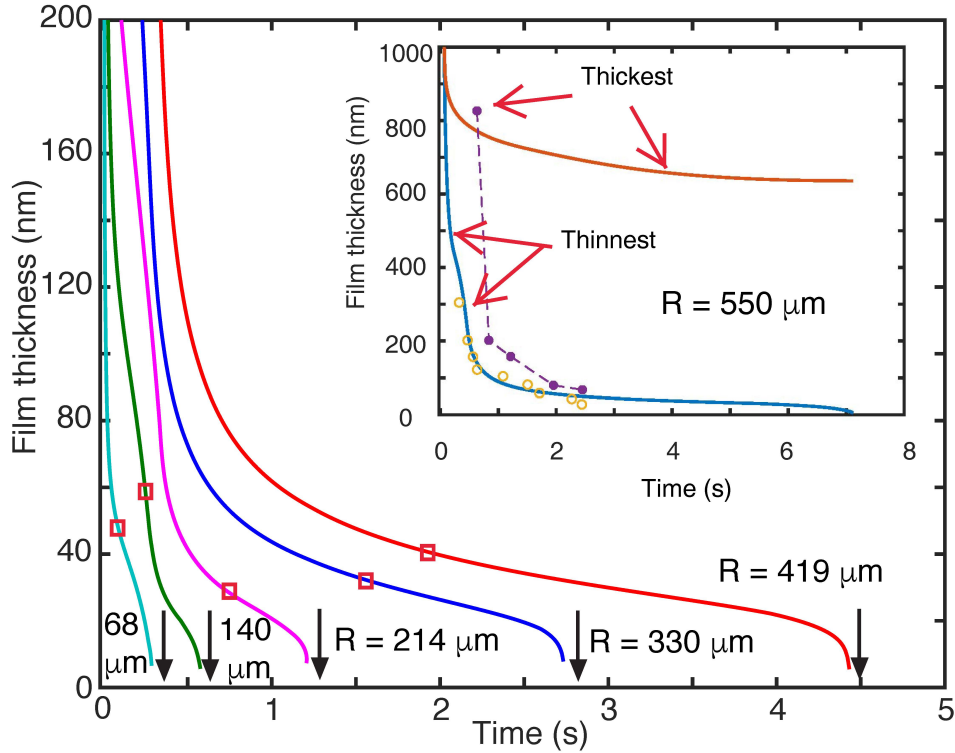


Figure 3.7: Rim thickness vs time according to the SRYL model prediction. Square dots indicate the experimental coalescence times for these cases. The inset shows comparison between theory (solid lines) and experiment (symbols) for the thickest and thinnest parts of the film. The dash line is a guide for the eye.

In Figure 3.8, we reconstruct the shape of the bubbles based on the theoretical calculations. In general, the small bubble deforms very little because of its large Laplace pressure and mostly keeps its spherical shape and indents into the big bubble during the experiment while the big bubble inverted its shape in the order of $50 \mu\text{m}$ for the reported case.

A better understanding of bubble coalescence might be achieved based on the experimental results and theoretical predictions in this study. The coalescence of two bubbles colliding at high velocity in water is inhibited by the

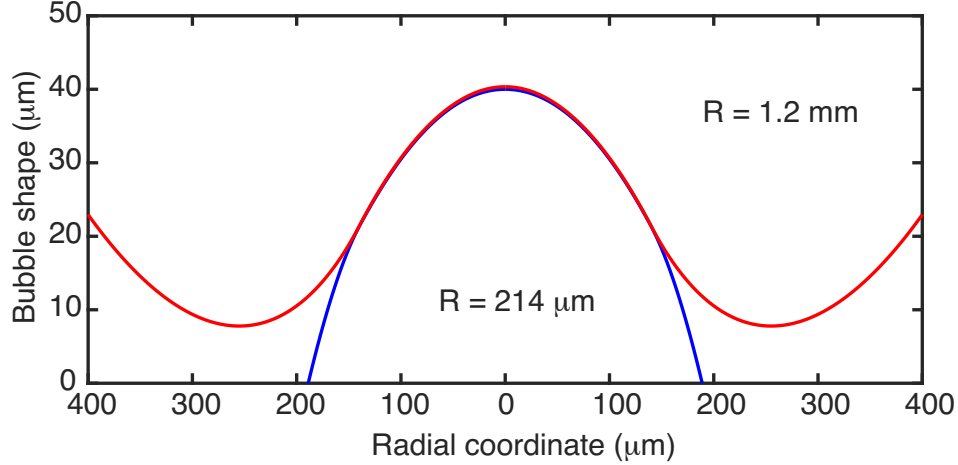


Figure 3.8: The shape of small and large bubbles predicted from the model just before coalescence.

trapped liquid in the dimpled thin film because of the hydrodynamic pressure. Drainage of the liquid film is significantly accelerated by the decrease of bubble size, while the loss of symmetry of the thin film in the experiment contributes to faster drainage than the theoretical predictions using the axisymmetric assumption. Interestingly, the film keeps draining until a critical rupture thickness of 25 ± 15 nm regardless of the loss of symmetry. The measured critical rupture thickness agrees well with the theory using VDW interaction as the rupture mechanism. The puzzle of the wide scattering of experimental coalescence times between two fast colliding bubbles, which has been reported in many papers, is reasonably explained with the loss of symmetry phenomena based on our quantitative experimental results.

3.5 Summary

The spatiotemporal evolution of the thin liquid film drainage and the interaction force between two colliding bubbles of different size were measured simultaneously in our experiment. Experimental data of coalescence times indicated that small bubbles favored faster coalescence when compared with larger bubbles. The effect of bubble size is significant in the hydrodynamic drainage process because of the change in Laplace pressure. The SRYL model with the

immobile boundary condition capture the main features of the interaction force and the dimple formation. The direct observation of the film thickness in this work reveals a non-symmetric drainage behavior of the trapped liquid in the dimple that provides a reasonable explanation for the scattering of experimental coalescence time. The unexpected faster flow in the dimple drainage process is probably a consequence of a slight misalignment between the bubbles or a local change in boundary condition because of shear stress and is responsible for shorter coalescence time. This experimental technique can be easily applied to other systems such as drop-drop coalescence and bubble-drop attachment.

Chapter 4

Coalescence of Bubbles with Mobile Interfaces in Water

Abstract

The fluid flow inside a thin liquid film can be dramatically modified by the hydrodynamic boundary condition at the interfaces. Aqueous systems can be easily contaminated by trace amounts of impurities, rendering the air-liquid interface immobile, thereby significantly resisting the fluid flow. Using high speed interferometry, rapid thinning of the liquid film, on the order of the collision speed, was observed between two fast approaching air bubbles in water, indicating negligible resistance and a fully mobile boundary condition at the air-water interface. By adding trace amounts of surfactants that changed the interfacial tension by 10^{-4} N/m, a transition from mobile to immobile was observed. This provides a fundamental explanation why the bubble coalescence time can vary by over three orders of magnitude.

4.1 Introduction

When two air bubbles collide with each other, they may bounce and keep their original volume or merge into a larger one. The collision of air bubbles plays a pivotal role in many fields including oil and gas extraction, mineral flotation and water purification, even though the expected outcome varies with industries. For example, large bubbles are desired for drag reduction [108], whereas microbubbles are beneficial for froth flotation [1]. Bubble coalescence occurs when the trapped thin liquid film reaches its critical rupture thickness, typically in the order of 50 nm [6, 79]. Within a dynamic collision process with limited time (~ 0.01 - 0.12 s) [56], the crucial factor determining the bubble collision is the film thinning rate [6], which is influenced by bubble size, collision velocity, non-symmetric drainage, and most importantly, the hydrodynamic boundary condition at the interface [6, 8, 16, 17, 79, 109]. The latter may be tangentially immobile (zero tangential velocity at the air-liquid interface due to the presence of contaminants or surfactants) or fully mobile (when the air-liquid interface cannot sustain any shear stress, as is the case of bubbles in pure water).

The mobility of air-liquid interfaces has been utilized for drag reduction by using super-hydrophobic surfaces in micro-fluidics [39, 110] or covering falling spheres with an air layer [111]. Theoretically, the film thinning rate between two bubbles with mobile interfaces can be three or four orders of magnitude faster than that with tangentially immobile interfaces [86]. Though the existence of mobile air-water interfaces in bubble coalescence is still controversial, experiments have found instances of rapid bubble coalescence in milli-seconds [6, 18], which was hypothesized to be a result of interface mobility without any evidence on a film level. However, direct observations of the spatiotemporal thinning of the thin liquid film using interferometry, when compared with theoretical prediction, have thus far consistently confirmed the immobile air-water boundary condition. Experimental data were obtained for the interaction between an air bubble and hydrophilic/hydrophobic surfaces over a wide range of Reynolds numbers [24, 35, 37, 89], and between two

bubbles in quasi-static or dynamic conditions [79, 80, 109]. Phenomenological features of the thinning film, including the inversion of curvature (dimple) and the dynamic evolution of the dimple profile, agreed well with theoretical prediction assuming the immobile boundary condition [37]. Even freshly generated bubbles with fully mobile surfaces during rise in bulk exhibited an immobile boundary condition when colliding with a solid surface [24, 89]. The discrepancy between experiments leaves a gap in researchers’ understanding of air-water interfaces.

In this letter, we report bubble collision experiments using high speed interferometric images that provide quantitative information on the thinning behavior and the rupture of the thin liquid film trapped between two bubbles. Analysis of the interferometry fringes revealed a rapid coalescence process within a few milliseconds, which is three or four orders of magnitude faster than most reported data for immobile drainage. This observation can be characterized using a lubrication model that assumes a tangentially mobile hydrodynamic boundary condition at the air-water interfaces [44–46]. We further show that a minor amount of surfactant that changes the interfacial tension in the order of 10^{-4} N/m will be enough to alter the hydrodynamic boundary condition significantly. The transition is likely associated with the balance of shear and Marangoni stresses at the interface.

4.2 Experimental system

A schematic of the Dynamic Force Apparatus [35, 79] is shown in Figure 4.1(a). The experiments were conducted in a glass vessel filled with Milli-Q purified water or surfactant solutions. By injecting ambient air from a gas-tight syringe into a capillary tube, we generated and held a bubble ($R_b=1.2$ mm) at the orifice of the capillary, while another bubble (R_s is between 400 and 850 μm) was immobilized on a hydrophobic fused silica glass surface (contact angle $\approx 100^\circ$, treated by Octadecyltrichlorosilane). Because the air-water interface is known to be easily immobilized by a tiny amount of impurities [8, 17], a thorough cleaning procedure was adopted and experiments were performed

quickly after the bubbles were generated (within 5 minutes). The glass vessel, the capillary tube, and the hydrophobic silica surface were rinsed thoroughly before each set of experiments. The liquid in the glass vessel, which was open to air, was changed hourly to avoid contamination from the ambient air. Moreover, the bottom bubble was formed by the breakage of a capillary bridge (see Appendix B for details).

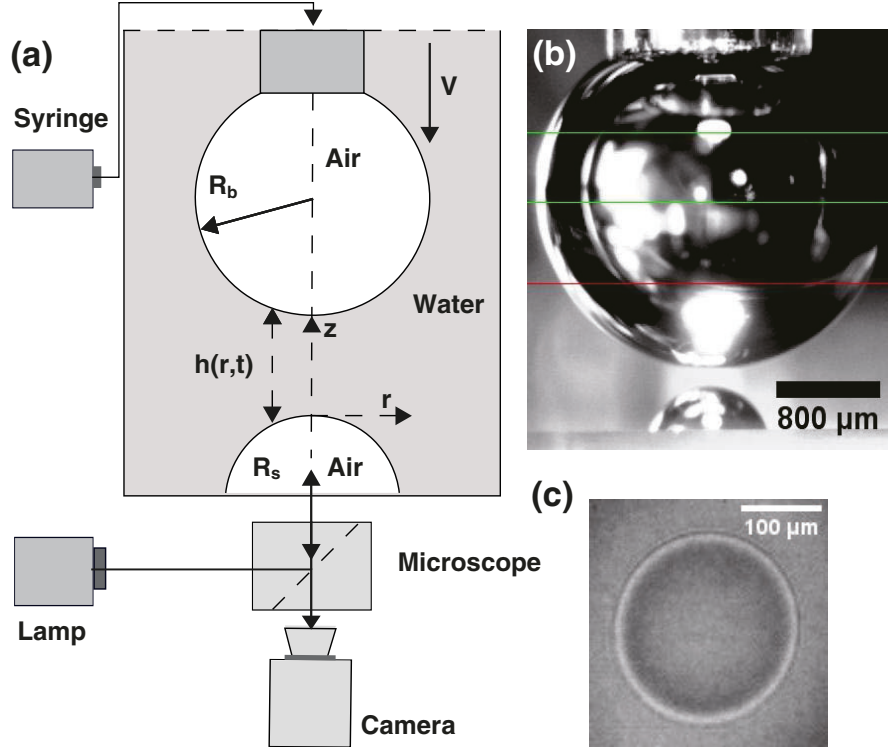


Figure 4.1: (a) Schematic of the experimental setup. A bubble of radius $R_b=1.2$ mm was held at the glass capillary orifice, whereas another bubble of radius R_s was immobilized on a hydrophobic silica surface. The capillary was driven downward by a speaker diaphragm at the velocity V to achieve collision between the bubbles. A high-speed camera connected to an inverted microscope was used to record the interference fringes. (b) Side view illustration of the bubbles, where lines are used to monitor top bubble size and position. (c) A snapshot of the interference fringes obtained between two colliding bubbles ($R_s=0.79$ mm, $V=28$ mm/s, 5 μM SDS).

The process was monitored by a side view CCD camera so that the bubbles could be carefully aligned to achieve head-to-head collision(see Figure 4.1(b)). The top bubble was pushed towards the bottom one by a speaker diaphragm at the controlled collision velocity V between 0.5 and 50 mm/s. The deformation

of the bubble due to its acceleration and movement was small or negligible at the speeds used in this study. The thinning and rupture of the thin liquid film trapped between the bubbles was directly observed by an inverted microscope (Carl Zeiss Axiovert 100) through the transparent silica glass and recorded by a high-speed camera (Photron SA4, 40000 frames/s). The lighting was achieved by a high intensity mercury lamp (X-Cite 120Q). The spatial resolution was approximately $2 \mu\text{m}/\text{pixel}$. An example of recorded interferometric fringes is shown in Figure 4.1(c).

4.3 Results and discussions

Figure 4.2(a) shows a sequence of interference fringes leading up to the rupture of the thin liquid film. The rapid evolution of interference fringes indicating fast film thinning behavior within 3 ms is shown in snapshots 1 to 4, followed by a dark area (snapshot 5) marking the coalescence of the bubbles (film ruptured). An axisymmetric drainage behavior of the liquid film can be deduced from the interference fringes. In experiments in clean systems, there was no clear evidence of the inversion of the thin liquid film or ‘dimple’ formation, which is typically present for reported experiments with immobile boundary conditions [24, 63, 79]. Furthermore, the film radius was smaller than $20 \mu\text{m}$ during the drainage process, whereas it would easily exceed $100 \mu\text{m}$ with immobilized air-water interfaces. This result suggests a very small hydrodynamic resistance during the drainage process.

The evolution of the light intensity in the central area of the film is plotted in Figure 4.2(b), from which the time evolution of the film thickness shown in Figure 4.2(c) was obtained. We define the time $t = 0$ as the point when the two non-deformable bubbles would have touched at a given applied approach speed, so the ‘coalescence time’ can be defined as the time taken from this point to film rupture. In Figure 4.2(c), the experimental result revealed that the two interfaces approached each other from 2000 nm to 100 nm at the same speed as the bubble approach velocity, followed by a gradual decrease in the thinning rate until rupture at around 30 nm , resulting in a coalescence time

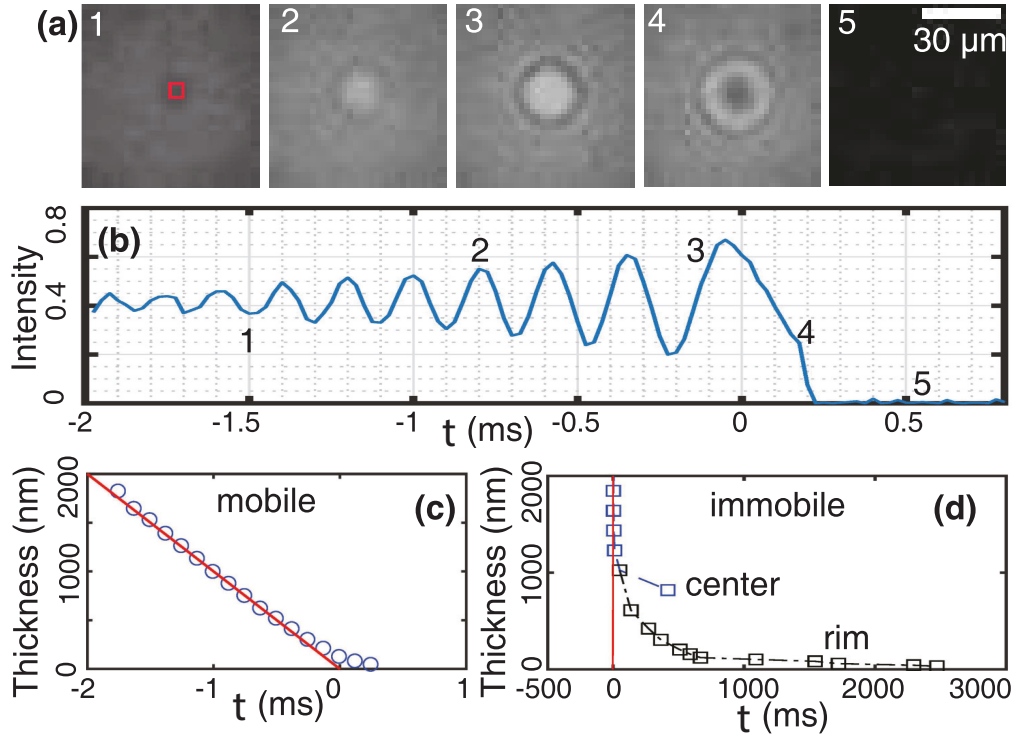


Figure 4.2: (a) Snapshots of the interference fringes in a time sequence obtained between two colliding bubbles ($R_s=0.73$ mm, $V=1$ mm/s). (b) Evolution of the light intensity at the film center marked by the red square (2×2 pixels, $\sim 4 \times 4 \mu\text{m}^2$), from which we obtained (c) time evolution of the film thickness (circles) compared with approaching undeformed bubbles (straight line). (d) Thin film drainage with immobile air water interfaces ($R_s=0.55$ mm, $V=1$ mm/s). Before collision, the bubbles were left in bulk for over 60 minutes so that the interfaces were contaminated and immobilized.

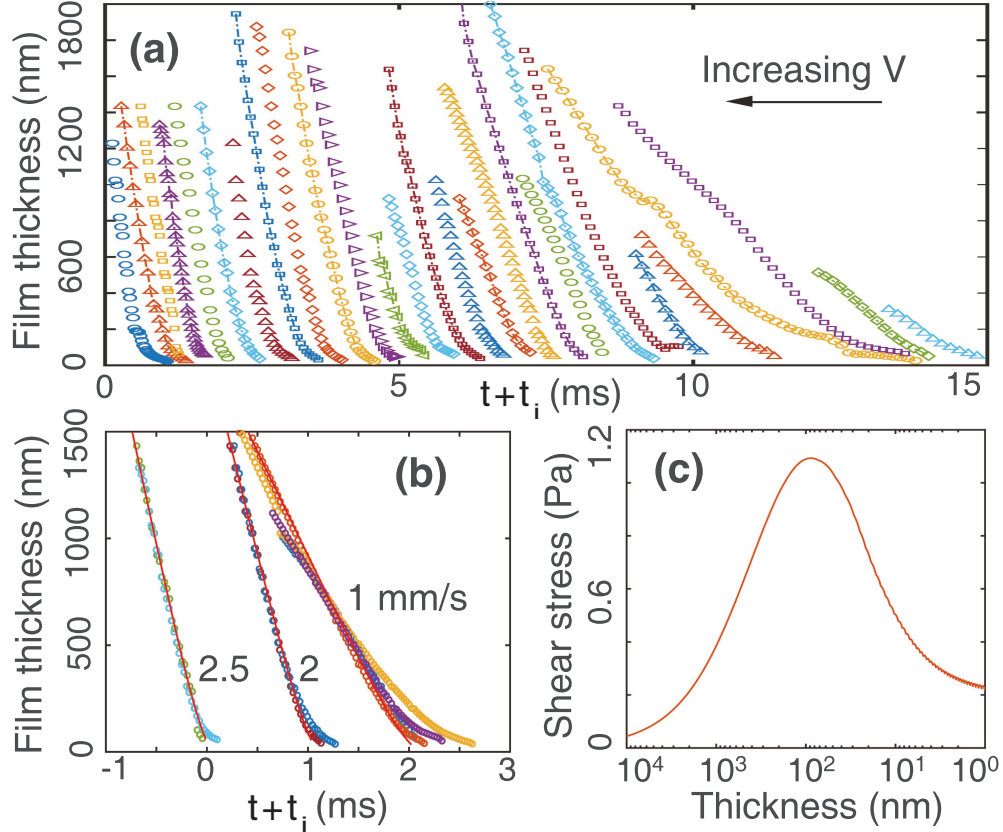


Figure 4.3: (a) Experimental film drainage at different approach velocities in the range 0.5 to 2.8 mm/s. The slope of thickness-time evolution indicates the film thinning velocity. (b) Comparison between experiments and theory [44, 45] that assumes lubrication and fully mobile boundary condition. In (a) and (b) each curve 'i' has been shifted by a time t_i for clarity. (c) In the theoretical prediction, the maximum shear stress along the interfaces evolves with center film thickness ($R_s=0.65$ mm, $V=10$ mm/s).

of 0.2 ms. This result further confirmed the low resistance at the air-water interfaces. In contrast, as shown in Figure 4.2(d), the drainage slowed down dramatically for the same process with immobile air-water interfaces, in which the coalescence was delayed by over 2000 ms with the dimple formation at the film thickness of ~ 1 μm where the film at the center became thicker than at the rim.

In Figure 4.3(a) we show the evolution of film thickness at different collision speeds ranging from 0.5 mm/s to 2.8 mm/s. The film thinning rate increases with collision speed. More specifically, the experimental film thinning rates from film thickness 2000 nm to ~ 100 nm followed the respective experimental

approach speed ($-dh/dt = V$) of the bubbles. This relationship agreed better at higher velocities than at lower ones, where the experimental thinning rate was slightly slower in some cases. Furthermore, there was a consistent slowdown of the film thinning rate when the film thickness reached ~ 100 nm.

Based on the above results two questions can be asked: (1) What is the physics behind the rapid thinning behavior with negligible resistance? (2) What is the reason for the observed slowdown of the film thinning rate at $h \sim 100$ nm? To answer these questions, we compared these experimental results with the predictions from a constant velocity model that assumes mobile fluid-fluid interfaces [44–46]. In this model, the liquid drainage is described by lubrication theory, while the flow inside the bubble is described by Stokes flow. The interfacial velocity U is determined by the continuity of the tangential shear stress across the interface ($\tau_b = \tau_f$), which arises from film liquid flow $\tau_f = \mu \partial u / \partial z|_{z=z^+}$, and the bubble air flow $\tau_b = \mu_{air} \partial u / \partial z|_{z=z^-}$ (with z^+ and z^- indicating positions at the liquid and air sides of the interface, respectively).

Comparisons between the model and the experimental results are shown in Figure 4.3(b). The rapid film thinning behavior is successfully captured in the prediction; therefore, the negligible resistance during collision can be explained by the low viscosity of the air phase [44]. Further information can be obtained from the simulation; e.g., the interfacial velocity U and shear stress τ_f at the interfaces are non-uniform with the maximum values found at the outer region of the formed thin liquid film.

Unfortunately, the model predicted faster drainage rates than the experiment at thicknesses smaller than ~ 100 nm (See Appendix B Figure C.2). The predicted film thinning speed did not slow down until a film thickness at ~ 30 nm was reached. One possible explanation for the discrepancy is the existence of a Marangoni stress $\partial \sigma / \partial r$ at the interface, which was neglected in the model but could resist τ_f in the experiment. The air-water interface is known to be easily contaminated by surface active impurities [8, 112]. Due to the continuous convection flow that sweeps the impurities out, the surface tension gradient along the interface can increase during the film thinning process.

In this scenario, the interfacial velocity U would be jointly determined by the Marangoni stress and the shear stress using the relationship $\tau_b = \partial\sigma/\partial r + \tau_f$. According to the theoretical prediction shown in Figure 4.3(c), the maximum shear stress along the surface evolves with film thickness and has a peak of around 1 Pa at a film thickness close to 100 nm. Marangoni stress ($\Delta\sigma/\Delta r$) at the same magnitude is easily achieved by a surface tension gradient ($\Delta\sigma$) of around 0.1 mN/m from the center to the outer region (assuming a characteristic radius Δr of 100 μm) of the thin liquid film. Therefore, the slowdown of the film thinning rate at small film thickness (large $\partial\sigma/\partial r$), which is more obvious at low collision speeds (small τ_f), is a consequence of the Marangoni stress. This effect can also explain experimental results with immobile boundary conditions ($|\tau_f| = |\partial\sigma/\partial r|$) [17, 24, 46], inward flow of the thin liquid film ($|\tau_f| < |\partial\sigma/\partial r|$) [38], and rapid bubble coalescence, within milliseconds, with high collision velocities and/or clean water ($|\tau_f| > |\partial\sigma/\partial r|$) [6, 85, 109].

To further understand the role of Marangoni stress on surface mobility, surfactant was added in water to change the interfacial tension in a controlled manner. The ionic surfactant sodium dodecyl sulfate (SDS, Sigma Aldrich) was used at very diluted concentrations (5, 7.5, 10, and 15 μM). Considering the dynamic adsorption process, the freshly generated bubbles were allowed to age for 10 minutes before the collision, with a measured interfacial tension change ($\Delta\sigma$) smaller than 0.2 mN/m (Krüss k12, ring method) when compared to pure water. In these diluted SDS solutions, the colliding bubbles exhibited two main outcomes: (1) Bubbles coalesced within a few milli-seconds (<5 ms), which will be referred to hereafter as ‘rapid coalescence’. (2) Bubbles took a much longer time to coalesce or did not coalesce after an experimental period of 20 seconds, which feature the formation of a dimple (Figure 4.4a) from which the liquid drained slowly until an equilibrium thin liquid film formed. This film was stabilized by the negatively charged air-water interfaces with the estimated surface potential of -80 ± 20 mV.

The impact of Marangoni stress was clearly demonstrated by the immobilization of the air water interfaces in the second case. This effect was also

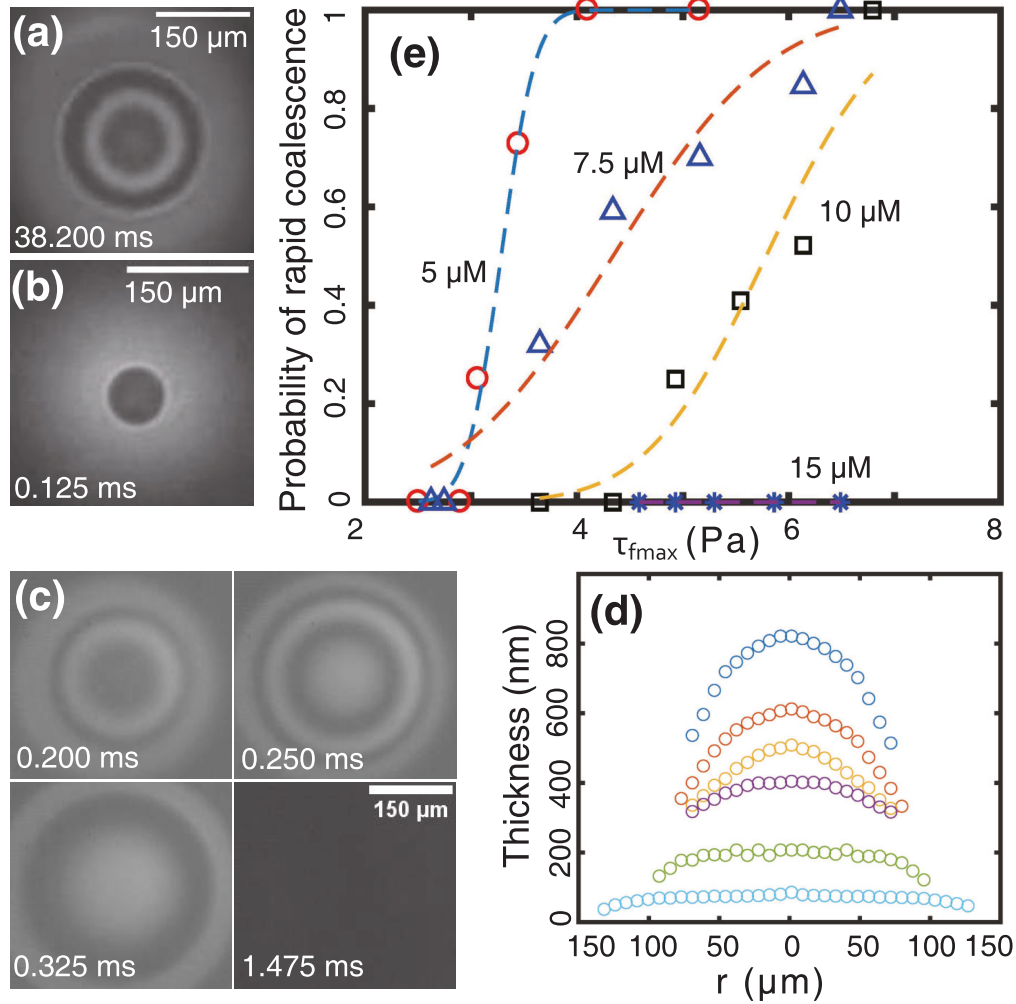


Figure 4.4: (a) Fringes showing dimple formation in $7.5 \mu\text{M}$ SDS solution, $R_s=0.83 \text{ mm}$, $V=2.8 \text{ mm/s}$ ($\tau_{fmax} \approx 3.2 \text{ Pa}$). (b) Small film width in pure water, $R_s=0.85 \text{ mm}$, $V=2.8 \text{ mm/s}$. (c) Rapid evolution of interference fringes in $10 \mu\text{M}$ SDS, $R_s=0.79 \text{ mm}$, $V=50 \text{ mm/s}$ ($\tau_{fmax} \approx 6.6 \text{ Pa}$), resulting in (d) film profiles for times from top to bottom: 0.175, 0.250, 0.300, 0.350, 0.500 and 1.325 ms. (e) The probability of rapid coalescence ($<5 \text{ ms}$) as a function of maximum shear stress ($\tau_{fmax} \sim V^{0.25}$, symbols), where '0' represent no coalescence and '1' represents rapid coalescence. Lines correspond to a cumulative Gaussian distribution fit.

manifested in cases with short coalescence time in various ways. For example, the radius of thin liquid films before rupture, which was very small for clean water ($\sim 30 \mu\text{m}$, Figure 4.4b), became much larger with the addition of SDS ($\sim 100 \mu\text{m}$, Figures. 4.4a, 4.4c), indicating an increase in the resistance at the interfaces. More significantly, the snapshots for $10 \mu\text{M}$ SDS shown in Figure 4.4(c) describe the formation of a dimple during the early stage, which diminished rapidly and ruptured in milli-seconds. By analyzing the complete fringes [79, 109], film profiles are presented in Figure 4.4(d). The formation of the dimple clearly indicates that the interfaces were initially immobile, however, the subsequent rapid film thinning in milli-seconds suggests that the boundary condition changed to mobile during the film thinning process. This transition can be explained by the lesser impact of the Marangoni stress when compared to the increasing shear stress in the dynamic process.

The approach velocities ranging from 1 to 50 mm/s would change the maximum shear stress at the immobile interface following the relationship $\tau_{fmax} \approx 0.5Ca^{0.25}\sigma/R$ ($Ca = \mu V/\sigma$, with μ the water viscosity) [46]. The probability of rapid coalescence as a function of the maximum shear stress (assume $R_s=0.65 \text{ mm}$) is presented in Figure 4.4(e) for SDS concentrations of 5, 7.5, 10 and 15 μM . The probabilities were generated after at least 20 repeated experiments for each case. Consistent non-coalescence was observed at low shear stress ($|\partial\sigma/\partial r| \geq |\tau_f|$, low approach velocity), and consistent quick coalescence at large shear stress ($|\partial\sigma/\partial r| < |\tau_f|$, large approach velocity). For values in between, the experimental outcomes appeared to follow a probabilistic behavior and were reasonably fitted by the cumulative Gaussian distribution function. As the SDS concentration was increased, faster approach velocities were required for rapid coalescence; moreover, rapid coalescence was not observed for 15 μM , illustrating that the Marangoni stress would be dominant over the shear stress at this concentration or larger. In the great majority of scenarios, the film would either be ruptured in milliseconds or be stabilized, a result that agrees well with the prediction of Chesters [14] that the surfactant would either completely immobilize the surface or be driven away by the film flow.

4.4 Conclusion

In summary, we investigated the thin film drainage between two quickly colliding bubbles using high speed interferometry. The experimental results in the clean water system provided rapid film thinning rates almost identical to the collision speeds, indicating negligible resistance and mobile hydrodynamic boundary condition at the air-water interface. Results in the presence of a small amount of surfactant, which changed the interfacial tension in the order of 10^{-4} N/m, highlighted the role of the Marangoni stress caused by the uneven distribution of surface active materials in the hydrodynamic boundary condition. The Marangoni stress can balance the shear stress, hindering the mobility of the air-water interface and even resulting in a transition from a mobile to an immobile boundary condition. The competition between stresses might evolve continually over the thinning process for the mobile interface, but once balance has been achieved, the surface becomes immobile. Our systematic investigation provides explanations for previous experimental data that had either fast or slow bubble coalescence.

Chapter 5

Coalescence or Bounce? How Surfactant Adsorption in Milliseconds Affects Bubble Collision

Abstract

The coalescence between two colliding bubbles in ultraclean water can be 3 or 4 orders of magnitude faster than the coalescence in contaminated solutions. This surprising result is explained by the mobile or immobile boundary conditions at the air-water interface. In this work, we employ rising bubbles to study bubble collisions in aqueous solutions of up to 2 mM surfactant concentrations. The experimental results clearly show that freshly generated bubbles can coalesce within milliseconds if they collide right after generation. However, once the bubbles stayed in bulk for tens of milliseconds, the coalescence is heavily hindered. Based on these results, we conclude that the clean air-water interface, rather than clean water, is required to achieve the mobile boundary condition that allows quick coalescence. These findings provide fundamental understanding for further improvements in bubble generation that will benefit industrial processes such as mineral flotation, oil extraction, and waste water treatment.

5.1 Introduction

Two air bubbles colliding in ultraclean water can coalesce within milliseconds [113], much faster than the time required in contaminated or surfactant systems. Understanding this behavior is essential for a better-controlled bubble generation technique, which is the core component in mineral flotation [1], oil extraction [3], and water purification [4]. In such industries, the typical residence time of particles or oil drops in bulk can be over 10 minutes. However, their attachment to the air bubbles is highly influenced by the short bubble generation process that lasts tens of milliseconds [114, 115]. During bubble generation, the newly formed air bubbles collide with each other and with the target particles/drops, thereby influencing the bubble size distribution and bubble-particle attachment, two key factors for successful flotation [2, 79, 115, 116]. The rapid bubble coalescence within milliseconds provides an opportunity for rational manipulation of the bubble coalescence or bounce in the short bubble generation period, hence improving the flotation recovery and selectivity.

To achieve rapid bubble coalescence, the air-water interface needs to be mobile [113], that means, negligible tangential resistance at the interface. The tangentially mobile interface enhances the fluid flow inside the thin liquid film trapped between the bubbles. [14, 17, 44, 113] The lack of resistance at the interface contributes to a film thinning rate that is roughly equal to the bubble collision speed until its rupture at around 50 nm; hence, the bubbles can coalesce within milliseconds. [113] However, contaminations that change the air-water interfacial tension in the order 10^{-4} N/m can be sufficient to inhibit the air-water interface mobility and render the interface immobile (i.e zero tangential velocity). [14, 17, 113] For decades, most of the experimental data was modeled using the tangentially immobile boundary condition. [8, 16, 17, 24] In the limited experiments where the mobile air-water interface was achieved, the experimental setup had to be carefully cleaned and water purity had to be maintained. [18, 89, 113, 117] In industry, however, surface active components are unavoidable or even purposely added to reduce the

interfacial tension [1, 71, 116], resulting in solutions that are much ‘dirtier’ than the clean water used in laboratory experiments. The question remains unanswered about whether the rapid bubble coalescence with mobile air-water interface can be achieved in the contaminated or surfactant solutions.

In this letter, we report bubble collision experiments in surfactant solutions using the rising bubble technique. Side view observations with a high speed camera (5000 frames/s) clearly show the dynamic collision in milliseconds between two air bubbles in aqueous solutions. By observing the bounce or coalescence between the bubbles and compare with theoretical predictions, we found that the freshly generated air-water interface could be mobile even in surfactant solutions, and that enabled bubble coalescence within a few milliseconds. The mobility can be easily inhibited once the bubble was left in bulk for tens of milliseconds, which is fast but in the same order of magnitude as the bubble generation process. The results show that a clean air-water interface is required to achieve the mobile boundary condition, and therefore, controlled bubble coalescence or bounce can be achieved.

5.2 Experimental method

Schematic of the rising bubble experimental setup is shown in Figure 5.1a. In a square glass vessel ($170 \times 40 \times 60 \text{ mm}^3$) that avoids optical distortion, we placed a homemade sharp end capillary tube at the bottom through a capillary holder. Air bubbles (radii $300\text{-}600 \mu\text{m}$) were generated by pumping air through the capillary using a syringe pump at the volumetric flow rates from 0.5 to 4 mL/min. The flat air-water surface was adjusted to be ~ 5 mm above the capillary orifice. This distance allows the bubble to travel at its terminal velocity before hitting the top flat surface. It also enables the detailed sequential observation of the complete dynamic process (bubble formation, rise, collision, bounce and coalescence) using a high-speed camera (Photron SA4) at the resolution $\sim 15 \mu\text{m}/\text{pixel}$.

Before the experiment, the glass vessel was carefully washed in 1 M NaOH solution, and rinsed thoroughly with milli-Q water. The capillary holder and

respective tubing were ultrasonic washed for 20 minutes and rinsed thoroughly. Milli-Q purified water was used to prepare the surfactant solutions with Sodium Dodecyl Sulfate (SDS, Sigma Aldrich, 98.5%) or methyl isobutyl carbinol (MIBC, Fisher Scientific, 99%) at concentrations ranging from 0.01 to 2 mM.

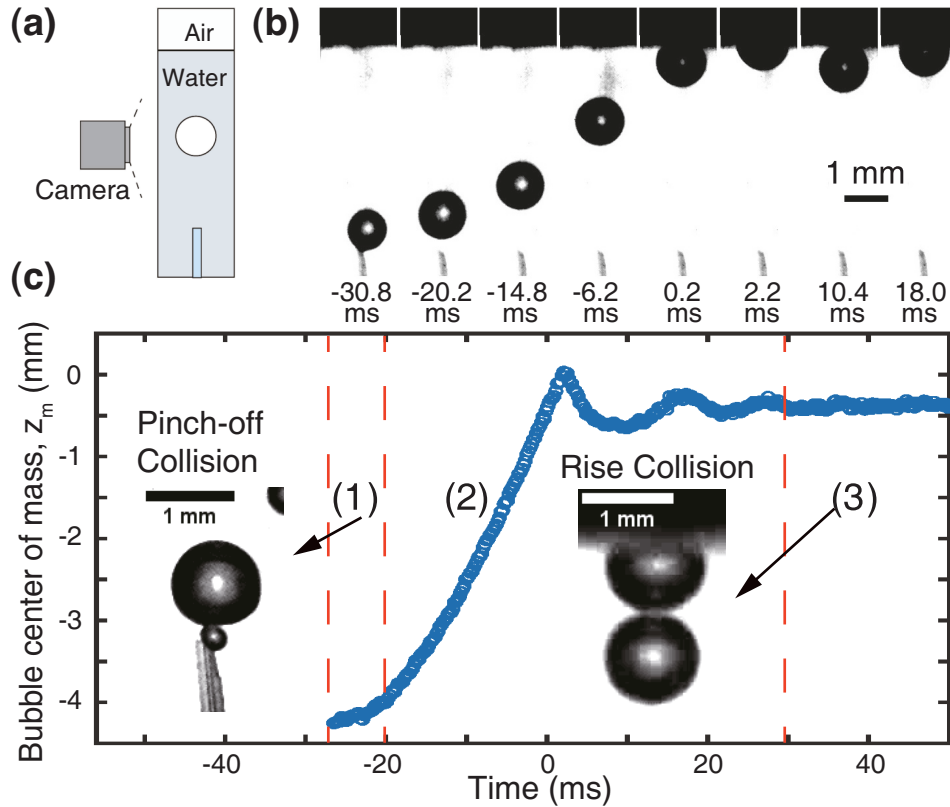


Figure 5.1: (a) Schematic of the rising bubble experimental setup. (b) Snapshots of a rising bubble and its collision with the flat air-water interface in a 0.03 mM SDS solution. Images were pretreated by ImageJ. (c) The extracted bubble trajectory, from which the rise collision and pinch-off collision were designed (see insets) with different aging time (~ 50 ms and ~ 10 ms, respectively). Time $t=0$ is defined as the time the bubble would have ‘touched’ the flat interface if there was no deformation; the flat surface is defined as the position $z=0$. The position of the bubble was extracted from the images by Matlab.

Snapshots of the rising bubble are shown in Figure 5.1b, from which the rising trajectory shown in Figure 5.1c was extracted. Initially, the just released bubble oscillated in bulk and rose slowly (≤ 5 cm/s) for around 10 ms (stage

1). Afterward, the bubble rapidly accelerated to its terminal velocity of ~ 20 cm/s, taking 20 ms for it to hit the flat air-water surface. Upon collision, the bubble bounced back slightly a few times during which the kinetic energy was dissipated [15, 17, 37]. After that, the bubble rested below the surface, and moved laterally at a slow speed (stage 3). In the experiment, the bubbles were released continually from the capillary orifice and the bubbling frequency was adjusted by changing the aeration rate.

Based on the bubble rising trajectory, we adjusted the aeration rate to change the aging time and obtained two distinct aging time scales: ~ 50 ms, named ‘rise collision’ and ~ 10 ms, named ‘pinch-off collision’. The rise collision was achieved with small aeration rates (0.5-1.5 mL/min) so that bubbles were generated and released every 20-60 ms. In this way, one bubble that was resting on the flat surface was hit by the rising one. The pinch-off collision was achieved with higher aeration rates (2-4 mL/min). In this scenario, one bubble that was just pinched off was hit by the growing bubble at the orifice. The bubble expansion rate (~ 5 -40 cm/s) was much faster than the rising velocity (~ 5 cm/s) of the first bubble that was still in the slow rising phase. In both cases, the aging time was counted based on the bubble that stayed longer in bulk. Discussion regarding the aging time is provided in appendix C.

5.3 Results and discussions

By varying the experimental conditions, bubble collisions exhibited two outcomes: (1) the bubbles bounced away from each other after interacting for a few milliseconds, (2) they merged into a bigger one almost immediately (≤ 0.4 ms) upon collision. Examples for these outcomes are provided in Figure 5.2. For instance, the snapshots in Figure 5.2a show the collision and bounce between two bubbles of ~ 0.52 mm radii. Initially, one bubble was staying below the flat air-water interface, while the other was rising in bulk at its terminal velocity of 18.3 cm/s. Upon collision, the bottom bubble slowed down dramatically with observable deformation, pushing the top bubble upward to indent

into the flat air-water surface. After staying in contact for a few milliseconds, the bubbles bounced away from each other and recovered their spherical shape. Because the bubbles were not exactly vertically aligned, the second collision was not head-on. As a comparison, the scenario in which the colliding bubbles coalesced is provided in Figure 5.2b. Similarly, the bottom bubble rose at its terminal velocity (19.2 cm/s), similar to the previous one though the bubble radius was smaller (~ 0.40 mm). However, the bubbles coalesced almost immediately (≤ 0.4 ms) upon collision. Neither of the bubbles deformed nor changed their trajectory before coalescence, suggesting negligible resistance during their collision. Similar results with bounce or coalescence were also observed with the pinch-off bubble collision (see Appendix C).

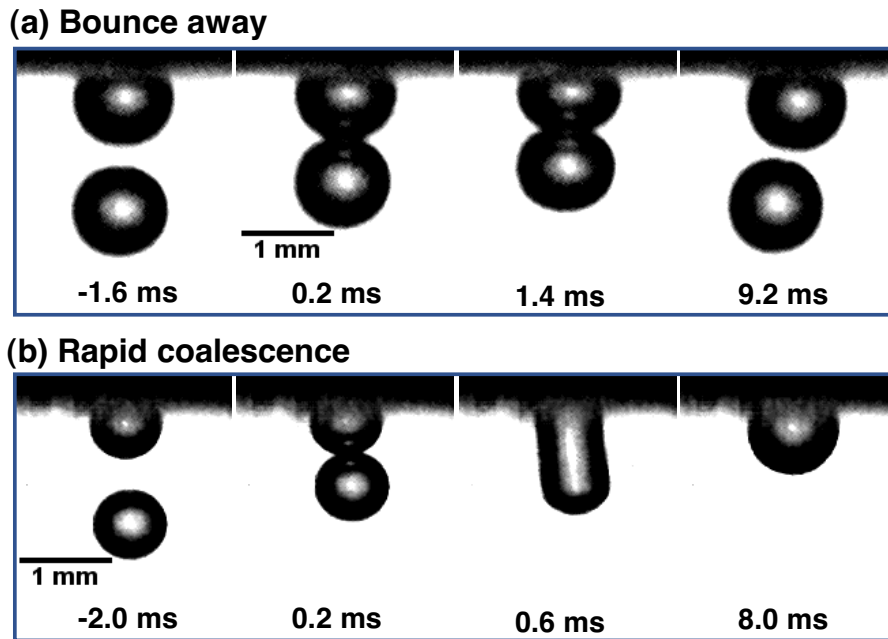


Figure 5.2: (a) Snapshots of the bubble bounce in the 0.05 mM SDS solution; bubble radii are ~ 0.52 mm, collision velocity is 18.3 cm/s. (b) Snapshots for bubble coalescence in milli-Q water; bubble radii are ~ 0.40 mm, collision velocity is 19.2 cm/s. The time $t=0$ is defined as the first image that the two bubbles ‘touched’ from side view observation, which means that the actual distance is below $15 \mu\text{m}$ (1 pixel).

The probability of coalescence varies with surfactant concentrations and aging time for pinch-off or rise collisions, as shown in Figure 5.3, in which each probability data point was obtained from more than 100 collisions. The

probability value ‘1’ corresponds to the consistent bubble coalescence, while ‘0’ corresponds to the consistent bubble bounce. The surfactant concentration was varied by 2 orders of magnitude from 0.01 to 2 mM. Results obtained for 0.01 mM SDS showed consistent coalescence, similar to experiments using pure water. For both SDS and MIBC solutions, increasing the surfactant concentration significantly reduced the probability of coalescence, with the relationship reasonably fitted by an inverse accumulated normal distribution (dashed lines). Meanwhile, the aging time showed a dramatic impact on the coalescence statistics. With the longer aging time (~ 50 ms), bubble coalescence was not observed once the surfactant concentration exceeded 0.05 mM. By comparison, rapid coalescence was still observed in 1 mM MIBC solution for the shorter aging time (~ 10 ms). Based on the statistical results of Figure 5.3, the outcome of bubble collisions is determined jointly by the bulk surfactant concentration and aging time. This can be qualitatively explained by the dynamic adsorption of surfactant from the bulk to the air-water interface [65, 71, 118, 119].

There are many factors influencing bubble collision results, such as bubble size [6, 17, 79], collision velocity [8, 9, 120] and surface forces [16, 24, 63]. However, regarding the coalescence or bounce that happens within a few milliseconds, the most rational explanation is the difference in the air-water interface mobility [6, 113]. The boundary condition is significantly influenced by the dynamic surfactant adsorption onto the air-water interface. An immobile surface should be achieved with enough surfactant adsorbed at the air-water interface, whereas a mobile surface can be achieved with relatively clean air-water interface. In experiment, the bouncing case represents the result with an immobile boundary condition, whereas the coalescence case represents the mobile air-water interface on both bubbles. As mentioned before, the difference in surface mobility is determined by the competition between the shear stress and the Marangoni stress. The latter is significantly influenced by the . To support this hypothesis, we modeled the bubble collision process using theories that assume immobile and mobile boundary conditions at the air-water interface. Three boundary conditions were considered in the theory:

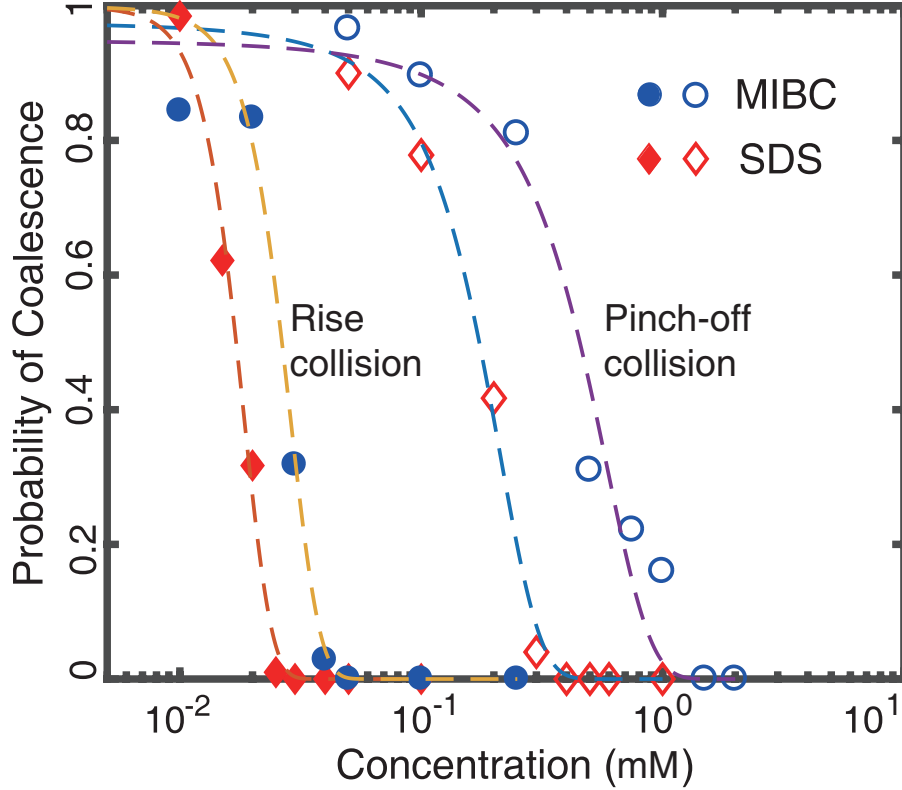


Figure 5.3: Probability of coalescence as a function of surfactant concentration for pinch-off and rise collisions.

(A) both surfaces are clean and mobile (mobile-mobile); (B) one surface is mobile while the other is immobile (immobile-mobile); (C) both surfaces are immobile (immobile-immobile). The position $z=0$ is defined as the undeformed fluid surfaces, as shown in the insets (1) and (2) of Figure 5.4a. The time $t=0$ is defined as the expected collision time if the bubble and flat surfaces are non-deformable. Comparisons between the experimental results and the model are shown in Figure 5.4. For the mobile-mobile case, experimental data obtained between two colliding bubbles is used. For the other cases, experimental data obtained between a rising air bubble and a flat surface is chosen to fulfill the axisymmetric assumption in the model. The flat surface can be assumed as a large-contaminated bubble with immobile boundary condition, [15, 17, 69]. Details of the equations, the boundary conditions, and the numerical technique are presented in appendix c.

The experimental rising velocities were used in the theoretical calculations.

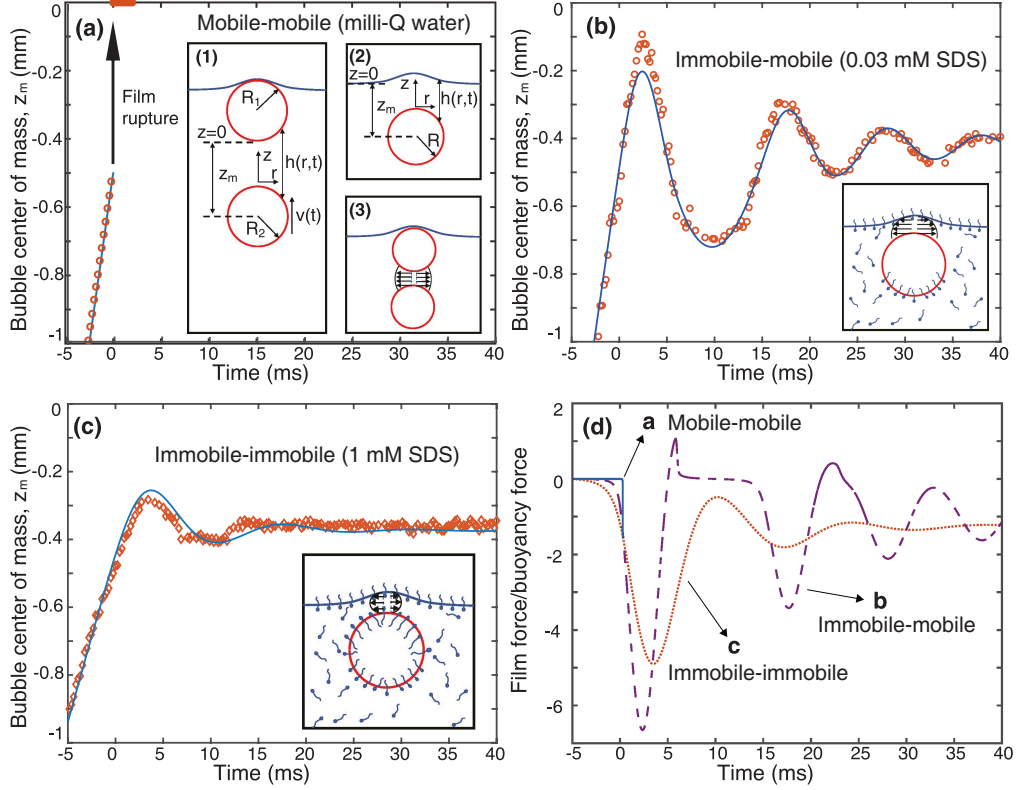


Figure 5.4: Comparison between theory and experiment for the bubble position under different conditions. The insets show the coordinate definitions and the schematic representations of the boundary conditions. (a) Two bubbles coalesce with mobile surfaces in Milli-Q water ($R_1=R_2=0.38$ mm, collision velocity is 17.8 cm/s). (b) Bubble-flat surface collision in 0.03 mM SDS solution ($R=0.48$ mm, collision velocity is 21.2 cm/s, immobile-mobile boundary condition). (c) Bubble-flat surface collision in 1 mM SDS solution ($R=0.45$ mm, collision velocity is 11.4 cm/s, immobile-immobile boundary condition). (d) Comparison of film forces for the cases a, b and c.

In milli-Q purified water (Figure 5.4a) and 1 mM SDS solution (Figure 5.4c), the rising velocities agree well with the theoretical prediction using the mobile and immobile boundary conditions, respectively. [43] For the concentration of 0.03 mM, the bubble rising velocity was 21.2 cm/s (Figure 5.4b), which lies in between the expected terminal velocities for fully mobile (~ 25 cm/s) and immobile (~ 10 mm/s) air-water interface, suggesting partial adsorption of surfactant on the bubble. [43, 69, 121]

The collision process exhibited significant differences. In milli-Q water, the colliding air bubbles coalesced without any bounce (see Figure 5.4a), which

agreed with the prediction using the mobile-mobile boundary condition (Figure 5.4a inset 3). As a comparison, bubble bouncing was observed in the other two cases. Bounces presented in Figure 5.4b agree with the prediction using the immobile-mobile boundary condition, with the flat surface being the immobile side. This can be justified because the flat surface has been reported to be easily immobilized by contaminants from the ambient air [15, 17, 24], while surfactant was used in this experiment. Therefore, the top surface of the rising bubble should be clean and mobile, while the bottom surface was contaminated to reduce the bubble rising velocity. The uneven distribution of surfactant at the interface is caused by the shear flow in the rising stage. [121] In 1 mM SDS solution, the rise and bounce of the bubble agree well with the prediction using immobile-immobile boundary condition.

The bubble bouncing behavior is determined by the film force arises from the fluid flow inside the thin liquid film [15, 17] (see Appendix C for the force balance equation). The evolution of the film forces normalized by the buoyancy force during collisions are provided in Figure 5.4d. The forces start to build up when the distance is less than $\sim 10 \mu\text{m}$ ($5 \text{ ms} \times 20 \text{ cm/s}$), after which the bubble surfaces deformed to form the thin film. The initial film formation for case (c) is slightly earlier than for case (b), caused by the difference in the surface mobility. For both cases, the kinetic energy was dissipated during the bounces, and showed a negligible effect on the coalescence of the rising bubble and the flat surface. The coalescence was mostly determined by the film thinning process at the resting stage, when the film force was equal to the buoyancy force. In contrast, the film for the mobile-mobile case only formed when the surfaces were almost touching and it ruptured in an extremely short time. Consequently, this small film force was barely enough to deform the bubbles and agrees with the observation in Figure 5.2b. With the mobile boundary condition, the velocity at the interface is determined by the viscosity ratio in the bulk and in the bubble. [44, 113] Considering the viscosity ratio between water and air (~ 50), it is not surprising to find a large surface velocity, rapid film thinning, and negligible resistance.

5.4 Conclusion

In conclusion, we employed the rising bubble technique to explore bubble collision and coalescence in surfactant solutions. The freshly generated bubbles were allowed to age for two time scales (~ 50 ms and ~ 10 ms) and the dynamic bubble rise and collision were captured by a high speed camera. In the collision process that lasted a few milliseconds, the bubbles could either bounce away from each other or merge into a bigger one. These outcomes agreed well with the theoretical predictions using either immobile or mobile boundary conditions at the air-water interface. Statistical results showed that the boundary conditions changed with the bulk surfactant concentration and the aging time, which was explained by the dynamic adsorption of surfactants. Our work illustrates that clean air-water interfaces give rise to the mobile boundary condition, rather than just ultraclean water. This knowledge bridges the gap between the fundamental understanding on surface mobility with engineering applications.

Chapter 6

Conclusions and Future work

6.1 Conclusions

The major contributions of this thesis to science and engineering are listed as follows.

An experimental method combining the bubble pair concept and thin film interferometry was developed based on the home-made Dynamic Force Apparatus, by which the interaction force and the spatiotemporal evolution of the liquid film between two colliding bubbles were obtained simultaneously. The thin film dynamics were studied in various experimental conditions. Parameters like bubble size, collision speed, bulk surfactant concentration can be easily adjusted. This technique can also be used to study drop coalescence and bubble-drop attachment.

A systematic study of the interaction and coalescence between a millimeter size bubble and surface micro-bubbles with different radius (30-700 μm) were explored. The measured interaction force agreed well with the prediction of the Stokes-Reynolds-Young-Laplace equation using the tangentially immobile boundary condition at the air-water interface. The coalescence times increase with increasing micro-bubble size, which can be explained by the reduction of Laplace pressure. To be more specific, a significant increase of coalescence time from ~ 100 ms to 1000 ms was observed when the surface bubble radius increased from ~ 50 μm to 300 μm . The theoretical prediction works as an upper bound for the experimental coalescence times. The variation of the coalescence time in the experiments was attributed to a loss of symmetry

during the thin liquid film drainage, which allows the trapped liquid to drain out faster than the theoretical prediction. The observed experimental rupture thicknesses of 25 ± 15 nm, agreed with the theoretical prediction considering van der Waals interaction as the controlling factor for film rupture.

After that, the rapid film thinning rate between two colliding bubbles that was equal to the collision speed ($-dh/dt = V$) was captured using high-speed interferometry. The film thinning with negligible resistance was explained by a model that assuming mobile boundary condition at the air-water interfaces. The air-water interface mobility was dramatically altered by a minute amount of surfactant that changed the interfacial tension by about 10^{-4} N/m. The balance of the shear stress and Marangoni stress is shown to determine surface mobility. The results provide solid evidence of film drainage with mobile boundary condition at the air-water interfaces.

In the following work, bubble coalescence in surfactant solutions was investigated. Experiments were conducted in a simple bubble rising technique in which the freshly generated bubbles can collide after staying in bulk for a very short period (~ 10 ms or ~ 50 ms). According to the bounce or coalescence results, it is shown that the mobile air-water interface is achievable even in surfactant solutions similar to those used in the industrial processes. The freshly generated bubbles can be mobile and may switch to immobile after staying in bulk for tens of milliseconds. The surface mobility is jointly determined by the bubble residence time in bulk and the bulk surfactant concentration, corresponding to the dynamic adsorption of the surfactant onto the air-water interface. These findings suggest that the clean air-water interface, rather than the clean water, is required to achieve the mobile boundary condition at the air-water interface. This work bridges the fundamental understanding of surface mobility to real applications like mineral flotation, oil extraction, and water purification.

6.2 Future Research

The developed experimental method and the findings in this thesis enable some further research. Some possibilities are listed below

- The experimental setup can be adopted to study the thin film drainage between two drops or between an air bubble and an oil drop. The effect of bubble/drop size, surfactant, collision velocity, and de-emulsifier on thin liquid film drainage between the deformable drop/bubble can be investigated.
- The impact of salt on bubble coalescence has not been well explained. In-depth understanding will possibly be achieved using this setup.
- The results in chapter 4 and chapter 5 prove the existence of the fully mobile interface in bubble coalescence. This property can be utilized to optimize the design of the bubble generator, which will benefit many industrial applications.
- In surfactant solutions, the transition from mobile to immobile boundary condition happens within tens of milliseconds. Retarding the transition process by applying an external field, such as ultrasonic, can be helpful for industrial applications.

References

1. Yoon, R.-H. Microbubble flotation. *Minerals Engineering* **6**, 619–630 (1993).
2. Yoon, R. & Luttrell, G. The effect of bubble size on fine particle flotation. *Mineral Processing and Extractive Metallurgy Review* **5**, 101–122 (1989).
3. Masliyeh, J., Zhou, Z. J., Xu, Z., Czarnecki, J. & Hamza, H. Understanding water-based bitumen extraction from Athabasca oil sands. *The Canadian Journal of Chemical Engineering* **82**, 628–654 (2004).
4. Rubio, J., Souza, M. & Smith, R. Overview of flotation as a wastewater treatment technique. *Minerals Engineering* **15**, 139–155 (2002).
5. Anthony, C. R. *et al.* Scaling laws and dynamics of bubble coalescence. *Phys. Rev. Fluids*. **2**, 083601. ISSN: 2469-990X (2017).
6. Horn, R. G., Del Castillo, L. A. & Ohnishi, S. Coalescence map for bubbles in surfactant-free aqueous electrolyte solutions. *Advances in Colloid and Interface Science* **168**, 85–92. ISSN: 00018686 (2011).
7. Chan, D. Y. C., Klaseboer, E. & Manica, R. Film drainage and coalescence between deformable drops and bubbles. *Soft Matter* **7**, 2235–2264. ISSN: 1744-683X (2011).
8. Langevin, D. Bubble coalescence in pure liquids and in surfactant solutions. *Current Opinion in Colloid and Interface Science* **20**, 92–97. ISSN: 18790399 (2015).
9. Orvalho, S., Ruzicka, M. C., Olivieri, G. & Marzocchella, A. Bubble coalescence: Effect of bubble approach velocity and liquid viscosity. *Chemical Engineering Science* **134**, 205–216. ISSN: 00092509 (2015).
10. Katsir, Y. & Marmur, A. Rate of bubble coalescence following dynamic approach: Collectivity-induced specificity of ionic effect. *Langmuir* **30**, 13823–13830. ISSN: 15205827 (2014).
11. Firouzi, M. & Nguyen, A. V. Effects of monovalent anions and cations on drainage and lifetime of foam films at different interface approach speeds. *Advanced Powder Technology* **25**, 1212–1219. ISSN: 15685527 (2014).

12. Yaminsky, V. V., Ohnishi, S., Vogler, E. A. & Horn, R. G. Stability of aqueous films between bubbles. Part 1. the effect of speed on bubble coalescence in purified water and simple electrolyte solutions. *Langmuir* **26**, 8061–8074. ISSN: 07437463 (2010).
13. Henry, C. L., Dalton, C. N., Scruton, L. & Craig, V. S. J. Ion-specific coalescence of bubbles in mixed electrolyte solutions. *Journal of Physical Chemistry C* **111**, 1015–1023. ISSN: 19327447 (2007).
14. Chesters, A. K. & Bazhlekov, I. B. Effect of insoluble surfactants on drainage and rupture of a film between drops interacting under a constant force. *Journal of Colloid and Interface Science* **230**, 229–243 (2000).
15. Manica, R., Klaseboer, E. & Chan, D. Y. The impact and bounce of air bubbles at a flat fluid interface. *Soft Matter* **12**, 3271–3282 (2016).
16. Vakarelski, I. U. *et al.* Dynamic interactions between microbubbles in water. *Proc. Natl. Acad. Sci. U. S. A.* **107**, 11177–11182 (2010).
17. Vakarelski, I. U. *et al.* Coalescence dynamics of mobile and immobile fluid interfaces. *Langmuir* **34**. PMID: 29328665, 2096–2108 (2018).
18. Del Castillo, L. A., Ohnishi, S. & Horn, R. G. Inhibition of bubble coalescence: Effects of salt concentration and speed of approach. *Journal of Colloid and Interface Science* **356**, 316–324 (2011).
19. Katsir, Y. & Marmur, A. Rate of bubble coalescence following dynamic approach: Collectivity-induced specificity of ionic effect. *Langmuir* **30**, 13823–13830. ISSN: 15205827 (2014).
20. Karakashev, S. I. & Nguyen, A. V. Effect of sodium dodecyl sulphate and dodecanol mixtures on foam film drainage: Examining influence of surface rheology and intermolecular forces. *Colloids and Surfaces A: Physicochemical and Engineering Aspects* **293**, 229–240. ISSN: 09277757 (2007).
21. Karakashev, S. I. & Manev, E. D. Hydrodynamics of thin liquid films: Retrospective and perspectives. *Advances in Colloid and Interface Science* **222**, 398–412. ISSN: 00018686 (2015).
22. Karakashev, S. I. Hydrodynamics of foams. **58**, 1–40. ISSN: 07234864 (2017).
23. Krasowska, M. & Malysa, K. Wetting films in attachment of the colliding bubble. *Advances in Colloid and Interface Science* **134**, 138–150 (2007).
24. Chan, D. Y. C., Klaseboer, E. & Manica, R. Theory of non-equilibrium force measurements involving deformable drops and bubbles. *Advances in Colloid and Interface Science* **165**, 70–90. ISSN: 00018686 (2011).
25. Frankel, S. P. & Myseis, K. J. On the “dimpling” during the approach of two interfaces¹. *The Journal of Physical Chemistry* **66**, 190–191 (1962).

26. Hartland, S. & Robinson, J. D. A model for an axisymmetric dimpled draining film. *Journal of Colloid and Interface Science* **60**, 72–81 (1977).
27. Jain, R. K. & Ivanov, I. B. Thinning and rupture of ring-shaped films. *Journal of the Chemical Society, Faraday Transactions 2: Molecular and Chemical Physics* **76**, 250–266 (1980).
28. Dagastine, R. R. *et al.* Dynamic forces between two deformable oil droplets in water. *Science* **313**, 210–213. ISSN: 0036-8075 (2006).
29. Manica, R., Connor, J. N., Carnie, S. L., Horn, R. G. & Chan, D. Y. C. Dynamics of Interactions Involving Deformable Drops: Hydrodynamic Dimpling under Attractive and Repulsive Electrical Double Layer Interactions. *Langmuir* **23**. PMID: 17209614, 626–637 (2007).
30. Tabor, R. F., Manica, R., Chan, D. Y. C., Grieser, F. & Dagastine, R. R. Repulsive van der Waals Forces in Soft Matter: Why Bubbles Do Not Stick to Walls. *Phys. Rev. Lett.* **106**, 064501 (6 Feb. 2011).
31. Verwey, E. Theory of the stability of lyophobic colloids. *The Journal of Physical Chemistry* **51**, 631–636 (1947).
32. Tabor, R. F., Chan, D. Y. C., Grieser, F. & Dagastine, R. R. Anomalous Stability of Carbon Dioxide in pH-Controlled Bubble Coalescence. *Angewandte Chemie* **123**, 3516–3518 (2011).
33. Tabor, R. F., Wu, C., Grieser, F., Dagastine, R. R. & Chan, D. Y. C. Measurement of the Hydrophobic Force in a Soft Matter System. *The Journal of Physical Chemistry Letters* **4**. PMID: 27045729, 3872–3877 (2013).
34. Wang, L. & Yoon, R.-H. Effects of surface forces and film elasticity on foam stability. *International Journal of Mineral Processing* **85**, 101–110. ISSN: 0301-7516 (2008).
35. Zhang, X. *et al.* Simultaneous measurement of dynamic force and spatial thin film thickness between deformable and solid surfaces by integrated thin liquid film force apparatus. *Soft Matter* **12**, 9105–9114 (2016).
36. Feng, L., Manica, R., Grundy, J. S. & Liu, Q. Unraveling Interaction Mechanisms between Molybdenite and a Dodecane Oil Droplet Using Atomic Force Microscopy. *Langmuir* (2019).
37. Hendrix, M. H., Manica, R., Klaseboer, E., Chan, D. Y. & Ohl, C. D. Spatiotemporal evolution of thin liquid films during impact of water bubbles on glass on a micrometer to nanometer scale. *Physical Review Letters* **108**, 1–4. ISSN: 00319007 (2012).
38. Zhang, X., Manica, R., Tchoukov, P., Liu, Q. & Xu, Z. Effect of Approach Velocity on Thin Liquid Film Drainage between an Air Bubble and a Flat Solid Surface. *Journal of Physical Chemistry C* **121**, 5573–5584 (2017).

39. Schäffel, D., Koynov, K., Vollmer, D., Butt, H.-J. & Schönecker, C. Local flow field and slip length of superhydrophobic surfaces. *Physical Review Letters* **116**, 134501 (2016).
40. Langevin, D. Rheology of adsorbed surfactant monolayers at fluid surfaces. *Annual Review of Fluid Mechanics* **46**, 47–65 (2014).
41. Sonin, A. A., Bonfillon, A. & Langevin, D. Role of surface elasticity in the drainage of soap films. *Phys. Rev. Lett.* **71**, 2342–2345 (14 Oct. 1993).
42. Danov, K. D., Valkovska, D. S. & Ivanov, I. B. Effect of surfactants on the Film Drainage. *Journal of Colloid and Interface Science* **211**, 291–303. ISSN: 1095-7103 (1999).
43. Manica, R., Klaseboer, E. & Chan, D. Y. The hydrodynamics of bubble rise and impact with solid surfaces. *Advances in Colloid and Interface Science* **235**, 214–232 (2016).
44. Davis, R. H., Schonberg, J. A. & Rallison, J. M. The lubrication force between two viscous drops. *Phys. Fluids A: Fluid Dynamics* **1**, 77–81 (1989).
45. Abid, S. & Chesters, A. K. The drainage and rupture of partially-mobile films between colliding drops at constant approach velocity. *International Journal of Multiphase Flow* **20**, 613–629. ISSN: 03019322 (1994).
46. Klaseboer, E., Chevaillier, J. P., Gourdon, C. & Masbernat, O. Film drainage between colliding drops at constant approach velocity: experiments and modeling. *Journal of Colloid and Interface Science* **229**, 274–285 (2000).
47. Azgomi, F., Gomez, C. & Finch, J. Correspondence of gas holdup and bubble size in presence of different frothers. *International Journal of Mineral Processing* **83**, 1–11 (2007).
48. Chen, F., Gomez, C. & Finch, J. bubble size measurement in flotation machines. *Minerals Engineering* **14**, 427–432 (2001).
49. Nasset, J. E. *Modeling the Sauter Mean Bubble Diameter in Mechanical Forced-air Flotation Machines* (McGill University Montreal, Canada, 2011).
50. Girgin, E., Do, S., Gomez, C. & Finch, J. Bubble size as a function of impeller speed in a self-aeration laboratory flotation cell. *Minerals Engineering* **19**, 201–203. ISSN: 0892-6875 (2006).
51. Craig, V. S., Ninham, B. W. & Pashley, R. M. The effect of electrolytes on bubble coalescence in water. *The Journal of Physical Chemistry* **97**, 10192–10197 (1993).
52. Dobby, G., Yianatos, J. & Finch, J. Estimation of bubble diameter in flotation columns from drift flux analysis. *Canadian Metallurgical Quarterly* **27**, 85–90 (1988).

53. Banisi, S. & Finch, J. reconciliation of bubble size estimation methods using drift flux analysis. *Minerals Engineering* **7**, 1555–1559 (1994).
54. Gorain, B., Franzidis, J.-P. & Manlapig, E. Studies on impeller type, impeller speed and air flow rate in an industrial scale flotation cell—Part 1: Effect on bubble size distribution. *Minerals Engineering* **8**, 615–635 (1995).
55. Laakkonen, M., Honkanen, M., Saarenrinne, P. & Aittamaa, J. Local bubble size distributions, gas–liquid interfacial areas and gas holdups in a stirred vessel with particle image velocimetry. *Chemical Engineering Journal* **109**, 37–47 (2005).
56. Kirkpatrick, R. & Lockett, M. The influence of approach velocity on bubble coalescence. *Chemical Engineering Science* **29**, 2363–2373 (1974).
57. Ivanov, I. *Thin liquid films* (CRC Press, 1988).
58. Manev, E. D. & Nguyen, A. V. Critical thickness of microscopic thin liquid films. *Advances in Colloid and Interface Science* **114**, 133–146 (2005).
59. Derjaguin, B. & Kussakov, M. An experimental investigation of poly-molecular solvate (adsorbed) films as applied to the development of a mathematical theory of the stability of colloids. *Acta Physicochimica URSS* **10**, 26–45. ISSN: 00796816 (1939).
60. Karakashev, S. I. *et al.* Comparative validation of the analytical models for the Marangoni effect on foam film drainage. *Colloids and Surfaces A: Physicochemical and Engineering Aspects* **365**, 122–136 (2010).
61. Scheludko, A. Thin liquid films. *Advances in Colloid and Interface Science* **450**, 391–464. ISSN: 00018686 (1967).
62. Karakashev, S. I., Nguyen, A. V. & Manev, E. D. A novel technique for improving interferometric determination of emulsion film thickness by digital filtration. *Journal of Colloid and Interface Science* **306**, 449–453 (2007).
63. Yaminsky, V. V., Ohnishi, S., Vogler, E. A. & Horn, R. G. Stability of aqueous films between bubbles. Part 2. Effects of trace impurities and evaporation. *Langmuir* **26**, 8075–8080. ISSN: 07437463 (2010).
64. Oolman, T. O. & Blanch, H. W. Bubble coalescence in stagnant liquids. *Chemical Engineering Communications* **43**, 237–261 (1986).
65. Yang, Y. M. & Maa, J. R. Bubble coalescence in dilute surfactant solutions. *Journal of Colloid and Interface Science* **98**, 120–125 (1984).
66. Bournival, G., Ata, S., Karakashev, S. & Jameson, G. An investigation of bubble coalescence and post-rupture oscillation in non-ionic surfactant solutions using high-speed cinematography. *Journal of Colloid and Interface Science* **414**, 50–58 (2014).

67. Zhang, F. & Thoroddsen, S. Satellite generation during bubble coalescence. *Physics of Fluids* **20**, 022104 (2008).
68. Feng, J., Li, X., Bao, Y., Cai, Z. & Gao, Z. Coalescence and conjunction of two in-line bubbles at low Reynolds numbers. *Chemical Engineering Science* **141**, 261–270 (2016).
69. Kosior, D. & Zawala, J. Initial degree of detaching bubble adsorption coverage and the kinetics of dynamic adsorption layer formation. *Physical Chemistry Chemical Physics* **20**, 2403–2412 (2018).
70. Zawala, J., Dorbolo, S., Terwagne, D., Vandewalle, N. & Malysa, K. Bouncing bubble on a liquid/gas interface resting or vibrating. *Soft Matter* **7**, 6719–6726. ISSN: 1744-683X (2011).
71. Pawliszak, P. *et al.* Interfacial characterisation for flotation: 2. Air-water interface. *Current Opinion in Colloid and Interface Science* (2018).
72. Wang, L., Sharp, D., Masliyah, J. & Xu, Z. Measurement of interactions between solid particles, liquid droplets, and/or gas bubbles in a liquid using an integrated thin film drainage apparatus. *Langmuir* **29**, 3594–3603. ISSN: 07437463 (2013).
73. Browne, C. *et al.* Bubble coalescence during acoustic cavitation in aqueous electrolyte solutions. *Langmuir* **27**, 12025–12032. ISSN: 07437463 (2011).
74. Doublié, L. The drainage and rupture of a non-foaming liquid film formed upon bubble impact with a free surface. *International Journal of Multiphase Flow* **17**, 783–803 (1991).
75. Morokuma, T., Ohara, T. & Utaka, Y. Combination of laser interferometric and laser extinction methods for precise thickness measurement of liquid film between coalescing twin air bubbles. *International Journal of Heat and Mass Transfer* **127**, 154–160. ISSN: 0017-9310 (2018).
76. Cain, F. & Lee, J. A technique for studying the drainage and rupture of unstable liquid films formed between two captive bubbles: measurements on KCl solutions. *Journal of Colloid and Interface Science* **106**, 70–85 (1985).
77. Bhamla, M. S., Chai, C., Álvarez-Valenzuela, M. A., Tajuelo, J. & Fuller, G. G. Interfacial mechanisms for stability of surfactant-laden films. *PLOS ONE* **12**, e0175753 (2017).
78. Cosijnse, J. *Experimental and numerical research of coalescence of two approaching drops in liquid-liquid dispersions* PhD thesis (Masters thesis, Eindhoven University of Technology, 1994).
79. Liu, B. *et al.* Dynamic Interaction between a Millimeter-Sized Bubble and Surface Microbubbles in Water. *Langmuir* **34**, 11667–11675 (2018).

80. Gao, Y. & Pan, L. Measurement of instability of thin liquid films by synchronized tri-wavelength reflection interferometry microscope. *Langmuir* **34**, 14215–14225 (2018).
81. Takahashi, M. ζ potential of microbubbles in aqueous solutions: electrical properties of the gaswater interface. *The Journal of Physical Chemistry B* **109**, 21858–21864. ISSN: 1520-6106 (2005).
82. Graciaa, A., Morel, G., Saulner, P., Lachaise, J. & Schechter, R. The ζ -potential of gas bubbles. *Journal of Colloid and Interface Science* **172**, 131–136 (1995).
83. Katsir, Y. & Marmur, A. Rate of bubble coalescence following quasi-static approach: Screening and neutralization of the electric double layer. *Scientific Reports* **4**, 4266 (2014).
84. Pushkarova, R. A. & Horn, R. G. Bubble- solid interactions in water and electrolyte solutions. *Langmuir* **24**, 8726–8734 (2008).
85. Del Castillo, L. A., Ohnishi, S., Carnie, S. L. & Horn, R. G. Variation of local surface properties of an air bubble in water caused by its interaction with another surface. *Langmuir* **32**, 7671–7682. ISSN: 15205827 (2016).
86. Chesters, A. K. & Hofman, G. in *Mechanics and Physics of Bubbles in Liquids* 353–361 (Springer, 1982).
87. Shi, C. *et al.* Measuring forces and spatiotemporal evolution of thin water films between an air bubble and solid surfaces of different hydrophobicity. *ACS Nano* **9**, 95–104. ISSN: 1936086X (2015).
88. Klaseboer, E., Manica, R. & Chan, D. Y. Universal behavior of the initial stage of drop impact. *Physical Review Letters* **113**, 1–5. ISSN: 10797114 (2014).
89. Parkinson, L. & Ralston, J. The interaction between a very small rising bubble and a hydrophilic titania surface. *Journal of Physical Chemistry C* **114**, 2273–2281. ISSN: 19327447 (2010).
90. Wang, L. & Qu, X. Impact of interface approach velocity on bubble coalescence. *Minerals Engineering* **26**, 50–56. ISSN: 08926875 (2012).
91. Manica, R. *et al.* Hydrodynamic forces involving deformable interfaces at nanometer separations. *Physics of Fluids* **20**, 032101. ISSN: 10706631 (2008).
92. Langevin, D. Rheology of adsorbed surfactant monolayers at fluid surfaces. *Annual Review of Fluids Mechanics* **46**, 47–65. ISSN: 0066-4189 (2014).
93. Fan, M., Tao, D., Honaker, R. & Luo, Z. Nanobubble generation and its application in froth flotation (part I): nanobubble generation and its effects on properties of microbubble and millimeter scale bubble solutions. *Mining Science and Technology (China)* **20**, 1–19 (2010).

94. Azevedo, A., Etchepare, R., Calgaroto, S. & Rubio, J. Aqueous dispersions of nanobubbles: Generation, properties and features. *Minerals Engineering* **94**, 29–37. ISSN: 08926875 (2016).
95. Mishchuk, N., Ralston, J. & Fornasiero, D. Influence of very small bubbles on particle/bubble heterocoagulation. *Journal of Colloid and Interface Science* **301**, 168–175. ISSN: 00219797 (2006).
96. Firouzi, M., Howes, T. & Nguyen, A. V. A quantitative review of the transition salt concentration for inhibiting bubble coalescence. *Advances in Colloid and Interface Science* **222**, 305–318. ISSN: 00018686 (2015).
97. Del Castillo, L. A., Ohnishi, S. & Horn, R. G. Inhibition of bubble coalescence: Effects of salt concentration and speed of approach. *Journal of Colloid and Interface Science* **356**, 316–324. ISSN: 00219797 (2011).
98. Malysa, K., Krasowska, M. & Krzan, M. Influence of surface active substances on bubble motion and collision with various interfaces. *Advances in Colloid and Interface Science* **114-115**, 205–225. ISSN: 00018686 (2005).
99. Zawala, J. & Malysa, K. Influence of the impact velocity and size of the film formed on bubble coalescence time at water surface. *Langmuir* **27**, 2250–2257. ISSN: 07437463 (2011).
100. Manica, R., Klaseboer, E. & Chan, D. Y. The impact and bounce of air bubbles at a flat fluid interface. *Soft Matter* **12**, 3271–3282 (2016).
101. Katsir, Y. & Marmur, A. Rate of bubble coalescence following quasi-static approach: Screening and neutralization of the electric double layer. *Scientific Reports* **4**, 1–7. ISSN: 20452322 (2014).
102. Shi, C. *et al.* Interaction between air bubbles and superhydrophobic surfaces in aqueous solutions. *Langmuir* **31**, 7317–7327. ISSN: 15205827 (2015).
103. Morokuma, T. & Utaka, Y. Variation of the liquid film thickness distribution between contacting twin air bubbles during the coalescence process in water and ethanol pools. *International Journal of Heat and Mass Transfer* **98**, 96–107 (2016).
104. Xie, L., Shi, C., Cui, X. & Zeng, H. Surface forces and interaction mechanisms of emulsion drops and gas bubbles in complex fluids. *Langmuir* **33**. PMID: 28178417, 3911–3925 (2017).
105. Parkinson, L. & Ralston, J. Dynamic aspects of small bubble and hydrophilic solid encounters. *Advances in Colloid and Interface Science* **168**, 198–209. ISSN: 00018686 (2011).
106. Khristov, K., Taylor, S., Czarnecki, J. & Masliyah, J. Thin liquid film technique—application to water–oil–water bitumen emulsion films. *Colloids and Surfaces A: Physicochemical and Engineering Aspects* **174**, 183–196 (2000).

107. Radoev, B. P., Scheludko, A. D. & Manev, E. D. Critical thickness of thin liquid films: Theory and experiment. *Journal of Colloid and Interface Science* **95**, 254–265. ISSN: 00219797 (1983).
108. Verschoof, R. A., Van Der Veen, R. C., Sun, C. & Lohse, D. Bubble Drag Reduction Requires Large Bubbles. *Physical Review Letters* **117**, 1–4. ISSN: 10797114 (2016).
109. Yaminsky, V. V., Ohnishi, S., Vogler, E. A. & Horn, R. G. Stability of aqueous films between bubbles. Part 1. The effect of speed on bubble coalescence in purified water and simple electrolyte solutions. *Langmuir* **26**, 8061–8074 (2010).
110. Tsai, P. *et al.* Quantifying effective slip length over micropatterned hydrophobic surfaces. *Physics of Fluids* **21**, 112002 (2009).
111. Vakarelski, I. U. *et al.* Self-determined shapes and velocities of giant near-zero drag gas cavities. *Science Advances* **3**, e1701558 (2017).
112. Maali, A. *et al.* Viscoelastic drag forces and crossover from no-slip to slip boundary conditions for flow near air-water interfaces. *Physical Review Letters* **118**, 084501 (2017).
113. Liu, B. *et al.* Coalescence of Bubbles with Mobile Interfaces in Water. *Physical Review Letters* **122**, 194501 (19 May 2019).
114. Jameson, G. J. New directions in flotation machine design. *Minerals Engineering* **23**. Froth Flotation, 835–841. ISSN: 0892-6875 (2010).
115. Zhou, Z., Xu, Z., Finch, J., Masliyah, J. & Chow, R. On the role of cavitation in particle collection in flotation—A critical review. II. *Minerals Engineering* **22**, 419–433 (2009).
116. Kracht, W. & Finch, J. Using sound to study bubble coalescence. *Journal of Colloid and Interface Science* **332**, 237–245 (2009).
117. Henry, C. L., Parkinson, L., Ralston, J. R. & Craig, V. S. A mobile gas-water interface in electrolyte solutions. *Journal of Physical Chemistry C* **112**, 15094–15097 (2008).
118. Chang, C.-H. & Franses, E. I. Adsorption dynamics of surfactants at the air/water interface: a critical review of mathematical models, data, and mechanisms. *Colloids and Surfaces A: Physicochemical and Engineering Aspects* **100**, 1–45 (1995).
119. Eastoe, J. & Dalton, J. Dynamic surface tension and adsorption mechanisms of surfactants at the air–water interface. *Advances in Colloid and Interface Science* **85**, 103–144 (2000).
120. Duineveld, P. in *In Fascination of Fluid Dynamics* 409–439 (Springer, 1998).
121. Sadhal, S. & Johnson, R. E. Stokes flow past bubbles and drops partially coated with thin films. Part 1. Stagnant cap of surfactant film—exact solution. *Journal of Fluid Mechanics* **126**, 237–250 (1983).

122. Butt, H.-J., Kappl, M., *et al.* *Surface and interfacial forces* (Wiley Online Library, 2010).
123. Parsegian, V. A. & Gingell, D. On the electrostatic interaction across a salt solution between two bodies bearing unequal charges. *Biophysical Journal* **12**, 1192–1204 (1972).
124. Moore, D. The velocity of rise of distorted gas bubbles in a liquid of small viscosity. *Journal of Fluid Mechanics* **23**, 749–766 (1965).
125. Schiller, L. & Naumann, A. *A. Zeit Ver Deut Ing*, 77:318 (1933).

Appendix A

Experimental and data analysis

A.1 Bottom bubble generation

In Chapter 3, the surface microbubbles were generated by an ultra-sharp pipette. In chapter 4, the possible contamination from the pipette became a concern, because of our strict requirement on the air-water surface cleanness. Therefore, a method for minimizing external contaminations was adopted to generate bubbles on the solid substrate (see Figure A.1). An air bubble was generated and held at the capillary orifice. Then the bubble was driven toward the solid surface to form an air bridge between the tube and the substrate. The capillary tube was further moved downward until its orifice was around 1 mm above the substrate. By sucking air out slowly using the gas-tight syringe, the air capillary bridge was broken, hereafter a small bubble was left on the solid substrate. This procedure allowed for quick bubble-bubble interactions.

A.2 Alignment of the bubbles in water

Detailed steps for the alignment of the top bubble and the surface microbubble are shown in Figure A.2. Careful alignment of the bubbles was monitored by the inverted microscope. As shown in Figure A.2A, at the beginning we set the focus of the microscope at the top surface of the quartz glass. Then the microscope focus was moved upward until the observation of a bright round area indicating the bottom center of the top millimeter size bubble (see Figure A.2B). The location of the bright circle area was marked using a red

rectangular box. Afterward the focus was moved downward slightly until a similar round bright area, marked by a grey box in Figure A.2C, due to the light re-lected from the top of the surface microbubble was observed. By carefully adjustment of the surface microbubble location until the center of the bright circle areas (marked by the red and grey boxes) overlap with each other, the alignment of the bubbles was achieved. Then the focus was moved upward slightly (shown in Figure A.2D) for the observation of the interference fringes during the collision of the bubbles.

A.3 Film thickness determination

The thin film thickness is obtained by interferometric measurements. The mercury lamp, with three specific characteristic wavelengths (436 nm, 546 nm and 579 nm), enabled the extraction of light intensity $I(t)$ from three channels (blue, green and red) of the high-speed images captured (as shown in Figs. A.3a and b). The observed interference fringes were used to obtain the absolute film thickness $h(t)$ by fitting the theoretical relation (Eq.A.1) of wavelength (λ) dependent thickness as a function of fringe order [79, 80, 89], which is defined when isolating $h(t)$ in the Eq.A.1 The fringe order was determined by counting back from the last fringe before film rupture, the latter was confirmed to be order 1 from the comparison of results obtained from different channels. I_{max} and I_{min} are maximum and minimum intensities in each range (peaks and valleys, see Figure 4.2b) and n is the refractive index of water. As shown in Figs.A.3a and b, the film thickness calculated from the three-channel interference agreed well with each other, while their deviation from the polynomial fitted curve was less than 30 nm. Film thickness results reconstructed from the green channel images, which provided the clearest fringes, are reported in chapter 4.

The conversion from intensity to thin film thickness was performed using the following equation [89]

$$\frac{I(t) - I_{min}}{I_{max} - I_{min}} = \sin^2 \left(\frac{2\pi n h(t)}{\lambda} \right) \quad (\text{A.1})$$

The film ruptured at the thickness ~ 30 nm, therefore I_{min} for this fringe order ($h=0$ nm) cannot be obtained experimentally. The background light after rupture was assumed to be the specific value for I_{min} , which would contribute to a maximum error of around 30 nm [79].

Experiments in pure water were performed for velocities from 0.5 mm/s up to 50 mm/s, but for large velocities the current camera frame rate was insufficient to clearly capture the interference fringes. Therefore, only intensities from velocities no larger than 2.8 mm/s were analyzed by this method. In surfactant solutions, higher velocities are required to achieve higher shear stress. The results are reported based on the collision outcome (rapid coalescence or not) in chapter 4, rather than the film thinning rate.

A.4 Reconstruction of the thin film profile (symmetric and asymmetric)

With immobile air-water interfaces(chapter 3), The early stage of film drainage is symmetric and can be compared with the SRYL model. In Figure A.4A we show the comparison between theory and experiment for the first few profiles just before the loss of symmetry, showing quite reasonable agreement. In Figure A.4B, a non-symmetric 3D thin film profile reconstructed from the last snapshot of Figure A.4 is shown. The figure describes the liquid film profile before rupture. As is shown in the figure, the thin film is neither symmetric nor flat. But we can easily find that the thickest part of the thin liquid film is roughly at the center, while the thinnest part can be found somewhere around the rim.

A.5 Estimation of the uncertainty in the critical rupture thickness

In chapter 3, the critical rupture thickness for different bubble sizes was calculated based on the independently measured light intensities using the equation one shown below. Where $I_{rupture}$ is the light intensity at rupture point, I_{max}

and I_{min} are the maximum and minimum light intensities shown in Figure 3.6, respectively. λ is the wavelength of light, n_1 and n_2 are the refractive indices of air and water.

$$h(r, t) = \frac{\lambda}{2\pi n_2} \left(\arcsin \sqrt{\frac{\Delta}{1 + 4(1 - \Delta) \frac{R_{12}}{(1 - R_{12})^2}}} \right) \quad (\text{A.2})$$

$$R_{12} = \frac{(n_1 - n_2)^2}{(n_1 + n_2)^2} \quad (\text{A.3})$$

$$\Delta = \frac{I_{rupture} - I_{min}}{I_{max} - I_{min}} \quad (\text{A.4})$$

The impact of experimental errors on rupture thickness is considered in this work. The sources of the errors would include (1) identifying the location of rupture and the light intensity of rupture; (2) identifying the max and minimum light intensities; (3) average of the light intensities from 9 pixels; (4) systematic errors (i.e., background light) that can be up and down. Overall, any uncertainties in $I_{rupture}$, I_{max} and I_{min} would contribute to the uncertainty in the film rupture thickness. In this study, we provide a very conservative estimate of errors. The error range shown in Figure 3.6 is estimated based on methods mentioned below: (1) in addition to I_{max} and I_{min} measured from the light intensity profile of the selected 9 pixels, two extreme values I_{max2} and I_{min2} in one experimental run by analyzing the overall thin film area were also obtained. These extreme values would provide a reasonable top bound for I_{max} and a bottom bound for I_{min} . (2) The accuracy of $\pm 10\%$, a typical value for sensitivity analysis, is assumed for the rupture light intensity ($I_{rupture}$).

$$\Delta_{up} = \frac{1.1I_{rupture} - I_{min2}}{I_{max} - I_{min2}} \quad (\text{A.5})$$

$$\Delta_{bottom} = \frac{0.9I_{rupture} - I_{min}}{I_{max2} - I_{min}} \quad (\text{A.6})$$

The consideration of the two sources of uncertainties lead to the Δ_{up} and Δ_{bottom} values shown in equation A.5 and A.6 respectively for the calculation of upper and lower bounds of the critical rupture thickness in Figure 3.6.

A.6 Matlab code for film center thickness

In this section, we provide the Matlab code for the extraction of film center thickness using the interferometry method. The code is divided into three files: 1. Video Read; 2. Light intensity extraction; 3. Thickness analysis. To extract the dimple profile, the code need to be slightly modified.

A.6.1 Read the video

```
clc; clear;
    %% read the video, the video is pretreated
v=VideoReader('green_mobile1.avi');
frames=v.NumberOfFrames;
m=v.Height;
n=v.Width;
I_total=0;
    %% extract the data from the video
tic
cc=zeros(m,n,frames); % build a matrix to store the data
    for k=1:frames % a loop to extract the data
frame=read(v,k);
frame=frame(:,:,1);
frame=im2double(frame);
cc(:,:,k)=frame;
end
toc
pp=cc; % use a new matrix to store the data for further processing
```

A.6.2 Extract light intensity

```
%%%%%%%%%%
%%% Extract the light intensity data from the video
%%%%%%%%%%
close all
```

```

clc
pp1=pp; % pp is the matrix containing the video data
%% Extract the data from the film center
aa=17;bb=16; % film center
image_show=25; % show a suitable frame in the later stage
i=2; % get data from 3*3 data points
qq_00=pp1(aa:aa+i,bb:bb+i,:); % data matrix
qq_0=sum(sum(qq_00)); % sum the data from 9 points
qq_1(:)=qq_0(1,1,:); % store the sum data in the data vector
qq_2=qq_1/((i+1)^2); % average
%% plot the data, and shown the image
plot((1:frames)/40,qq_2) % recorded at 40,000 fps
grid on; grid minor;
xlabel('Time (ms)')
ylabel('Light Intensity')
figure;
imshow(pp(:, :, image_show)); % show the frame
rectangle('position',[bb,aa,i,i])

```

A.6.3 Film thickness extraction

```

%%%%%%%%%%
%Calculate the film thickness from center light intensity
%%%%%%%%%%
lambda=546; % wave length of green light
qq_3=smooth(qq_2); % smooth the light intensity to remove noise
loc_0=1:frames; % frames number vector
stp=99; % the rupture frame
%% find the peaks and valleys
[pks_1, locs_1] = findpeaks(qq_3(1 : stp)); % find peaks
[vls_2, locs_2] = findpeaks(-qq_3(1 : stp)); % find valleys

vls_2=-vls_2; % the value of valleys

```

```

plot(loc_0,qq_3,loc_0(locs_1),pks_1,'or',loc_0(locs_2),vls_2,'ob'); % plot for check
%% clarify I_max and I_min for calculation
I_max=locs_1';
I_min=locs_2';
I_all=[I_max I_min];% include all the elements in a big vector and sort
I_all=sort(I_all);
I_number=size(I_all,2); % find the column
rim=find(I_all==I_all(end)); %
h_start=1;
% values for calculation
n_1=1; % refractive index of air
n_0=1.333; % refractive index of water
rrr = (n_0 - n_1)/((n_0 + n_1)^2);% only water and air
rrr_minus = (1 - rrr)^2;
%begin calculation of film thickness
for i=2:rim
tt=abs((i-rim)/2);
aa=floor(tt);
bb=mod(abs((i-rim)),2);
i_vector=[qq_3(I_all(i-1)) qq_3(I_all(i))];
for kkk=I_all(i-1):I_all(i) % point 1 to point 2
delta(kkk)=(qq_3(kkk)-min(i_vector))/(max(i_vector)-min(i_vector));
a_sin(kkk)=asin((1+rrr)*sqrt(delta(kkk)/(rrr_minus+4*rrr*delta(kkk))));
h(kkk)=lambda/(2*pi*n_0)*((h_start+aa)*pi-(1-2*bb)*a_sin(kkk));
end
end
%% from the peak to rupture
for kkk=I_all(rim):stp
max_1=qq_3(I_all(end));
%min_1=qq_3(I_all(end-1)+20);
min_1=qq_3(end); % light intensity after rupture is assumed to be the mini-
mum light intensity at the film thickness 0 nm

```

```

delta(kkk)=(qq_3(kkk)-min_1)/(max_1-min_1);
a_sin(kkk)=asin((1+rrr)*sqrt(delta(kkk)/(rrr_minus+4*rrr*delta(kkk))));
h(kkk)=lambda/(2*pi*n_0)*((1-2*bb)*a_sin(kkk));
end
    hp=[];
hp=h(L_all(1):stp);
hp=abs(hp);
figure
plot((1:95)/40,abs(hp),'o')% time should be further corrected
axis([-2 3 0 900])
xlabel('Time (ms)')
ylabel('Film thickness (nm)')

```

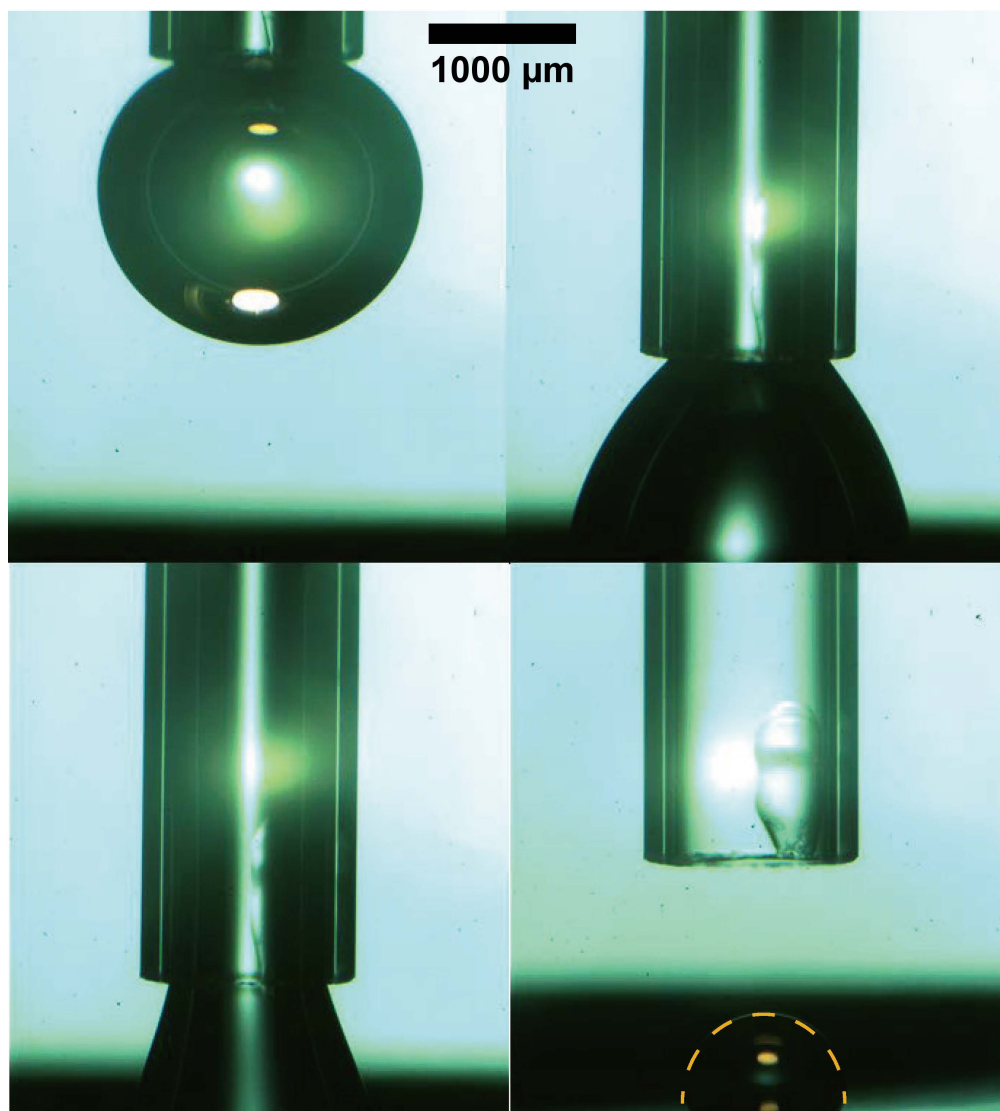


Figure A.1: (a) A bubble was generated from the capillary tube. (b) The bubble was driven to the surface to form a capillary bridge (c) Air was sucked out using the syringe. (d) After the air bridge broke, a bubble remained at the solid surface.

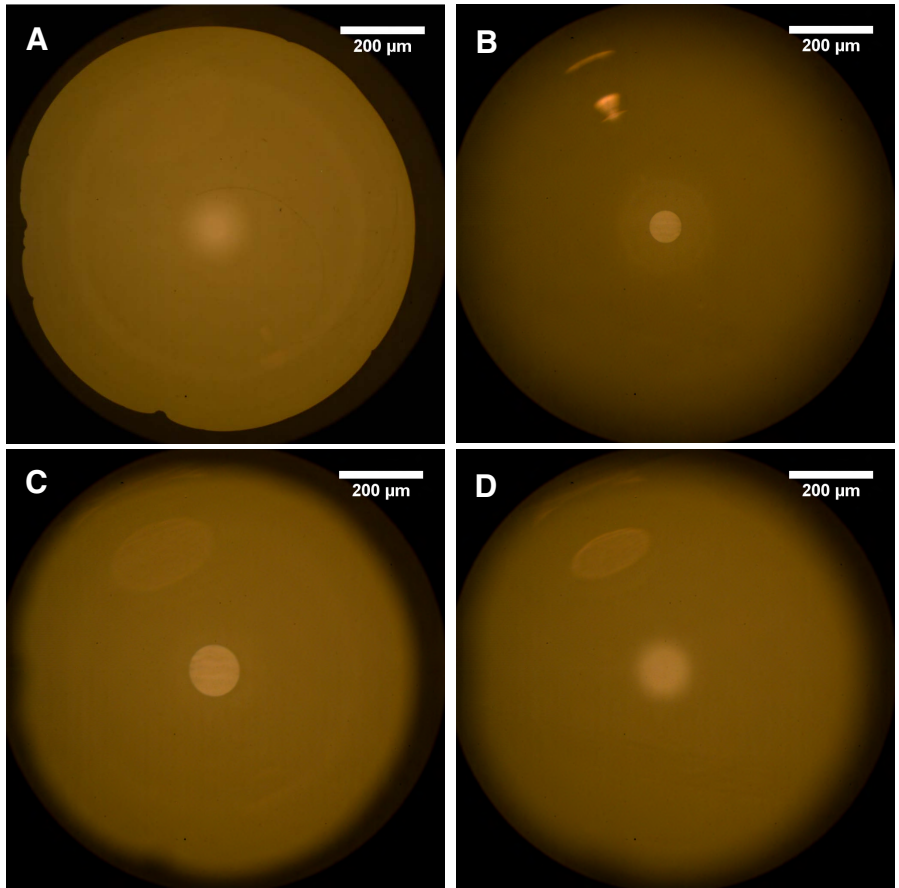


Figure A.2: Alignment of the bubbles assisted by the inverted microscope (A) Focus at the quartz glass top surface, the surface bubble is observed; (B) Focus at the bottom of the top bubble, the center area is marked using the red box; (C) Focus at the top of the surface microbubble, the center area is marked using a grey box. The overlap of the red and the grey boxes indicate a proper alignment of two bubbles; (D) The focus is moved upward a little for interference fringe observation.

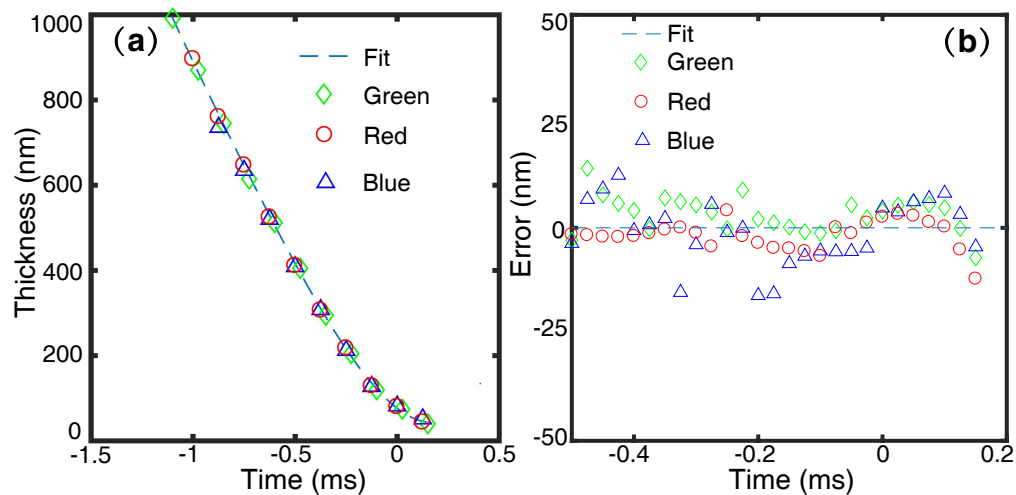


Figure A.3: (a) The film thickness reconstructed from the light intensity obtained in different channels and the fitting by a 4th order polynomial. (b) The deviations of the experimental data from the fit.

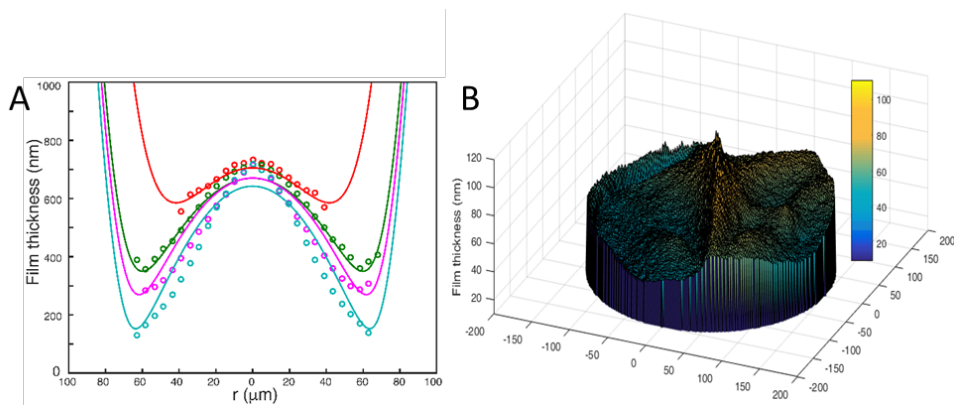


Figure A.4: Thin film profile between a top bubble ($R=1.2$ mm) and a surface bubble ($R=550$ μm) in water (A) Comparison between theoretical predictions and experimental film profiles before the loss of symmetry; (B) 3D thin film profile reconstructed from the last snapshot of Figure 3.3.

Appendix B

Supporting information for chapter 3

B.1 Unusual force curves

In the chapter 3 we reported force measurements that included an increase stage and a stable stage. In Figure B.1, we report two examples with different force features. The blue circles in Figure B.1A show the interaction force between the millimeter size bubble and a surface microbubble with the small radius of $68 \mu\text{m}$ that the film ruptures before the stable stage is reached. To explain the reason, the model was used to predict the film thinning behavior which stopped at the experimental rupture time. By this time, a rim thickness of around 35 nm is predicted. This thickness is in the range $(25 \pm 15 \text{ nm})$ of the critical rupture thickness observed in the experiment (see Figure 3.7). The rapid thinning of the liquid film in this experiment contributes to the quick coalescence of the two bubbles without the observation of the stable interaction force. Although the stable stage was not achieved in the three cases provided in the inset in Figure B.1B, the size dependence behavior of the coalescence time and the interaction force was observed. After the transition bubble radius around $100 \mu\text{m}$, typically the stable stage was observed on the force profile. The red circles in Figure B.1A describe the interaction force between a top millimeter size bubble and a surface microbubble with the radius of $330 \mu\text{m}$. It is noteworthy that the force drops a little before the stable stage. The decrease of the interaction force is a result of the slight movement of the three-phase

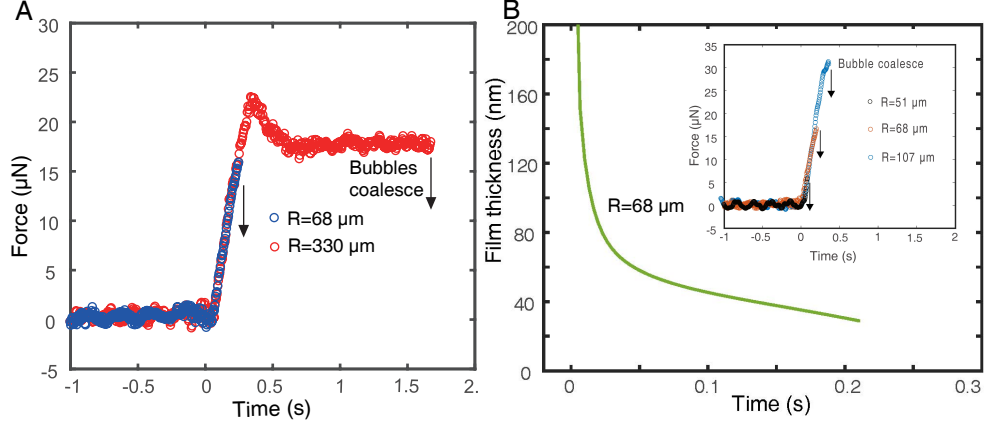


Figure B.1: (A) The interaction force between a top millimeter bubble and surface microbubbles with the radius of $68 \mu\text{m}$ (early coalesce) and $330 \mu\text{m}$ (late coalesce); (B) The predicted film thickness at the rim between the top bubble and the surface microbubble ($R=68 \mu\text{m}$), the model prediction stops at the rupture time obtained from the experiment. The inset shows the size dependence trend of the interaction force and coalescence time.

contact line of the surface microbubble during the experiment.

B.2 The role of EDL interaction

As mentioned in the chapter 3, the colloidal stability between two bubbles is predicted by the DLVO theory and has been observed in experiments with low collision velocities. Although the fitted air-water surface potential varies from -30 mV to -100 mV in those reported conditions, [12, 85, 101] the thin liquid film was suggested to be stabilized by the repulsive EDL force. However, the thin film lost its colloidal stability when the approaching velocity is high. [6] To gain a better understanding, the disjoining pressure between two identical air-water interfaces is calculated using the DLVO theory. The calculation is independent of the SRYL model and both the constant surface charge and the constant surface potential boundary condition are considered in the calculation of the EDL interaction. Detail equations for the calculation are shown below. [122] Two surface potential values were assumed in the calculation: one value (-40 mV) within the reported range, and the other (-20 mV) weaker than the reported surface potentials. Thereby we hope to stress

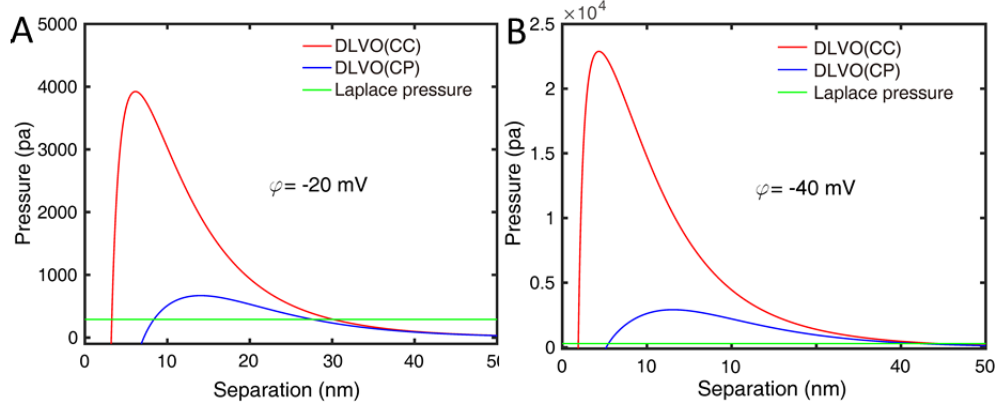


Figure B.2: Pressure profile between two identical air-water interfaces (A) surface potential is -20 mV; (B) surface potential is -40 mV. The disjoining pressure was calculated based on the DLVO theory under constant surface charge (CC, top line) and constant surface potential (CP, bottom line) boundary conditions. The Laplace pressure (straight line) is calculated with the radius of $500 \mu\text{m}$. The solution is assumed to be 1:1 monovalent salt at the concentration of 1 mM/L .

the discrepancy between the predicted colloidal stability and the experimental coalescence results.

The prediction results are shown Figure B.2. In both conditions, the predictions describe an equilibrium film thickness followed by a high pressure barrier regardless of the boundary condition. The predictions are in contradiction to the experimental results where coalescence are consistently observed. Considering that the high pressure barrier should be much higher than the local hydrodynamic pressure, the discrepancy cannot be explained by the small hydrodynamic pressure that arises from the liquid drainage. One possible explanation has been provided by Castillo and Horn [6] that the air-water surface property might be neither constant nor homogeneous, and can change locally by the flow during the interaction. As mentioned by them, a negligible or even attractive EDL interaction which may lead to abnormal drainage and/or rupture behavior might be predicted in certain conditions. However, we are unable to provide the exact reason for the negligible effect of EDL interaction based on the results of this work. The disjoining pressure between the air-water surfaces is calculated using the equations for parallel surfaces. The overall disjoining pressure is the sum of the VDW interaction and EDL

interaction: $\Pi_{DLVO} = \Pi_{VDW} + \Pi_{EDL}$. For the calculation of van der Waals interaction, a consistent equation ($\Pi_{VDW} = -\frac{A}{6\pi D^3}$), where A is the Hamaker constant, D is the separation) is used. For the calculation of the EDL interaction, both the constant surface potential and the constant surface charge boundary conditions are considered.

Constant surface potential boundary condition [123]

$$\Pi_{EDL} = \frac{4ne^2\psi_0^2}{k_B T} \frac{-2 + e^{D/\lambda_D} + e^{-D/\lambda_D}}{(e^{D/\lambda_D} - e^{-D/\lambda_D})^2} \quad (B.1)$$

Constant surface charge boundary condition: [122]

$$\Pi_{EDL} = \frac{2\sigma^2\lambda_D}{\epsilon\epsilon_0} \frac{2 + e^{D/\lambda_D} + e^{-D/\lambda_D}}{(e^{D/\lambda_D} - e^{-D/\lambda_D})^2} \quad (B.2)$$

Where λ_D is the Debye length calculated as $\lambda_D = 0.304/\sqrt{c_0}$ nm, c_0 is the bulk concentration of electrolyte, k_B is the Boltzmann constant, T is the Kelvin temperature, e is charge of electron, ψ_0 is the surface potential, D is the separation between two surfaces, ϵ_0 is the permittivity of vacuum, ϵ is the dielectric constant of the water, σ is the surface charge, the surface charge and surface potential is related through the Grahame equation: $\sigma = \sqrt{8c_0 \epsilon_0 k_B T} \sinh(e\psi_0/2k_B T)$.

Appendix C

Supporting information for chapter 4

C.1 Model description

A model that assumes mobile air-water interfaces [44–46] was used to explain the fast film thinning phenomenon. In this model, the liquid drainage inside the thin liquid film is described by lubrication theory, while the air flow inside the bubble is described by Stokes flow [14, 44–46] (see Figure C.1). The applied collision velocity yields a global Reynolds number ($Re = 2\rho R_b V/\mu$, where ρ is water density, μ is water viscosity) up to 130. However, the applicability of the lubrication model is easily justified from the film Reynolds number ($Re_f = \rho h_F V_f/\mu$, where h_F is the film thickness, V_f is the velocity of the interface in the vertical direction) [37], which is much smaller than unity because of the small characteristic film thickness of around 10^{-6} m. Under these conditions, the thickness of the film $h(r, t)$ can be obtained from

$$\frac{\partial h}{\partial t} = -\frac{1}{r} \frac{\partial}{\partial r} (rUh) + \frac{1}{12\mu r} \frac{\partial}{\partial r} \left(rh^3 \frac{\partial p}{\partial r} \right) \quad (\text{C.1})$$

The first term on the right hand side of Equation C.1 represents the flow induced by the mobile air-water interfaces featured by the interfacial velocity U (see Figure C.1a). The interfacial velocity is determined by the continuity of tangential shear stress across the interface ($\tau_b = \tau_f$) that arises from film liquid flow

$$\tau_f = \mu \frac{\partial u}{\partial z} \Big|_{z=z^+} = -\frac{h}{2} \frac{\partial p}{\partial r} \quad (\text{C.2})$$

and the bubble air flow $\tau_b = \mu_{air} \partial u / \partial z|_{z=z^-}$. The second equality in Equation C.2 is obtained through derivation of the velocity profile of the flow inside the film, which is calculated from lubrication theory. Using the boundary integral method and the fact that information is only needed at the surface, the interfacial velocity is described as [45, 46]:

$$U(r) = -\frac{1}{\mu_{air}} \int_0^\infty \Phi(r, \omega) \tau_f(\omega) d\omega \quad (C.3)$$

$$\Phi(r, \omega) = \frac{k}{2\pi} \sqrt{\frac{\omega}{2r}} \int_0^\pi \frac{\cos\alpha}{\sqrt{1 - k^2 \cos\alpha}} d\alpha$$

$$k^2 = \frac{2r\omega}{r^2 + \omega^2}$$

Because the surface is assumed clean, the surface tension gradient from the uneven distribution of impurities ($\partial\sigma/\partial r$) is ignored. The interfacial velocity U , determined by the viscosity ratio between water and air ($\kappa = \mu/\mu_{air}$, ~ 50) [44], is very large. Therefore, the film drainage velocity with mobile interfaces can be three or four magnitudes faster than that with immobile air-water interfaces ($U = 0$, see Figure C.1b) where the tangential shear stress is balanced by the Marangoni stress ($\partial\sigma/\partial r + \tau_f = 0$).

The deformation of the air-water interfaces is described by the augmented Young-Laplace equation, which assumes an equilibrium surface profile in response to the pressure. Despite the rapid thinning and deformation in milliseconds, this assumption is still satisfied because the capillary wave velocity is in the order of 1 m/s [24] which is much faster than the characteristic collision velocities of the bubbles (50 mm/s). The augmented Young-Laplace equation is written as

$$p + \Pi = \frac{2\sigma}{R} - \frac{\sigma}{2r} \frac{\partial}{\partial r} \left(r \frac{\partial h}{\partial r} \right) \quad (C.4)$$

In Equation C.4, $R = 2R_b R_s / (R_b + R_s)$ is the harmonic mean radius between the bubbles, σ is the water surface tension, and Π is the disjoining pressure that determines whether the film ruptures or remains stable. Π is generally given by a combination of van der Waals and electrical double layer (also

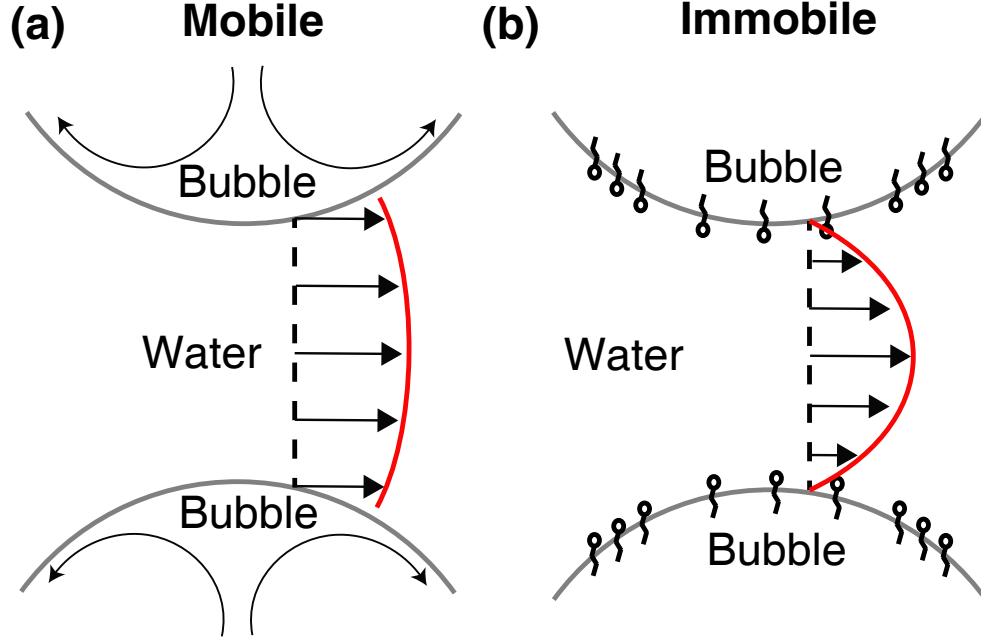


Figure C.1: Schematic illustration for the film flow with immobile and mobile boundary conditions: (a) The interfaces are assumed to be clean so that the Marangoni stress is not considered. The interfacial velocity U is determined by the continuity of tangential shear stress across the interface. For this system the first term on the right hand side of equation C.1 dominates. (b) The tangential shear stress on the interface due to film flow is balanced by the Marangoni stress at the interface ($\partial\sigma/\partial r$) due to the uneven distribution of surface active materials at the interfaces, rendered the surface immobile ($U = 0$). In this case the first term on the right hand side of equation C.1 drops out. Theoretically, these two boundary conditions give rise to drainage rates that are different by orders of magnitude.

known as "DLVO theory"). The van der Waals force between two bubbles is attractive and can possibly rupture the thin liquid film at the thickness below 50 nm [16, 79]. The electrical double layer force was reported to be negligible between two fast colliding bubbles in pure water [6, 19, 79]. In our case, we either do not consider Π or use van der Waals of the form $\Pi = -A/(6\pi h^3)$, where $A \sim 3 * 10^{-20}$ J is the Hamaker constant.

In this work, we focused on the constant approach velocity theory because experimentally we provided data that was generated under precise constant velocity approach. Another possible scenario, the constant force regime (for example, buoyancy force) was not considered experimentally though theory

has also been established [14, 45]. With the fully mobile boundary condition at the interface, the hydrodynamic resistance depends on the viscosity in the bubble/drop phase rather than the draining liquid viscosity [44]. This repulsive force can be large for drops whose viscosity is close or larger than water, in that sense both the constant approach velocity and constant force regimes would provide noticeable differences in drainage behavior. But for air bubbles in our work, the viscosity of air is much smaller than water so that the initial repulsive force is negligible when compared to the buoyancy force, so we did not consider the constant force regime in this work.

As initial condition, we assume the bubbles have a parabolic profile, which is a good approximation for the bubble shape close to the origin. As boundary conditions, we assume symmetry for h and p at $r=0$. At the far-field boundary at $r = r_{max}$, we take $p=0$ and $dh/dt = -V$, the experimental approach velocity.

The governing equations, together with boundary conditions, are solved using the standard linear solver ‘ode15s’ in Matlab. The equations are first nondimensionalized by using the following scales [45] of the variables, after we define the Capillary number as $Ca = \mu_{air}V/\sigma$ (Please note that Ca for mobile interface requires the viscosity of fluid inside the bubble, unlike the immobile case, where the viscosity of the draining liquid is needed). The radial scale is given by $r_c = RCa^{1/3}$, the film thickness scale is given by $h_c = RCa^{2/3}$, the time scale is written as $t_c = RCa^{2/3}/V$ and the pressure scale is simply $p_c = \sigma/R$. Under these natural scales, the first term on the right hand side of Equation C.1 becomes independent of any experimental parameters and the second term only has a negligible contribution to the drainage rate. The numerical solution becomes almost universal for this system, apart from the very last stage just before coalescence. This also means that scaling the experimental data using these scales should provide a universal curve if this model is correct for this system. Such results will be shown in Figure C.3b.

The numerical code in Matlab using the above equations is implemented as follows. With the initial film profile h , we calculate the pressure p from Equation C.4. With h and p we can calculate the shear stress using Equation C.2. With the shear stress we now calculate the surface velocity U using

Equation C.3. With that, we have all the ingredients to solve equation C.1 to get the film profile for the next time step and the process repeats.

C.2 Definition of time ($t=0$) and theoretical results

In this work, we provide a clear definition of the time ($t=0$) since there has not been a standard for defining the initial time for similar systems. From the literature, different definitions have been used. For example:

(1) In Ref. [16], the authors started counting the time at the beginning of the bubble movement and then compared with theory under the same condition. This definition, together with the well-controlled AFM experiment, enabled a fair comparison between the model and the experimental results (which agreed well). One weakness of this definition is that the measured coalescence time depends strongly on the initial separation between the bubbles.

(2) In most literature [17–19], the authors looked at the bubbles from the side and started counting time when the bubbles were close enough. That definition typically gives an error of a few milliseconds in the coalescence time because it depends on the judgment of the person taking the measurements. For the immobile drainage, the correct starting point is not critical as the coalescence time typically exceeds 1 second. However, for the pure water system with the total drainage time in milliseconds, this error cannot be overlooked. By looking from the side, it appears that the coalescence is almost instantaneous in our pure water experiments.

Therefore, we defined the time $t=0$ as the point when the separation becomes zero assuming two non-deformable surfaces approach each other at a given applied approach speed, as shown by the solid red curve in Figs. C.2a,b. Physically, that is the time when the two bubbles would have touched if they did not deform. The ‘coalescence time’ was then defined as the time taken from this point to film rupture. This definition of $t=0$ represents the ideal (fastest) coalescence with no-resistance at the interfaces, while the coalescence time represents the delay between the ideal scenario and the real system.

In Figure C.2a, we compare experimental data with theoretical prediction assuming the attractive van der Waals interaction as the disjoining pressure. The model agreed well with the experimental data until the film thickness reached ~ 200 nm, then the theoretical drainage became faster. In the theoretical plot, the film thickness decreased rapidly starting from ~ 30 nm, agrees with the experimental film rupture thickness. Theoretically this curve corresponds to the center where the film is thinnest. This justifies comparing experimental results and theoretical prediction at the center of the film.

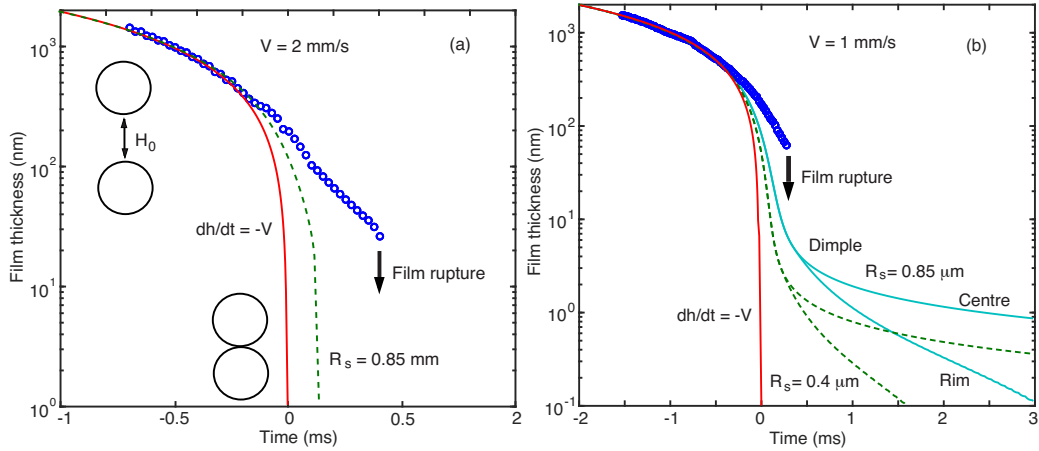


Figure C.2: Comparison between model prediction (lines) and experimental results (blue circles). The definition of time $t = 0$ as the moment that the two undeformed bubbles would have touched each other is represented by the red solid line at constant approach velocity ($V = -dh/dt$). (a) Under the influence of attractive Van der Waals, the theoretical result (green dashed line) predicts film rupture without the formation of a dimple at a time slightly shorter than the experimental film rupture. Inset shows schematic representing the definition of $t = 0$. (b) The effect of bubble size was considered theoretically by performing calculations at the lower end ($R_s = 0.4$ mm, solid cyan line) and higher end ($R_s = 0.85$ mm, dashed green line) of our experimental bubble sizes. In this plot, the influence of Van der Waals was omitted. The formation of a dimple was only predicted at very small thicknesses, after the experimental film rupture had occurred.

To provide further understanding about the features of the model, we also show the effect of bubble radius and neglect the disjoining pressure (II) to observe the formation of the dimple in Figure C.2b. When a dimple forms, the thinnest part of the film is no longer at the center but at some radial

distance called the ‘rim’. The effect of bubble size is negligible until the film thickness reaches ~ 100 nm, although the bubble size is a key parameter influencing film drainage when the air-water surface is immobile (not shown here). Furthermore, the model predicts the dimple (curvature inversion in which the thickness at the center becomes larger than that at the rim) formation at ~ 10 nm, which agrees with the previous theoretical predictions [44, 45]. However, the formation of the dimple is not observed experimentally in this case because the experimental film has ruptured (~ 30 nm) before the formation of the dimple.

Using this definition of $t=0$, all curves from Figure 4.3 can be combined in Figure C.3a. We see a broad range of approach rates where coalescence occurs in just under 1 ms. The starting thickness in each curve depends on the clarity of fringes for a particular experiment. As both surfaces deform, sometimes the interaction region can be slightly out of focus. By using the theoretical thickness and time scales described earlier, all experimental curves fall into a master curve in Figure C.3b. These results further indicate that the experimental data obeys the fully mobile boundary condition. By looking at the log scale inset of Fig C.3b, we observe that for the great majority of curves, the rupture time and rupture thickness are very similar to each other.

The results in Figure C.3b further confirm our results that coalescence is very quick in systems with pure water, almost as fast as two undeformed bubbles approaching at constant speed. As a consequence, if two bubbles impact each other in pure water, coalescence will be almost certain.

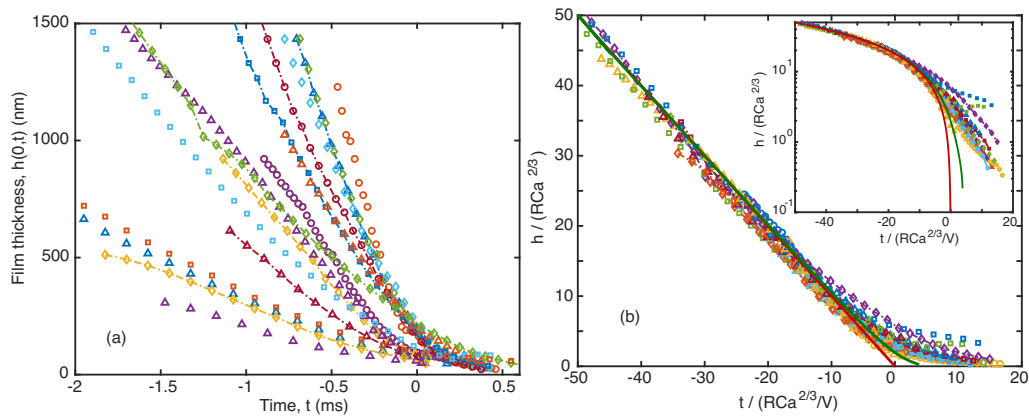


Figure C.3: (a) Experimental data from Figure 4.3a are plotted together following the definition of time $t=0$. (b) Time and thickness are scaled using theoretical time and length scales typical of this system. The red straight line corresponds to the film thinning at the applied speeds. As expected, the data curves overlap, indicating that this model is appropriate for our system. Inset shows the same plot using log scale, where it becomes evident that the rupture thickness and rupture time are similar for all cases. The theoretical prediction shows slightly shorter coalescence time. In this plot we took $R_s = 0.65$ mm, which is a typical value of our experimental data.

Appendix D

Supporting information for chapter 5

D.1 Bubble aging time

The bubbles residing in bulk can be divided into two sub-stages: (1) Bubble growth at the capillary orifice; (2) bubble rise in bulk. The bubble surface area keeps on increasing in the first stage, but barely changes in the second stage. The evolution of the surface area in stage (1) needs to be considered in quantifying the aging time. To be more specific, the measured aging time t_1 for stage (1) needs to be converted to an effective aging time ($t_{eff} = 0.6t_1$). In stage (2) the residence time t_2 is directly used. The overall aging time is given by: $t = t_2 + t_{eff} = t_2 + 0.6t_1$. A detailed derivation for t_{eff} is given here.

At a constant inlet flow rate J , the volume of the growing bubble $V(t) = Jt = \frac{4}{3}\pi(r(t))^3$, where $r(t)$ is the bubble radius at time t . The surface area at time t is,

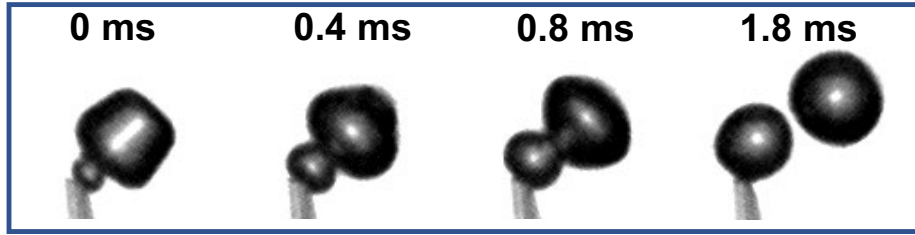
$$A(t) = 4\pi(r(t))^2 = 4\pi \left(\frac{3V(t)}{4\pi} \right)^{\frac{2}{3}} = 4\pi \left(\frac{3J}{4\pi} \right)^{\frac{2}{3}} t^{\frac{2}{3}} \quad (\text{D.1})$$

The effective aging time is defined as follows to represent the equilibrium time for surfactant adsorption at the surface area $A(t_1)$

$$t_{eff} = \frac{\int_0^{t_1} A(t) dt}{A(t_1)} = \frac{\frac{3}{5}A(t_1) \cdot t_1}{A(t_1)} = 0.6t_1 \quad (\text{D.2})$$

Using the above definition, the counted aging time for the pinch-off collisions is between 6.8 ms and 12.7 ms, referred as ~ 10 ms in chapter 5. For the rise

(a) Bounce away



(b) Rapid coalescence

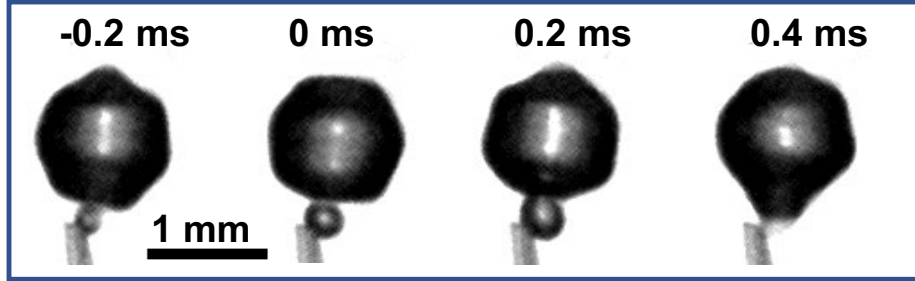


Figure D.1: (a) Snapshots for bubble bounce where a slowly rising bubble was pushed aside by a rapid growing one; (b) Snapshots for the bubble coalescence process. The growing bubble merge into the rising one within 0.4 ms.

collisions, the aging time is between 40 ms and 85 ms, referred as ~ 50 ms in chapter 5.

D.2 Pinch-off collision: bubble bounce and coalescence

The experimental phenomenon in which the bubbles either bounce or coalesce is also observed with the pinch-off collisions. An example for bubble bounce is presented in Figure D.1a, where the slow rising bubble was hit by a bubble that was rapidly growing at the capillary orifice. In this case, the bubble deformation and bounce cannot be clearly observed, because the rising bubble oscillated and deformed even without collision. But there is still a clear sign indicating the interaction force between the bubbles: after colliding for more than 1 ms, the rising bubble was pushed away by the growing one. The acceleration of the rising bubble, mostly in non-vertical direction, clearly demonstrates a repulsive force between the bubbles other than the buoyancy

force, indicating the immobile interface on one or both bubbles.

As a comparison, rapid coalescence is presented in Figure D.1b. Upon collision, the growing bubble at the orifice was "eaten" by the rising one within 0.4 ms. The rising bubble neither accelerated nor changed its trajectory, indicating the negligible repulsive force during their interaction. Therefore, the air-water interface on both bubbles should be mobile.

At the pinch-off case, coalescence between the bubbles happens continually and the rising bubble may engulf numerous growing bubbles before it finally leaves from collision. The probability is counted from the results whether the rising bubble left freely, or was being pushed aside and/or show a quick increase of velocity.

D.3 Force balance

To simulate the rising bubble and its collision with the resting bubble (Figure D.2a) or the flat surface (Figure D.2b), we need to consider the forces exerted on the bubbles. For a free rising bubble at its terminal velocity, the buoyancy force F_B is balanced by the hydrodynamic drag force F_D with the relationship $F_B + F_D = 0$. Upon collision with the resting bubble or the flat air-liquid interface, the pressure builds up in the film giving rise to the film force F_F that decelerates the rising bubble, accompanied by the deceleration of the surrounding liquid contributing to the added mass force F_A . The last two forces should be considered to obtain the force balance ($F_B + F_D + F_F + F_A = 0$). In our system, this balance is written as [15]

$$\underbrace{\frac{4}{3}\pi R_2^3 \rho C_m \frac{dV}{dt}}_{F_A} = \underbrace{\frac{4}{3}\pi R_2^3 \rho g}_{F_B} - \underbrace{C_D \operatorname{Re} \frac{\pi}{4} \mu R_2 V}_{F_D} - \underbrace{\int_0^{r_\infty} 2\pi r p dr}_{F_F} \quad (\text{D.3})$$

In the above equation, $C_m=0.5$ is the added mass coefficient, $\rho=998 \text{ kg/m}^3$ is the water density, $g=9.8 \text{ m/s}^2$ is the acceleration due to gravity. C_D is the drag coefficient which depends on the Reynolds number $Re = 2R\rho V/\mu$. For $C_D Re$, we use equations given by Moore [124] for mobile air-water interface or Schiller & Naumann [125] for immobile air-water interfaces. Detailed derivation and

applications can be found in the review of Manica et al. [15]. The film force F_F is calculated by integration of the pressure p inside the thin liquid film from the center to infinity. The pressure p inside the liquid film is a complex interplay of the Laplace pressure ($2\sigma/R$, σ is air-water interfacial tension, R is the harmonic mean radius $R = 2R_1R_2/(R_1 + R_2)$ for two bubbles collision, and is the rising bubble radius for the bubble-flat surface collision, see Figure D.2b), the surface deformation, and the disjoining pressure (Π). The relationship is known as the Young-Laplace equation, for the collision between a bubble and a flat surface:

$$p = \frac{2\sigma}{R} - \frac{\sigma}{r} \frac{\partial}{\partial r} \left(r \frac{\partial h}{\partial r} \right) - \Pi \quad (\text{D.4})$$

On the right hand side of the Young-Laplace equation, the Laplace pressure is directly calculated with the known bubble radius. The surface deformation depends on the pressure inside the film, including the disjoining pressure given by van der Waals and electrical double layer interactions. Therefore, a detailed treatment of the thin film evolution is achieved with the lubrication approximation. Three boundary conditions at the air-water interfaces should be considered when deriving the lubrication equations for our systems. Detail descriptions of the lubrication equations using three boundary conditions can be found in section 2.2.2, chapter 2.

D.3.1 Initial condition

The above equations are solved numerically using Matlab, with the initial film thickness given by:

$$h(r, 0) = h(0, 0) + \frac{r^2}{2R} \quad (\text{D.5})$$

where $h(0, 0)$ represent the initial separation between the center (apex) of the bubble and the flat surface.

D.3.2 Boundary conditions

The numerical simulation is limited within a region $0 < r < r_m$, with r_m similar to the bubble size. The deformation outside r_m is considered through proper

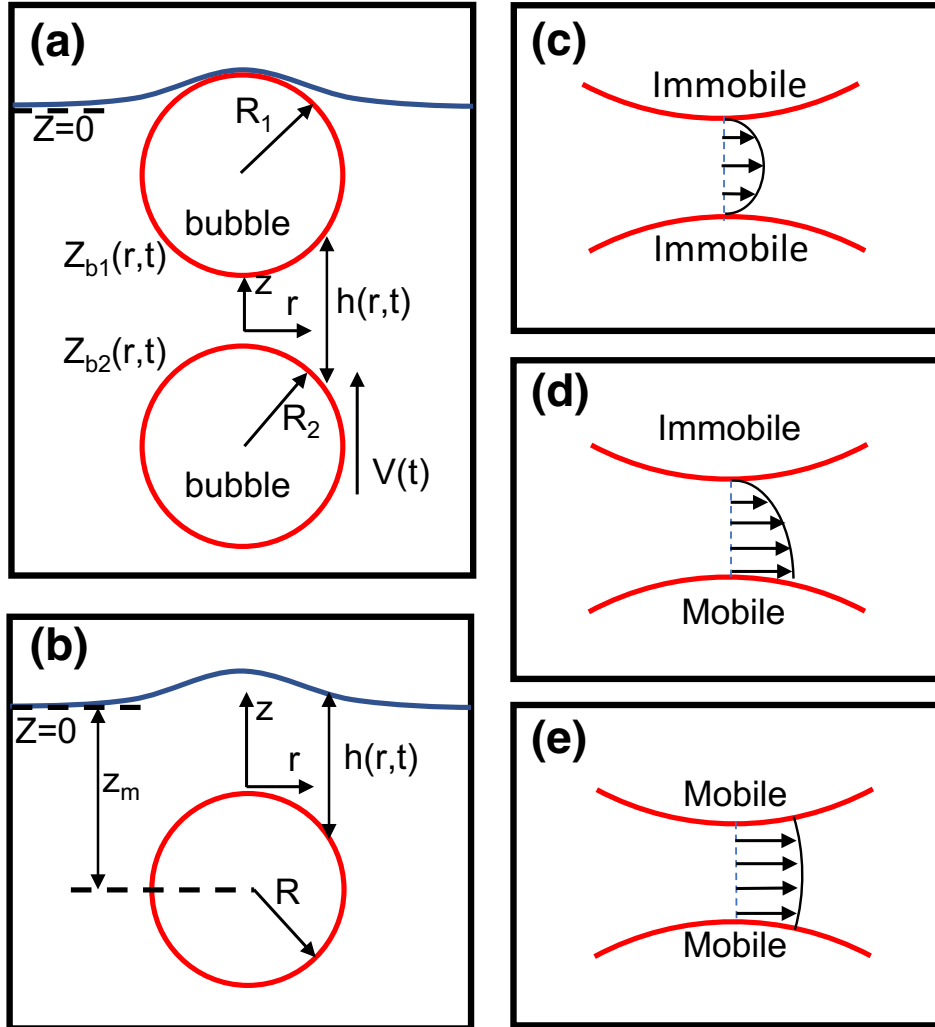


Figure D.2: (a) Schematic of the rising bubble hitting another bubble resting on the flat surface, with the symbols defined; (b) Schematic of the rising bubble hitting the flat surface, with the symbols defined. The other three schematics describe the boundary conditions at the air-water interface: (c) Immobile-immobile; (d) Immobile-mobile; (e) Mobile-mobile.

boundary conditions. This method helps to greatly reduce the numerical cost compared with full solutions, while keeping the accuracy at the nanometer scale. [24]

For the simulations between a rising bubble and the flat surface, both the rising bubble and the flat air-water interface can deform during the interaction. In the simulation, only the deformation of the free surface is taken into account, this simplification provides good results as discussed by Manica et al. [15]. The flat surface deformation in response for the overall interaction force F , is described by an analytical solution $z(r) = \frac{F}{2\pi\sigma} K_0(r/\lambda)$ [15], where $K_0(r/\lambda)$ represents the Bessel function of the second kind at order 0, $\lambda = \sqrt{\frac{\sigma}{\rho g}}$ is the capillary length. Therefore, we can obtain the boundary condition for the flat surface where $F = F_F$:

$$z(r_m, t) = \frac{F_F}{2\pi\sigma} K_0\left(\frac{r_m}{\lambda}\right) \quad (\text{D.6})$$

and boundary condition for the rising bubble.

$$z_b(r_m, t) = H(t) - \frac{r_m^2}{2R} \quad (\text{D.7})$$

with $H(t) = z_m(t) - R$ shown in Figure D.2b. By subtracting these two terms, the boundary condition for the film thickness at r_m is given by:

$$h(r_m) = z(r_m, t) - z_b(r_m, t) = \frac{F_F}{2\pi\sigma} K_0\left(\frac{r_m}{\lambda}\right) - H(t) + \frac{r_m^2}{2R} \quad (\text{D.8})$$

and the film thinning rate at r_m is:

$$\frac{dh}{dt} = V + \frac{1}{2\pi\sigma} K_0\left(\frac{r_m}{\lambda}\right) \frac{dF_F}{dt} \quad (\text{D.9})$$

For the bubble collision with mobile-mobile air-water interfaces, the film force is negligible ($F_F \approx 0$), then the boundary condition can be further simplified to $dh/dt = V$.

Appendix E

Lubrication equations

In chapter 2, the governing equations for the thin film drainage under different boundary conditions were briefly introduced. They are obtained from the lubrication approximation of the Navier-Stokes equations under the assumption that one length scale is much smaller than the others. In this section, the derivation of the thin film equations from the lubrication equations is briefly presented.

For simplicity, we define the experimental system with two identical bubbles approaching each other (see Figure E.1a). Therefore, only the immobile-immobile and mobile-mobile boundary conditions are discussed. The purpose of this simplification is to describe the concept in a easier way. The same equation can be obtained without this simplification. The definition of the coordinate system is shown in Figure E.1b, where $r = 0$ is set at the film radial center, $z = 0$ is defined at the film vertical center.

The lubrication equations E.1, E.2 in cylindrical coordinates and the continuity equation E.3 are written as

$$\frac{\partial p}{\partial z} = 0 \tag{E.1}$$

$$\frac{\partial p}{\partial r} = \mu \frac{\partial^2 u}{\partial z^2} \tag{E.2}$$

$$\frac{1}{r} \frac{\partial (ru)}{\partial r} + \frac{\partial u_z}{\partial z} = 0 \tag{E.3}$$

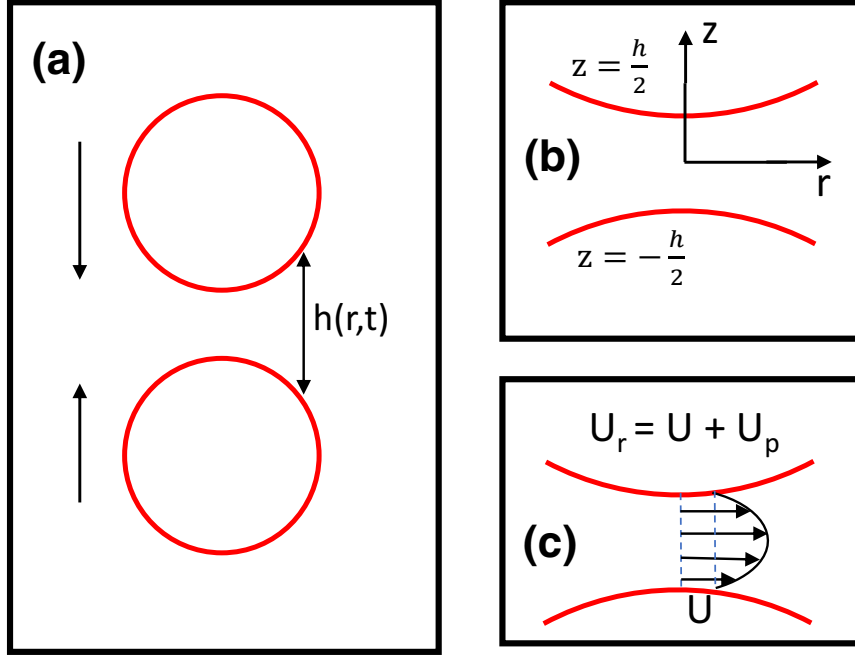


Figure E.1: (a) Schematic illustration for bubble collision; (b) the definition of the coordinate system; (c) schematic illustration of the radial velocity U_r .

For simplicity, the radial velocity is separated into two components $U_r = U + U_p$ (see Figure E.1c), where U describes the surface velocity, U_p describes the parabolic velocity with the highest value at $z = 0$.

To obtain the film drainage equation, first of all, the continuity equation E.3 is integrated in the z direction to obtain:

$$U_z = \int \frac{1}{r} \frac{\partial}{\partial r} (rU_r) dz + C_0 \quad (\text{E.4})$$

Here, we can link the film thinning rate with the approach of two surfaces $\partial h / \partial t = U_z|_{z=h/2} - U_z|_{z=-h/2}$:

$$\frac{\partial h}{\partial t} = \int_0^{\frac{h}{2}} \frac{1}{r} \frac{\partial}{\partial r} (rU_r) dz + \int_{-\frac{h}{2}}^0 \frac{1}{r} \frac{\partial}{\partial r} (rU_r) dz = \int_{-\frac{h}{2}}^{\frac{h}{2}} \frac{1}{r} \frac{\partial}{\partial r} (rU_r) dz \quad (\text{E.5})$$

As we defined, $U_r = U + U_p$, and U is a value independent of z , the relation in equation E.5 can be written as:

$$\frac{\partial h}{\partial t} = \frac{1}{\gamma} \frac{\partial}{\partial r} \left\{ r \int_{-\frac{h}{2}}^{\frac{h}{2}} U_r dz \right\} = \frac{1}{\gamma} \frac{\partial}{\partial r} (rUh) + \frac{1}{\gamma} \frac{\partial}{\partial r} \left\{ r \int_{-\frac{h}{2}}^{\frac{h}{2}} U_p dz \right\} \quad (\text{E.6})$$

From then on, the contributions from the surface velocity U and the parabolic velocity U_p on film thinning can be discussed separately. Firstly, U_p can be obtained from the the momentum equation E.2. Because the surface velocity U independent of z :

$$\frac{\partial^2 U}{\partial z^2} = \frac{\partial U}{\partial z} = 0 \quad (\text{E.7})$$

Therefore, equation E.2 can be written into:

$$-\frac{\partial p}{\partial r} = \mu \frac{\partial^2 U_r}{\partial z^2} = \mu \frac{\partial^2 U_p}{\partial z^2} \quad (\text{E.8})$$

By integrating equation E.8 in the z direction, and considering equation E.1 that the pressure only varies in the r direction, we get:

$$\frac{\partial U_p}{\partial z} = \frac{-1}{\mu} \frac{\partial p}{\partial r} \cdot z + c_1 \quad (\text{E.9})$$

In the above equation, $c_1=0$ because $\frac{\partial U_p}{\partial z} = 0$ at $z = 0$. A further integration results in:

$$U_p = \frac{-1}{2\mu} \frac{\partial P}{\partial r} z^2 + c_2 \quad (\text{E.10})$$

By applying the boundary conditions $U_p = 0$ at $z = \pm h/2$, we can obtain:

$$U_p = \frac{-1}{2\mu} \frac{\partial P}{\partial r} \left(z^2 - \frac{h^2}{4} \right) \quad (\text{E.11})$$

With equation E.11, equation E.5 is converted into:

$$\frac{\partial h}{\partial t} = -\frac{1}{r} \frac{\partial}{\partial r} (rUh) + \frac{1}{12\mu r} \frac{\partial}{\partial r} \left(rh^3 \frac{\partial p}{\partial r} \right) \quad (\text{E.12})$$

The above equation is the same as equation 2.6 for mobile-mobile lubrication. In this scenario, a further step is required to obtain the surface velocity U by considering the continuity of stress at the interfaces (see equation 2.7). If $U = 0$, equation E.12 is simplified into equation 2.4 for the immobile-immobile boundary condition.